Title
Functional Analysis of Iron Storage and Transport in the Green Alga Chlamydomonas reinhardtii

Author
Hui, Colleen

Publication Date
2021

Peer reviewed|Thesis/dissertation

UNIVERSITY OF CALIFORNIA

Los Angeles

Functional Analysis of Iron Storage and Transport in the Green Alga *Chlamydomonas reinhardtii*

A dissertation submitted in satisfaction of the
requirements for the degree Doctor of Philosophy
in Biochemistry, Molecular and Structural Biology

by

Colleen Hui

2021

ABSTRACT OF THE DISSERTATION

Functional Analysis of Iron Storage and Transport

in the Green Alga *Chlamydomonas reinhardtii*

by

Colleen Hui

Doctor of Philosophy in Biochemistry, Molecular and Structural Biology

University of California, Los Angeles, 2021

Professor Joseph Loo, Co-Chair

Professor Sabeeha Merchant, Co-Chair

Iron (Fe) is vital to growth and energy production of living organisms because it serves as a critical cofactor in many enzymatic reactions. Understanding Fe homeostasis in the plant lineage, including Fe storage and recycling mechanisms, provides a pathway to improve global primary productivity in agriculture and carbon capture capabilities. *Chlamydomonas reinhardtii* is a eukaryotic, unicellular green alga that has been used as a photosynthetic reference organism for the study of Fe metabolism, biofuel production, and other processes. In many organisms, Fe storage is often realized using vacuoles or the prototypical Fe storage protein, ferritin. In Chlamydomonas, ferritin appears to play a minor role in Fe storage, as its abundance is reduced with increasing amounts of extracellular Fe. Separately, the acidocalcisome, a lysosome-related vacuole characterized by acidic pH, high calcium (Ca) and polyphosphate (polyP) content, has been shown to house various trace metal ions in over-accumulating situations and is a candidate reservoir for Fe storage. Yet, the exact location for excess Fe in Chlamydomonas is uncertain. The pathway for and the regulation of sequestration, distribution, and mobilization of excess Fe

taken up under Fe luxury conditions are not well understood either. Targeting these issues, my project was set to address three specific aims on Fe storage and transport in Chlamydomonas: 1) Systematic analysis of secondary experimental variables that determine cellular Fe accumulation; 2) Distinguishing the role of acidocalcisomes in Fe storage; and 3) Identifying the molecular mechanisms for excess Fe sequestration and mobilization. In Aim 1, six common experimental variables relating to various environmental aspects were surveyed to examine their impact on cellular growth and Fe content. The results revealed that cells over-accumulate Fe during stationary phase (3-fold increase) and in alkaline condition (10-fold increase). These Fe over-accumulating conditions were used to address questions in Aim 2 and 3. In Aim 2, various types of elemental images consistently showed Fe in cells grown at alkaline pH colocalizing strongly with Ca and P, markers of acidocalcisomes. In contrast, the Fe accumulated in cells during stationary phase is mostly sequestered into foci that do not contain Ca or P, suggesting an Fe storage site other than the acidocalcisome. Thus, cells may be selectively housing Fe in the acidocalcisome under specific conditions. Interestingly, investigation over the bioavailability of stored Fe suggested that the Fe accumulated under alkaline condition is not readily accessible, as indicated by the slow growth of cells from such cultures upon transfer to Fe-free medium. In Aim 3, a comparative transcriptomic analysis of cells grown in alkaline vs. neutral media exposed a significant increase (138-fold) in the abundance of *FEA2* transcripts, encoding a periplasmic Fe-assimilating protein, hence strongly implicating FEA2 in playing a specific role in Fe accumulation under alkaline condition. In addition, a set of ten mutants involved in Fe homeostasis was tested for the capability to accumulate and re-distribute excess Fe. Surprisingly, the *fer1* strain, lacking the predominant ferritin subunit, over-accumulated even more Fe than did the wild-type and other tested mutant strains, but failed to benefit from its greater Fe content. This outcome implies that ferritin has a role in Fe acquisition and mobilization. Altogether, my studies provide a methodical analysis of the experimental stimuli resulting in Fe accumulation and the underlying mechanisms of Fe storage and transport in Chlamydomonas at a fundamental level.

The dissertation of Colleen Hui is approved.

Catherine Clarke

Megan McEvoy

Sabeeha Merchant, Committee Co-Chair

Joseph Loo, Committee Co-Chair

University of California, Los Angeles

2021

TABLE OF CONTENTS

LIST OF FIGURES, TABLES, AND ABBREVIATIONS

Figures

Tables

Supplementary Figures

Supplementary Table

Abbreviations

ICP-MS/MS	inductively coupled plasma tandem mass spectrometry analysis
NanoSIMS	nanoscale secondary ion mass spectroscopy
PFD	photon flux density
polyP	polyphosphate and pyrophosphate
ROI	region of interest
ROS	reactive oxidative species
TAP	Tris acetate-phosphate (growth medium)
TEM, SEM	transmission or scanning electron microscopy
TOC	total organic carbon analysis
XFM	X-ray fluorescence microscopy

Examples of Nomenclature

Nucleus-encoded gene:	*FER1*
Mutated nucleus-encoded gene:	*fer1*
Nucleus-encoded protein:	FER1 or ferritin1

ACKNOWLEDGMENTS

I want to express my deepest thanks to my advisor, Professor Sabeeha Merchant, for her instrumental guidance and support throughout my doctoral studies. I am especially appreciative of the intellectual challenges and the demand of high standard that she puts forth, for I have grown both professionally and personally as a result. I am also grateful to my thesis committee, Professor Joseph Loo, Professor Catherine Clarke, and Professor Megan McEvoy, for their advice and continuous support, particularly during stressful times. I am very much thankful to Dr. Peter Weber as well for his training and supervision over all NanoSIMS work, and for his constant help throughout my time at Lawrence Livermore National Laboratory (LLNL).

I would like to extend my thanks to the rest of the Merchant group, including both members from UCLA and from UC Berkeley. Their aid and support in times of need are a significant contribution toward the completion of my project. Furthermore, their valuable inputs on science and research have taught me important lessons that made me a more skillful researcher, and conversations with them have brought me much joy over the years. I want to thank Dr. Stefan Schmollinger and Dr. Daniela Strenkert in particular, who have been always so kind and encouraging, and were always available to assist me in whatever I needed in and outside of the laboratory. I am grateful for the combination of mentorship and friendship they have afforded me. I am also thankful to Dr. Sean Gallaher for generating the library for my transcriptomic experiment and assisting me in the subsequent data analysis, and I appreciate Dr. Patrice Salome for his effort in genotyping the mutant strains that I used in my studies.

Aside, I want to thank Christina Ramon and Christine Zachow for their assistance over research as well as administrative concerns at LLNL. To all the staff at the Electron Microscopy Lab at UC Berkeley, thank you for your training and guidance on all EM-related work. I want to thank Dr. Si Chen at Argonne National Laboratory as well for her help in setting up and analyzing data from the X-ray fluorescence microscopy experiments. I thank Professor Hosea Nelson and

his group at UCLA for synthesizing the IP1 dye for our experimental use, and I am grateful to Dr. Mark Arbing at the Protein Expression Lab at the UCLA-DOE Institute, along with Dr. Lital Davidi, Dr. Kristen Holbrook, and Dr. Daniela Strenkert from the Merchant group, for designing and testing the αV-PPase antibody. I am also appreciative of Dr. Crysten Blaby-Haas for permitting me to modify and use her figure (Figure 1.2) for this dissertation.

Finally, I would like to thank my family and friends for their unwavering love, patience, and support, regardless of how difficult times might be. I want to thank my late father, my mother, brother, and husband especially: Thank you for inspiring me to become the person I am today and continuously motivating me to be better. I cannot express in words how grateful I am to have everything that you have given me. I have been truly fortunate to have such an incredible support system.

All work was supported by the fellowship award offered to Colleen Hui by the Graduate Research Scholar Program at LLNL, as well as by a grant to Professor Sabeeha Merchant from the US Department of Energy, Office of Science, Basic Energy Sciences under Award # DE-SC0020627.

BIOGRAPHICAL SKETCH

Education:

2014 - 2016	M.S. Biochemistry & Molecular Biology, Oregon Health & Science University, Portland, OR
2009 - 2013	B.S. Chemical Biology, UC Berkeley, Berkeley, CA
2009 - 2013	B.A. Latin, UC Berkeley, Berkeley, CA

Employment History:

12/2018 - 06/2021	Visiting graduate student, Department of Molecular and Cellular Biology, Department of Plant and Microbial Biology, UC Berkeley, Berkeley, CA (Supervisor: Dr. Sabeeha Merchant)
10/2018 – 06/2021	Livermore Graduate Research Scholar, Lawrence Livermore National Laboratory, Livermore, CA (Supervisor: Dr. Peter Weber)
09/2016 – 06/2021	Graduate student researcher, Department of Chemistry and Biochemistry, UCLA, Los Angeles, CA (Supervisor: Dr. Sabeeha Merchant)
09/2014 - 06/2016	Graduate student researcher, Institute of Environmental Health, Oregon Health & Science University, Portland, OR (Supervisor: Dr. Pierre Moënne-Loccoz)
07/2013 - 06/2014	Research assistant, University of Oregon, Eugene, OR (Supervisor: Prof. Andy J. Berglund)
06/2011 - 05/2013	Research assistant, Produce Safety & Microbiology, U.S. Department of Agriculture, Agricultural Research Service, Pacific West Area, Western Regional Research Center, Albany, CA (Supervisor: Dr. Christopher Silva)
07/2010 - 06/2011	Research assistant, Plant Mycotoxin Research, U.S. Department of Agriculture, Agricultural Research Service, Pacific West Area, Western Regional Research Center, Albany, CA (Supervisor: Dr. Sui Sheng Hua)
05/2010 - 08/2010	Student intern, Research and Development Department, Libby's Laboratories Inc., Berkeley, CA (Supervisor: Dr. Stacey Cruz)

Award:

10/2018 - 09/2021	Selected recipient of the Livermore Graduate Scholar Fellowship, awarded by Lawrence Livermore National Laboratory, Livermore, CA
05/2021	Daniel E. Atkinson and Charles A. West Dissertation Award

Publications:

A) Published papers and submitted manuscripts

1. **Hui C**., Schmollinger, S., Glaesener, A. (2021) Growth Techniques. The Chlamydomonas Sourcebook, 3rd edition. Ed. U Goodenough, submitted.
2. Schmollinger S, Chen S, Strenkert D, **Hui C**, Ralle M, Merchant SS (2021) Single-cell visualization and quantification of trace metals in Chlamydomonas lysosome-related organelles. *Proc Natl Acad Sci USA*, 118(16) e2026811118.

3. Deredge DJ, Huang W, **Hui C**, Matsumura H, Yue Z, Moënne-Loccoz P, Shen J, Wintrode PL, Wilks A (2017) Ligand-induced allostery in the interaction of the *Pseudomonas aeruginosa* heme binding protein with heme oxygenase. *Proc Natl Acad Sci USA* 114(13):3421-3426.
4. Silva CJ, Erickson-Beltran ML, **Hui C**, Badiola JJ, Nicholson EM, Requena JR, Bolea R (2016) Quantitating PrP polymorphisms present in prions from heterozygous scrapie-infected sheep. *Anal Chem.* 86(1):854–861.
5. Silva CJ, Erickson-Beltran ML, Skinner CB, Dynin I, **Hui C**, Patfield SA, Carter JM, He X (2014) Safe and effective means of detecting and quantitating shiga-like toxins in attomole amounts. *Anal Chem.* 86:4698-4706.
6. Silva CJ, Dynin I, Erickson ML, **Hui C**, Carter JM (2013) PS.02. Oxidation of methionine in PrP is dependent upon the oxidant and the amino acid two positions removed. *Prion 7(Supplement):* 81.
7. Silva CJ, Dynin IA, Erickson ML, Requena JR, Balachandran A, **Hui C**, Onisko BC, Carter JM (2013) Oxidation of methionine 216 in sheep and elk PrP is highly dependent upon the amino acid at position 218, but is not important for prion propagation. *Biochemistry* 52(12):2139-2147.

B) Manuscripts in preparation

1. **Hui C**, Schmollinger S, Gallaher S, Weber KP, Merchant SS. Changes to the elemental composition of the green alga *Chlamydomonas reinhardtii* based on variations in cultivation conditions.
2. **Hui C**, Salome P, Schmollinger SS, Merchant SS. Distinct phenotypic classes of iron homeostasis pathway mutants.
3. Castruita M, Martin RH, Gallaher S, Lewis BE, Holbrook KN, Hofmann C, Schmollinger S, Krejci M, **Hui C**, Stemmler T, Clemens S, and Merchant SS. Cd toxicity impacts the transcriptome and global mineral homeostasis in Chlamydomonas.

CHAPTER 1

Introduction

1.1 Iron homeostasis is essential to life.

Iron (Fe) is a bio-essential trace metal for life because it facilitates a wide range of reactions, most importantly as a cofactor in electron transport and redox chemistry. Fe proteins are involved in DNA synthesis and repair, oxidative stress mitigation, fatty acid metabolism, and respiration, just to name a few processes. In photosynthetic organisms, the demand for Fe is especially high, since Fe is additionally used as a cofactor in all the abundant complexes of the photosynthetic electron transport chain (Photosystems I and II, cytochrome b_6f) and in ferredoxins (1). Despite its abundance in the earth's crust, Fe bioavailability in nature is low due to its insolubility in the Fe^{3+} oxidation state, which is the prevalent species in oxygenated environments (2, 3). As a result, organisms, especially microbes, have developed a collection of sophisticated Fe acquisition strategies to satisfy their Fe demands, even when the surrounding abundance is low. Meanwhile, excess and unbound Fe within the cell can lead to the generation of deleterious reactive oxygen species (ROS) through the Fenton reaction (4, 5). To prevent harm, cells must detoxify such Fe, either by binding them to proteins or metabolites, or by sequestering them in a less reactive state. It is vital for cells to achieve a balance between the essential need and potentially toxic surplus of Fe. Maintaining such a (near-)steady state intracellular Fe quota typically involve selective uptake, intracellular distribution of Fe, and expression of Fe proteins in response to changing Fe concentrations in the environments (6). This controlled Fe economy is a major attribute that confers to organisms the flexibility to tolerate nutrient fluctuations, quickly acclimate to cellular demands, and thrive within various niches.

1.2 Chlamydomonas is a powerful reference organism for the study of eukaryotic metal metabolism and biofuel production.

For over three decades, the eukaryotic, single-cell, green alga *Chlamydomonas reinhardtii* has been used as a reference organism for investigating trace metal metabolism in photosynthetic organisms (7–9). It is also a dominant model organism for research on algae as a source of biofuels and bioproducts (10, 11). There are several advantages in using Chlamydomonas in research: 1) Chlamydomonas, as part of the Viridiplantae, shares common ancestry and many biological features with land plants, including the photosynthetic apparatus (12). Discoveries made in Chlamydomonas and in land plants, such as those relating to Fe homeostasis, are often translatable to one another. Yet, Chlamydomonas is much simpler to work with than are land plants. It is haploid, unicellular, and has smaller gene families and a less complex gene structure compared to many land plants (12). 2) Furthermore, Chlamydomonas retains certain genes and features that were present in the common ancestor to both plants and animals, thus making it a useful reference organism outside of the plant kingdom as well (*e.g.* assembly and motility of eukaryotic cilia/flagella) (12, 13). 3) Chlamydomonas has an established genetic system with a well annotated, high quality genome assembly (14–16), which allows for molecular and genetic manipulation. A high-coverage library of loss of function insertional mutants for convenient functional studies has also been generated as a result (17, 18). 4) As it is unicellular, Chlamydomonas is grown like a microbe in a chemically-defined medium in the laboratory, with doubling times as fast as 6 hours. This advantage gives experimenters access to a homogenous population that can be exposed simultaneously to various perturbations, which is especially useful for nutritional studies. Radioactive or stable isotopes can be used for an excellent signal to noise ratio in metabolic tracer experiments. 5) Chlamydomonas is a facultative photoheterotroph that can produce ATP from either photosynthesis or respiration (19, 20). This feature enables researchers to design straightforward experiments to explore the effect of Fe nutrition on bioenergetic metabolism, simply by providing light and/or a reduced carbon source. Altogether,

Chlamydomonas provides an excellent experimental system, especially for tracking and monitoring movement and mobilization of Fe and other trace metals at a subcellular level.

1.3 What is known (and unknown) about Fe homeostasis in Chlamydomonas?

1.3.1 Fe nutrition

Four Fe nutrition stages, namely Fe-limited, Fe-deficient, Fe-replete, and Fe-excess, can be distinguished in Chlamydomonas under photoheterotrophic condition, *i.e.* when both light and acetate are provided (Figure 1.1) (21–23). These stages were defined based on phenotypes, the intracellular abundance of Fe, and the expression of genes coding for key sentinel proteins. Examples of proteins whose abundance is Fe-responsive include those involved in high-affinity Fe acquisition, which are stimulated in production when Fe becomes limited, and those that are Fe-containing and abundant, which are reduced in abundance under Fe limitation. Cultures can be induced into each stage by controlling the amount of Fe provided in the growth medium at the time of cell inoculation, typically at a density of 10^4 cells/ml. To induce Fe limitation, $\leq$ 0.5 μM of Fe^{3+}-EDTA is added to the growth medium at the time of inoculation; for Fe deficiency, 1-3 μM of Fe is added; Fe replete, 20 μM; and for Fe excess, from 50 up to 200 μM of Fe. It is important to note that the Fe status in a cell is governed by the Fe content per cell, as opposed to the external Fe concentration per se. The above medium Fe concentrations were determined specifically for cultivating cultures in a laboratory, in which a moderate to high cell density can be readily attained. In an environment where the cell density is low, even sub-micromolar levels of Fe may be sufficient to achieve an Fe-replete situation. However, because each cell has a minimal Fe quota for growth, low density, replete cultures transition to Fe deficiency or limitation as the cells consume Fe for continued growth and division.

Under Fe limitation, cells are growth-inhibited and chlorotic. These cells contain at least 4-fold less Fe than Fe-replete cells accumulate throughout their growth cycle. The transcription of genes for Fe uptake is maximally activated, as cells seek to assimilate even the smallest

amount of available Fe in their vicinity. Generally, the minimal Fe quota in cells is determined by the minimal abundance of essential Fe proteins under Fe limiting conditions. When Chlamydomonas cells face Fe limitation, they operate in an “Fe economy mode”, in which non-essential Fe proteins are degraded or replaced by Fe-independent but functionally-equivalent proteins (21). In turn, the released Fe atoms are reserved for essential Fe-containing proteins, expressed at the least required abundance (1, 7, 21).

In Fe-deficient cells, growth is not impacted nor is chlorosis visible. Their Fe quota is not fully minimized, thus allowing them to maintain a growth rate similar to that observed with Fe-replete cells. Nevertheless, fluorescence rise and decay kinetics (Kautsky curves) show a slower re-oxidation of the plastoquinone pool in these cells relative to cells replete in Fe (21). Also, under Fe deficiency, cells would already induce the high-affinity Fe assimilation systems to maximize uptake capacity, and in parallel reduce expression of some highly abundant but lower priority Fe-containing proteins (24).

Under the Fe-replete condition, the medium Fe concentration is adjusted to supply enough Fe for cells to satisfy all cellular demands of Fe. Fe-replete cells do not over-express the high-affinity Fe uptake systems, nor are they restricted in their expression of non-essential Fe-containing proteins. They are optimized to grow at the fastest rates. This is the standard growth condition used in many experiments for which the defined growth medium, TAP (Tris-acetate-phosphate) with the revised micronutrient composition (25), was optimized.

Lastly, in the Fe excess stage, cells over-accumulate Fe that is not required for immediate use (23, 26). Fe-excess cells appear without any growth phenotype in comparison to Fe-replete cells, except that they are more sensitive to very high light intensity, which is assumed to exacerbate the Fe-dependent generation of ROS (23). The otherwise asymptomatic growth of Fe-excess cells indicates that while the cells can synthesize all Fe-containing enzymes to saturation as desired, they are also able to safely store away any excess Fe, thus preventing the typical Fe-induced damage that could occur in the absence of other stress stimulants (*e.g.* high

light). It is hypothesized that the stored Fe may be mobilized subsequently for the cell to use when Fe deficiency or limitation is encountered. However, neither the exact storage site for excess intracellular Fe nor the proteins responsible for transporting the stored Fe has been determined in Chlamydomonas.

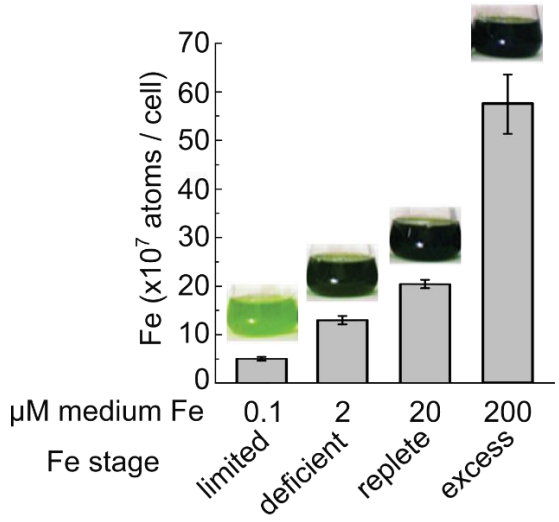

Figure 1.1. The four stages of Fe nutrition in Chlamydomonas. Wild-type Chlamydomonas (CC-4532) cells were grown under constant light (~95 μmol photons·m^{-2}·s^{-1}; see Section 2.2.2 for light quality) at 24ºC in TAP medium containing 0.1, 2, 20, and 200 μM Fe-EDTA chelate, representative of the four Fe nutrition stages as indicated. Cells were collected at late stationary phase and their Fe contents were measured by ICP-MS/MS. Error bars indicate standard deviation of 3 independent cultures. Pictures of a replicate of the cultures under each Fe condition are shown in correspondence. The samples were prepared, imaged, and analyzed by S. Schmollinger (unpublished).

1.3.2 Fe storage

In most eukaryotic cells, ferritin is the prototypical Fe storage unit. Ferritin is a hollow protein complex consisting of 24 polypeptides, which assemble in a spherical shell around a central core that can hold up to 4500 Fe^{3+} ions in mineralized form (27–29). Ferritin possesses ferroxidase activities, which catalyze the oxidation of Fe^{2+} to Fe^{3+} prior to storage in its core, consuming oxygen and hydrogen peroxide in the process (30). Accordingly, beside Fe storage, ferritin can also play a role in protection against oxidative stress through detoxification of excess Fe and dioxygen (31–33). In experiments, Fe-depleted ferritin (apoferritin) may be distinguished

from Fe-containing ferritin (holoferritin) as the former is less thermodynamically stable and much more susceptible to proteolysis (34, 35). The structure of ferritin is generally conserved across species. However, in mammals, ferritin contains two types of subunits, referred to as heavy- and light-chains, whereas all the subunits in the plant ferritin are identical (28).

In Chlamydomonas, as in other plants, ferritin is located in the plastid (27). Two ferritin genes are found in Chlamydomonas, *FER1* and *FER2*. The encoded proteins, FER1 and FER2, are present in the ratio of 70:1 in Fe-replete, photoheterotrophic conditions (36). FER1, the predominant ferritin, is soluble and an important component of Fe homeostasis, whereas FER2 is membrane-associated and is hypothesized to function as an Fe provider for membrane protein biogenesis (36). Interestingly, unlike in land plants and animals in which ferritin abundance is induced as cellular Fe content elevates, Chlamydomonas FER1 is most highly expressed in Fe limitation, especially under photoheterotrophic condition (23, 36–39). This unconventional expression pattern suggests that FER1 in Chlamydomonas might have a different function. For instance, it may function as an Fe buffer, sequestering Fe released from degradation of various Fe-containing proteins. In this role, ferritin would serve as a dynamic reservoir rather than a long-term Fe storage molecule (23, 39). A similar role for ferritin has been proposed in the marine green alga *Ostreococcus tauri*, in which ferritin is used during recycling and redistribution of intracellular Fe in Fe-limiting conditions (40, 41). In addition, FER1 could be involved in ROS mitigation in the plastid as well (29, 31, 33).

Vacuoles are another important storage site in eukaryotes for Fe and other trace metals. These membrane-bound organelles support many essential processes, including protein and macromolecule degradation, storage, buffering, and detoxification, and they are typically constitutively present in the cell (42–44). In yeast and plants, they can also sequester metals, and in some cases, reserve the metals for future use (43, 45, 46). In yeast, the lumen of the vacuole is acidified by the vacuolar H^+-ATPase (V-ATPase), which establishes the proton gradient that drives ion and metal transport into and out of the vacuoles (43) (more on Fe transporters in

Section 1.3.3). Defective vacuole acidification has been shown to compromise the activity of some ion and metal transporters, resulting in increased sensitivity to extracellular pH, ion concentration, as well as heavy metals and oxidants (47–49). Additionally, the yeast vacuole is a major store for calcium (Ca) and polyphosphate (polyP), which may assist metal accumulation (50). The multi-subunit vacuolar transporter chaperone (VTC) complex is required for polyP synthesis and accumulation in the vacuole (51–54). In particular, the loss of function of the VTC1 subunit renders the entire complex ineffective in *Saccharomyces cerevisiae* (52).

In plants, two types of vacuoles, the protein storage and the lytic vacuoles, are known to sequester metals. The protein storage vacuole is located mainly in developing seeds and contains membrane-bound compartments called globoids (44, 55). Globoids are rich in phytic acid, which can chelate metals, including Fe (56, 57). The lytic vacuole is found in vegetative tissues. Similar to the yeast vacuole, the lumen of the lytic vacuole is acidified by both V-ATPases and vacuolar pyrophosphatases (V-PPase), and it contains a variety of molecules for metal binding and transport (45, 58). These vacuoles are crucial for pH homeostasis, buffering and storage of ions and metals (59).

In recent years, the acidocalcisome, a lysosome-related vacuole, has been recognized as a site for metal sequestration in Chlorophyte algae, including Chlamydomonas (46). Originally discovered in trypanosomatids, the acidocalcisome is a cytosolic organelle defined by its acidic lumen, high concentration of Ca, pyrophosphate, and polyP, and can also house trace metal ions (42, 60–63). The acidocalcisome is ubiquitous in eukaryotic cells; similar Ca/polyP-containing compartments with low internal pH have been found in yeast and land plants, as mentioned above, as well as in animals (*e.g.* platelet dense granules in human), protists, and other green and red algae (41, 42, 64–66). Analogous to the yeast and plant vacuoles, the acidocalcisome contains V-ATPases and V-PPase, which acidify the compartment (67, 68). A VTC complex is also found in the acidocalcisome and is essential for polyP synthesis and accumulation within the organelle, just as in the yeast vacuole (54, 69). In Chlamydomonas, studies have demonstrated that the

acidocalcisome can house high amounts of Fe, copper (Cu), and manganese (Mn) under excess conditions (61–63). Furthermore, the accumulated metals are bioavailable in subsequent periods of starvation, suggesting that metal sequestration in the acidocalcisome is dynamic and the organelle may function as a reservoir (61, 62).

1.3.3 Fe transport

Chlamydomonas has been well studied at the cellular level and a well-characterized “map” of known and candidate Fe homeostasis pathways is available (Figure 1.2) There are multiple components of Fe uptake in Chlamydomonas. One is the multicopper ferroxidase, FOX1, which localizes to the plasma membrane and catalyzes the oxidation of Fe^{2+} to Fe^{3+} (22, 70). It is associated with FTR1, an Fe permease, which transports the Fe^{3+} from FOX1 into the cytosol (71). FOX1 is a robust marker for identifying the Fe status in the cell because its expression is highly regulated by Fe nutrition. Under Fe deficiency, the *FOX1* mRNA transcript and the encoded protein increase several folds in abundance (22, 24, 70). Correspondingly, cells with suppressed *FOX1* expression are growth-inhibited in Fe-deficient medium (72). A similar system (Fet3p/Ftr1p) has been previously recognized in yeast and other fungi (73–76), and in the fungal pathogen *Candida albicans* (77–79). As such, the above pathway is identified as a fungal-like ferroxidase dependent ferric transporter complex. At least one FOX1 homolog has also been found in the green algae *Chlorella variabilis*, *Coccomyxa* sp. C-169, and *Volvox carteri*, and it is hypothesized that algae with FTR-like permeases should also have partner multicopper oxidases (80).

Another component of the high-affinity Fe uptake system is FRE1, a ferric reductase also localized to the plasma membrane, which reduces Fe^{3+} to Fe^{2+} (81). The Fe^{2+} can be subsequently directed into the cytosol, likely by an IRT transporter (IRT1 or IRT2) (82). FRE1 is an example of NADPH oxidase, first described with a Fe^{3+} reduction activity in yeast (83, 84). Similar Fe-responsive reductase genes have been found in the model plant *Arabidopsis thaliana* (80, 85) and diatoms (80, 86, 87). In Chlamydomonas, the expression of the *FRE1* transcript is highly

induced under Fe deficiency (82). The IRT proteins are Fe-regulated transporters that belong to a family of divalent metal transporters known as ZIP, found across fungi, plants, and animals (88). In Arabidopsis, the homologous IRT1 is the major Fe uptake protein in the roots, while the expression of *IRT2* transcript is induced under Fe deficiency (89, 90). In contrast, *FRE1*, *IRT1*, and *IRT2* in Chlamydomonas are all negligibly expressed under replete Fe conditions (24). Like *FRE1*, the expression of *IRT1* and *IRT2* in Chlamydomonas is also affected by the Fe status of the cell (82). Both *IRT1* and *IRT2* increase in abundance when the cell faces Fe starvation, but their expression patterns differ; the surge of *IRT2* is more prominent than that of *IRT1* under Fe deficiency, while under Fe limitation, the expression of *IRT1* is over 100 times higher than that of *IRT2* (24). The IRT1 and IRT2 proteins have yet to be characterized in detail in Chlamydomonas.

Two algal-specific proteins, FEA1 and FEA2, correspond to a third component in the pathway. Both are substantially induced in Chlamydomonas during Fe-deficiency as well (82). Similar proteins have only been found in other green algae (80, 91). The FEA proteins are localized to the periplasm; they are secreted into the growth medium in Chlamydomonas strains that lack a cell wall (82). These strains are also more sensitive to Fe deficiency compared to strains that have a cell wall and retain the FEA proteins, thus implicating the FEAs' involvement in Fe assimilation (82). Consistently, in Arabidopsis and yeast Fe-uptake mutants, heterologous expression of *FEA1* rescued growth phenotypes on Fe-deficient medium (92, 93). Studies suggested that the FEA proteins may be delivering Fe^{3+} to FTR1 and may play a similar role to phytosiderophores in vascular plants (80).

Relatively little is known about the intracellular trafficking of Fe in algae. The two major destinations for Fe in algal cells are the chloroplast and mitochondria, where Fe is required in abundance as a cofactor in many proteins of the respective electron transport chains (1, 94). It is ambiguous how Fe is transported into the chloroplast. Within the chloroplast, ferritin has been attributed to chelating Fe released from degrading proteins (see Section 1.3.2 above). One protein,

MFL1, named for MitoFerrin-Like 1, has been identified as a putative mitochondrial Fe transporter (80).

Other than for utilization such as in the chloroplast and mitochondria, excess Fe is moved into sites of storage, presumably acidocalcisomes. Based on protein similarity networks and comparative transcriptional analyses, several candidate vacuolar Fe transporters have been identified in the Chlamydomonas genome, including NRAMP4, CVL1, and CVL2. These proteins are proton-dependent permeases that mostly transport divalent cations, mainly Fe^{2+} and Mn^{2+} (80, 95, 96). Three NRAMP genes have been found in Chlamydomonas: *NRAMP1*, *NRAMP2*, and *NRAMP4*. Only the expression of *NRAMP4* transcript is increased under Fe deficiency (24). NRAMP4 is also the only member that is orthologous to other eukaryotic NRAMPs, for example, NRAMP3 and NRAMP4 in Arabidopsis (80). The Arabidopsis NRAMP3 and NRAMP4 are likewise induced under Fe deficiency (97, 98), and they have been shown to function in mobilizing Fe from vacuoles during seed germination (99). As such, the Chlamydomonas NRAMP4 is hypothesized to be involved in transporting Fe out of the acidocalcisome. Unlike NRAMP4, the Chlamydomonas NRAMP1 and NRAMP2 are more closely related to the bacterial NRAMP than eukaryotic ones, which prefers Mn transport over Fe (80, 100). In yeast, the expression of *NRAMP1* can fully rescues a strain deficient in Mn transport, but only partially rescues one that is defective in Fe uptake (101). Consistently, the abundances of *NRAMP1* and *NRAMP2* transcripts in algae are increased specifically under Mn limitation (24, 102). That said, their exact functions and locations have not been determined.

The CVL proteins in Chlamydomonas, CVL1 and CVL2, are homologous to the CCC1 transporter in yeast and the VIT1 transporter in Arabidopsis (80). CCC1 is responsible for Fe import into the yeast vacuole (103, 104). The expression of *CCC1* is induced under excess Fe conditions (104). In yeast mutants subjected to excess cytosolic Fe, the over-expression of *CCC1* enables additional Fe sequestration into the vacuole, which helps suppress oxidative stress (104, 105). In Arabidopsis, VIT1 is localized to the vacuolar membrane and plays an essential role in

seed maturation (106). Unlike *CCC1*, the expression of *VIT1* is not dependent on Fe nutrition. Also, the lack of the VIT1 transporter does not affect the total Fe concentration in seeds, but it does impact the distribution of Fe within the seed (106). Interestingly, in contrast to both *CCC1* and *VIT1*, both *CVL1* and *CVL2* in Chlamydomonas are increased in expression under Fe deficiency (24). Like the NRAMP transporters, neither the function nor the location of the CVL proteins in Chlamydomonas has been biochemically confirmed, but based on homology with CCC1 and VIT1, they are hypothesized to mobilize Fe into a vacuole like the acidocalcisome.

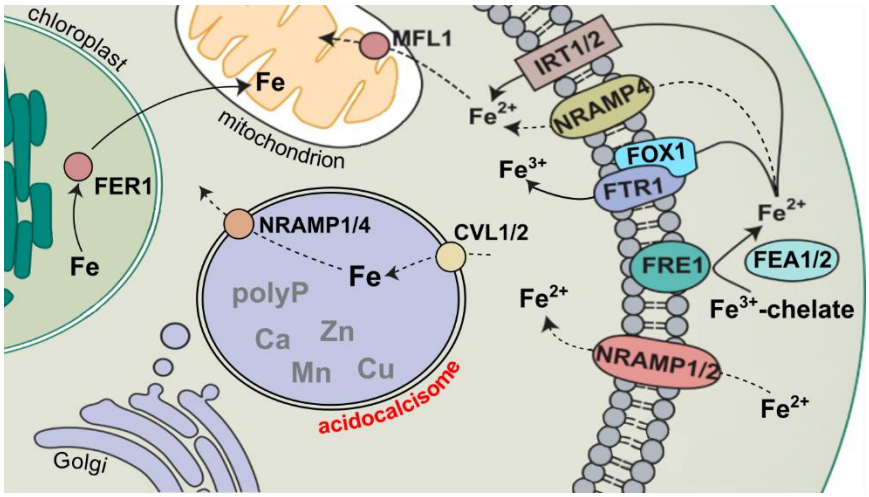

Figure 1.2. Known and candidate Fe homeostasis pathways in Chlamydomonas. Many transporters are involved in Fe assimilation at the plasma membrane and distribution within the cytoplasm and to organelles, including the acidocalcisome (center). The locations of NRAMP, CVL, and MFL1 transporters have not been biochemically validated. The candidate pathways are represented by dash lines, while known ones are shown by solid lines. Figure is modified from Blaby-Haas et al. (80).

1.4 Significance and Specific Aims of the Project

Fe deficiency limits primary productivity on a global scale. Approximately 30% of the oceans and a similar fraction of the world's croplands are Fe-limited (107–109). As a result, photosynthetic organisms, including algae, can be chronically under-nourished for Fe. Meanwhile, algae are broadly distributed in soil, freshwater and marine ecosystems; their growth and energy production, which are heavily impacted by Fe nutrition, contribute significantly to global primary productivity and consequently carbon sequestration, oxygen production, and food chains. Furthermore, as algae can be grown in bulk economically without adding competition for land use with other industries, there is also considerable interest in exploiting their biosynthetic capability for the production of biofuels and other high-value bioproducts (10, 11). To do so effectively and efficiently, it is necessary to first understand algal metabolic regulation and flexibility, especially in response to nutrient variation in diverse niches. Thus, studies of Fe metabolism in algae, particularly the mechanisms underlying Fe recycling and storage, can offer new insights to facilitating the process and application of engineering algae for improved carbon capture capabilities and biofuels.

Aligning with the above mission, the goal of my project is to discover and dissect the mechanisms underlying Fe storage and transport in the unicellular green alga *Chlamydomonas reinhardtii*. I have established three Aims: 1) To analyze systematically the secondary experimental variables stimulating cellular Fe accumulation in Chlamydomonas; 2) To distinguish the roles of acidocalcisomes in Fe storage; and 3) To identify the molecular mechanisms for excess Fe sequestration and mobilization. The background, methods and materials, as well as results and discussion for each of these Aims are presented in the subsequent chapters. Overall, the outcome of my project contributes to our understanding of the fate of Fe from luxury uptake in Chlamydomonas.

CHAPTER 2

Systematic Analysis of Secondary Experimental Variables that Determine Cellular Fe Accumulation

2.1 Background

What variables in the environment or growth milieu affect the Fe content of an algal cell? Beside the extracellular Fe concentration, environmental factors like pH, aeration, and other nutrient availabilities (*e.g.* carbon, nitrogen) can impact Fe bioavailability and/or cell metabolism, which changes the intracellular Fe quota. For example, extracellular pH and temperature can influence the solubility and oxidation state of Fe in the environment, thereby increasing or reducing the amount of Fe that cells can assimilate. Separately, fluxes in O_2/CO_2 supply or light intensity may trigger metabolic changes, which typically involve adjustment in the abundances of proteins in O_2- and CO_2-dependent pathways. This adjustment can in turn affect the trace metal quota in cells, since 40% of all enzymes require trace metal ions as cofactors (110, 111). Thus, the intracellular Fe content can be indirectly affected by various parameters in the environment as cells work to accommodate different fluctuations to continue growth.

In order to accurately address questions concerning the dynamics of Fe homeostasis in Chlamydomonas, the cellular Fe content must be consistently controlled in experiments. As explained above, this task cannot be accomplished solely by controlling the amount of external Fe provided to cells; it is also vital to recognize and control all the other variables in the laboratory set-up that indirectly affect the Fe content of cells. While previous works on Fe homeostasis in Chlamydomonas have revealed qualitatively reproducible results, quantitative variability in the magnitude of cellular Fe accumulation between individual experiments was noted. I hypothesized that the variation observed is a result of unintended changes in secondary experimental variables that were adjusted to accommodate independent experiments. For instance, depending on the quantity of cells or biomass required for downstream analyses, one may collect cell samples at

different timepoints post-inoculation; for instance, when the culture reaches a density that is more convenient for the experimenters. Yet, as cell density changes, the medium pH and the extent of light penetration in the culture also change. By the same reason, the size of the culture vessel and the culture volume can also vary between experiments, which leads to differences in the quantity of light and air accessible to cells. The choice of shaker speed for culturing cells also influences the aeration level. Gas exchange is promoted when the culture vessels are moved along a longer radius. Accordingly, the gas exchange rate from a shaker with a large diameter would be different from one with a smaller diameter moving at the same speed. Meanwhile, light intensity is reduced with increasing distance from a light source. Hence, depending on where the culture vessels are positioned relative to the light source (*e.g.* bulbs in an incubator), the amount of light received by individual cultures can differ. All these subtle variations in cultivation parameters could indirectly impact the cellular Fe content, but the exact effects had not been investigated. Additionally, genomic re-sequencing of 39 common laboratory *C. reinhardtii* strains revealed genetic diversity, consisting of two discrete haplotypes with ~2% sequence variance (112). These strains, albeit all “wild types”, may behave differently with respect to accumulating Fe and other elements.

Therefore, my first Aim was to systematically analyze six cultivation parameters for their impact on Fe accumulation in wild-type Chlamydomonas. The sets of tested variables included 1) cell density and sampling time, 2) growth medium pH, 3) photon flux density (PFD), 4) parameters affecting aeration, including culture volume, vessel size, and shaker speed, 5) temperature, and 6) strain background. These parameters are frequently varied between individual experiments. Yet, they are often documented merely as associated metadata or even neglected, despite their potential effect on cell growth, metabolism, and trace metal quota. In parallel, to assess whether any effect from the tested variables might also be influenced by external Fe concentration, all experiments were performed under two Fe supplement regimes: 1) the standard Fe-replete condition, and 2) the Fe-excess condition (20 and 200 μM medium Fe, respectively). These two

conditions were chosen because the cells are otherwise phenotypically identical (see Section 1.3.1), which simplified data comparison. Note that Fe-EDTA was used as the Fe source in the growth medium, which is more soluble than most other forms of Fe typically encountered in nature, namely oxides and hydroxides (113, 114). While Chlamydomonas has the capacity to extract the Fe atoms from EDTA for uptake (115), this capability should not be taken for granted; the green algae *Scenedesmus*, for instance, cannot utilize chelated copper (Cu) (116).

To accomplish this Aim, each sample's growth physiology and elemental composition, measured by ICP-MS/MS (inductively coupled plasma tandem mass spectrometry analysis), was recorded. Briefly, ICP-MS/MS is a hard ionization mass spectrometry technique for elemental analysis in liquid samples, such as acid-digested cells (117). It is equipped with two quadrupole mass filters with a collision/reaction cell in between, which collectively remove interfering ions. ICP-MS/MS has a high detection power and a wide linear dynamic range (over several orders of magnitude) for most elements, thus making it an excellent technique for determining ultra-trace levels of metals in biological samples (117, 118).

The outcomes of this analysis identified some common experimental variables that affect the intracellular Fe and other trace metal content in Chlamydomonas. Based on these results, I have also determined the experimental setups under which cells consistently over-accumulate the same amount of Fe. These setups were used to address questions in Aim 2 and 3 regarding the site of Fe storage and the components and dynamics of excess Fe mobilization.

2.2 Methods and Materials

2.2.1 Strains

Wild-type *Chlamydomonas reinhardtii* strain CC-4533 was used for all experiments. When analyzing the diversity among laboratory strains, CC-4533 was compared with six other wild-type strains, including CC-4532, CC-124, CC-125, CC-1009, CC-1690, and CC-1691, all obtained from

the Chlamydomonas Resource Center (http://chlamycollection.org/). The rationale for choosing these strains is presented in Section 2.2.3.

2.2.2 Standard culture conditions

Unless specified otherwise, cells were inoculated at 1 x 10^4 cells/ml in 100 ml of Tris-acetate-phosphate (TAP) medium (119) in a 250-ml Erlenmeyer flask, titrated to pH 7.0 with trace metal grade acetic acid (Fisher, A507-P212) and KOH. The TAP medium contained the revised micronutrient composition according to (25), with either 20 µM Fe-EDTA (replete condition) or 200 µM Fe-EDTA (excess condition). Cells were inoculated from a liquid pre-growth culture in TAP with 20 µM Fe that was at a cell density of 2-4 x 10^6 cells/ml. The cultures were grown in an Innova 44R incubator (New Brunswick Scientific) at 24ºC under constant agitation at 180 RPM and continuous illumination at 80-95 µmol photons·m^{-2}·s^{-1}. Photon flux density (PFD) was measured in separate cell-free TAP medium. For the light spectrum shown in Figure 2.1, two cool white fluorescent bulbs at 4,100 K were used for each warm white fluorescent bulb at 3,000 K. For all experiments, three independent cultures were inoculated and grown in parallel in random positions in the incubator at the same PFD.

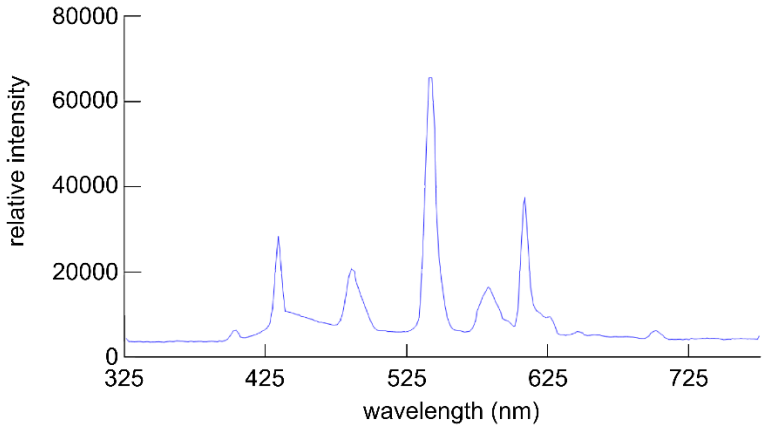

Figure 2.1. The light quality spectrum of the incubator used in all experiments. The light spectrum applied during cell cultivation for all experiments was measured using the SpectraPen SP 110. The probe was placed in the center of the incubator where cultures were positioned.

2.2.3 Systematic analysis of growth conditions

Each experiment presented in this chapter had a single cultivation parameter varied (listed below), while all other parameters were maintained as described above. If not stated otherwise, cells were visually examined and counted every 24 h post-inoculation for 1 week, and they were sampled for ICP-MS/MS during mid-log growth (2-4 x 10^6 cells/ml).

Variable changed:

i) Cell density and sampling time: Cells were grown, counted, and sampled for ICP-MS/MS analysis when they reached the following cell density checkpoints: 1 x 10^6, 2 x 10^6, 4 x 10^6, 6 x 10^6, 8 x 10^6, 12 x 10^6, and 14 x 10^6 cells/ml, and then for 3 additional days during stationary phase at a 24-h interval (1-week of monitoring in total)

ii) Growth medium pH: Fresh TAP medium was titrated to either pH 7.0 or pH 8.5 prior to inoculation. The pH of spent medium from the cultures was recorded every day for one week around the same time when cells were counted.

iii) PFD: Cultures were grown from inoculation to sampling in constant illumination at 30, 50, 95, or 180 $\mu mol \cdot m^{-2} \cdot s^{-1}$, measured in TAP medium without cells. The medium used for quantifying PFD was discarded afterward; fresh TAP medium was prepared for cell inoculation to prevent contamination.

iv) Culture volume: 25, 50, 100, 150, and 200 ml of fresh medium were put in individual 250-ml Erlenmeyer flasks. Inoculant density was maintained at 1 x 10^4 cells/ml in each vessel.

v) Vessel size: 125-, 250-, 500-, 1000-ml Erlenmeyer and 2800-ml Fernbach flasks were used, with each flask containing medium representing 40% of the vessel volume.

vi) Shaker speed: Cultures were grown in incubators shaking at 0, 60, 120, 140, 160, and 180 RPM.

vii) Temperature: Cultures were grown at 18, 21, 24, 27, and 30ºC.

viii) Strain background: Six different laboratory wild-types strains were compared to CC-4533, including CC-4532, CC-124, CC-125, CC-1009, CC-1690, and CC-1691. The CC-4533 strain represents the wild-type parent of a collection of publicly available insertion mutants (17, 18), which were used in Aim 3. The CC-4532 strain is a wild-type reference commonly used for trace metal studies in Chlamydomonas. The CC-124, CC-125, CC-1009, CC-1690, and CC-1691 strains each represent a distinct lineage among the different Chlamydomonas wild-type strains (112) (more on strain backgrounds in Section 2.3.5).

2.2.4 Determination of growth rate and number of generations

Cells in each culture were manually counted using a hemocytometer. A 1-ml aliquot of each culture, thoroughly mixed, was treated with 3-10 µL of iodine solution (0.25 g iodine in 100 mL 95% EtOH) to stain and immobilize cells. 10 µL of the stained cells was loaded into the counting chamber of the hemocytometer. The aliquot was diluted with TAP medium as needed, so that at most ~100 cells were counted in each measurement.

Doubling time, used as a measure for growth rate, was calculated between consecutive time points during log growth phase by $k = t \log(2)/(\log(O_t) - \log(O_0))$, where *k* is the doubling time, *t* is the duration in hour between the initial and new measurements, and O_t and O_0 are the culture densities at the time of the new and initial measurement, respectively.

The number of generations from the time of inoculation until stationary growth phase was calculated by $n = \log(O_f/O_0)/\log(2)$, where *n* is the number of generations, O_f is the stationary cell density, and O_0 is the inoculant density.

2.2.5 Quantitative elemental content analysis

Trace metal composition including iron (Fe), copper (Cu), zinc (Zn), and manganese (Mn), as well as the abundances of macronutrients sulfur (S), calcium (Ca), and phosphorous (P) were

determined by ICP-MS/MS as described in (120) with minor modifications. Briefly, 5 x 10^7 cells were collected by centrifugation at 2,600 x*g* for 3 min. Spent medium, 2 ml from each sample, was collected and diluted to 7 ml with Milli-Q water containing Optima grade nitric acid (Fisher, A467-500, final concentration 2% nitric acid). The cell pellets were washed twice with 1 mM Na_2-EDTA to remove cell surface-associated metals and once with Milli-Q water. The washed cell pellet was overlaid with 143 µl of 70% nitric acid (Optima grade, Fisher, A467-500) and digested at room temperature overnight, followed by a 2 h incubation at 65ºC. The cell hydrolysate was diluted to 5 ml with Milli-Q water (final nitric acid concentration of 2%).

Fe, Cu, Zn, Mn, S, Ca, and P contents in each of the spent media and cell lysates were measured by ICP-MS/MS on an Agilent 8800 or Agilent 8900 instrument in 3-5 technical replicates. The average variation between the technical replicate measurements was below 2% for all analytes and never exceeded 5% for an individual sample. A dilution series of an environmental calibration standard (Agilent 5183-4688), a sulfur (Inorganic Ventures CGS1) and a phosphorus (Inorganic Ventures CGP1) standard was used for quantification. ^{45}Sc and ^{89}Y were used as internal standards (Inorganic Ventures MSY-100PPM, MSSC-100PPM) to account for sample composition differences between standards and cell lysates. The total content of all analytes in the samples was determined in MS/MS mode: ^{40}Ca and ^{56}Fe were determined directly using H_2 as a cell gas, whereas ^{55}Mn, ^{63}Cu, and ^{66}Zn were measured using He in the collision cell, and ^{31}P and ^{32}S were determined via mass-shift from 31 to 47 and 32 to 48, respectively, using O_2 as a cell gas.

The data were analyzed with Masshunter (Agilent, v4.4), Microsoft Excel, and OriginPro 9.1 (OriginLab). Trace metal, Ca and P contents were normalized to the S content of the same sample if cellular S content correlated linearly with cell number and total organic carbon (TOC) content and was similar in all samples. This was the case in the experiments testing cell density/sampling time, pH, PFD, all the aeration parameters, and strain background. However, in the experiment investigating the effect of temperature, the cellular S content changed as

temperature varied and did not correlate strongly to TOC content; cell number was thus used as a normalization factor.

2.2.6 Total organic carbon (TOC) content analysis

Total, non-purgeable organic carbon content of the cells was determined as described in (121) on a Shimadzu TOC-L/TN CSH analyzer with the following modifications. The cell lysates prepared and used for ICP-MS/MS described in Section 2.2.5 were subsequently used for total organic carbon (TOC) analysis. 500 µl of each digested sample from the ICP-MS/MS analysis (in 2% nitric acid) was diluted with 14.37 ml of Milli-Q water and 135 µl of 3M HCl (to a final HCl concentration of 27 mM). A 2% nitric acid solution was diluted likewise as a blank. Samples were sparged with purified air to remove inorganic carbon. Some volatile organic compounds, such as methanol and ethanol, might be purged from the samples. A standard curve from 0.5 to 25 ppm carbon from Potassium Hydrogen Phthalate was used for quantification. The carbon content measured by TOC analysis was plotted against the sulfur content of the same sample measured by ICP-MS/MS to evaluate correlation. Data were analyzed in Microsoft Excel and OriginPro 9.1 (OriginLab).

2.2.7 TAP medium titration

To assess the pH at which Fe precipitates in TAP medium, a flask of fresh TAP medium with 200 µM Fe was prepared and titrated to 8.5, 9.0, 9.5, 10.0, 10.5, and 11.0 with KOH. In the reverse direction, to assess whether any Fe precipitate is re-solubilized in acidified medium, fresh TAP medium at pH 11.0 was titrated to pH 10.5, 10.0, 9.5, 9.0, and 8.5 with acetic acid. The media were undisturbed at each titration point for 30 mins at room temperature, and then 4 ml of each medium was collected, of which 2 ml was filtered through a 0.22 µm filter. Both the filtered and unfiltered samples were analyzed by ICP-MS/MS to evaluate their soluble Fe content.

2.3 Results and Discussion

2.3.1 Cellular Fe, Cu, and Zn contents increase with time during stationary growth.

The growth of Chlamydomonas cells was monitored under both replete and excess Fe conditions (20 vs. 200 μM Fe, respectively). Consistent with previous studies (21, 23), cells grew at virtually the same rate under both Fe conditions, with a doubling time of 7-8 hours and with the same number of total generations (Figure 2.2A-C). To understand how Fe content changed in Chlamydomonas cells as they grew, cells were sampled for ICP-MS/MS analysis at various densities (1, 2, 4, 6, 8, 12, and 14 x 10^6 cells/ml) and at a 24-h interval for 3 additional days during stationary phase. The data showed that the amount of cellular sulfur (S) was about constant across different sampling times and was similar between replete and excess Fe conditions (Supplementary Figure 1). Thus, S was used as a normalization factor for all other elements in this ICP-MS/MS analysis.

The ICP-MS/MS data revealed that cellular Fe content increased as cells grew, but most significantly during stationary phase. Interestingly, in stationary phase, the cellular Fe content increased linearly with respect to time (Figure 2.2D) and not with cell density per se (Figure 2.3A). Furthermore, the extent of how much Fe accumulated in cells was influenced by the medium Fe concentration. Under excess Fe condition, cells were able to accumulate 3-fold more Fe after 4 days into stationary phase compared to the beginning of log phase. In comparison, cells grown under replete Fe condition accumulated only ~2-fold more Fe in the same period of time.

In a similar pattern to Fe, cellular Cu and Zn contents also increased 2-3-fold from log to stationary phase, with the increase occurred mainly during stationary phase, linearly with respect to time but not to cell density (Figure 2.2E-F, Figure 2.3B-C). The accumulation of Cu in cells was slightly greater under the replete Fe condition than in the excess Fe condition, while the accumulation of Zn was unaffected by medium Fe concentration. In contrast to Fe, Cu, and Zn, the level of cellular Mn was relatively constant from log to stationary phase and was similar under both replete and excess Fe conditions (Figure 2.2G, Figure 2.3D).

Because of my interest in the acidocalcisome, which contains a high amount of Ca and polyP, I have also examined how secondary cultivation parameters would affect the accumulation of Ca and P. Cells accumulated ~2-fold more Ca and ~1.5-fold more P when they first entered stationary phase than they did in log phase, but this higher level of Ca and P was maintained thereafter (Figure 2.2H-I, Figure 2.3E-F).

The continued import of Fe, Cu, and Zn during stationary phase, *i.e.* when cells have stopped dividing, is intriguing, given that metal overload could lead to deleterious effects, in particular ROS-induced damages. *S. cerevisiae* has also been found to accumulate Fe linearly with time during post-exponential growth (122). It is hypothesized that the high-affinity Fe import pathway in *S. cerevisiae* turns off more subtly than the decline in the rate of cell growth, causing cells to continue Fe import during stationary growth. It is therefore possible that the transport of Fe in Chlamydomonas likewise does not synchronize with the growth rate of cells, leading to increased import of the metals after the cells refrain from dividing. However, to test this hypothesis, one must first document all Fe transport pathways and then probe for the rate and extent of Fe transport attributed to each component. Meanwhile, Fe is almost always scarce in nature and a limiting factor for growth to photosynthetic organisms (107–109). Thus, it is likely that organisms have evolved to deliberately allow a moderate excess of Fe to be accumulated within the cell in face of potential supply fluctuation and starvation (1, 6). This is another plausible explanation for the 2- to 3-fold increase in cellular Fe content observed during stationary phase.

For similar reasons, Cu and Zn might accumulate in slight excess in cells as well, even though the requirement for Cu and Zn in cells is about 10 times lower than that of Fe under standard growth mode (123). The observation that having a replete vs. excess amount of Fe in the medium subtly affected Cu accumulation during stationary phase hints to linkage between Fe and Cu transport in cells under these conditions.

Curiously, Mn accumulation did not follow the same pattern as Fe, Cu, and Zn; cellular Mn content remained relatively constant from log to stationary phase, even though Chlamydomonas

does have a high Mn requirement (62, 123, 124). Uptake kinetics data suggested that Chlamydomonas cells might be maintaining a strict cellular Mn quota by adjusting the rate for transport (V_{max}) through a negative feedback control (125). In Arabidopsis, the Mn transporter NRMAP1 cycles dynamically between the plasma membrane and endosomal compartments in response to Mn availability to control uptake and prevent toxicity (126). The localization and function of the Chlamydomonas NRAMP1, however, has not been confirmed. Additionally, Mn accumulation was unaffected by external Fe concentration when both trace metals were supplied at replete or higher level, despite there being an overlap of transporters used for the two metals (80). It has been shown that Mn deficiency induces secondary Fe deficiency, and provision of extra Fe can at least partially rescue phenotypes of Mn-deficient cells (124). Thus, Mn homeostasis might be impactfully affected by Fe nutrition only in an Fe-limited state.

In the meantime, the unchanged cellular Ca and P content during stationary phase was not unexpected, given the tight regulation of Ca and P in photosynthetic cells. An excess of either element would lead to toxicity, change in cytosolic pH, and disruption in ion balances and uptake of other essential nutrients (*e.g.* Fe) (127–129). Nevertheless, the increased accumulation of Ca and P from log to stationary phase suggested that the two macronutrients might be needed in the cells especially during stationary phase, perhaps for the synthesis of acidocalcisomes and general storage of metabolites. In (130), the authors showed by quick-freeze deep-etch electron microscopy an abundance of polyP granules-containing acidocalcisomes in Chlamydomonas cells collected from stationary phase, but not in cells from log phase. These acidocalcisomes could be functioning as a storage site for polyP and Ca. They might also be a potential reservoir for other micronutrients accumulated during stationary phase, such as Fe. This subject was further investigated and is discussed in Chapter 3.

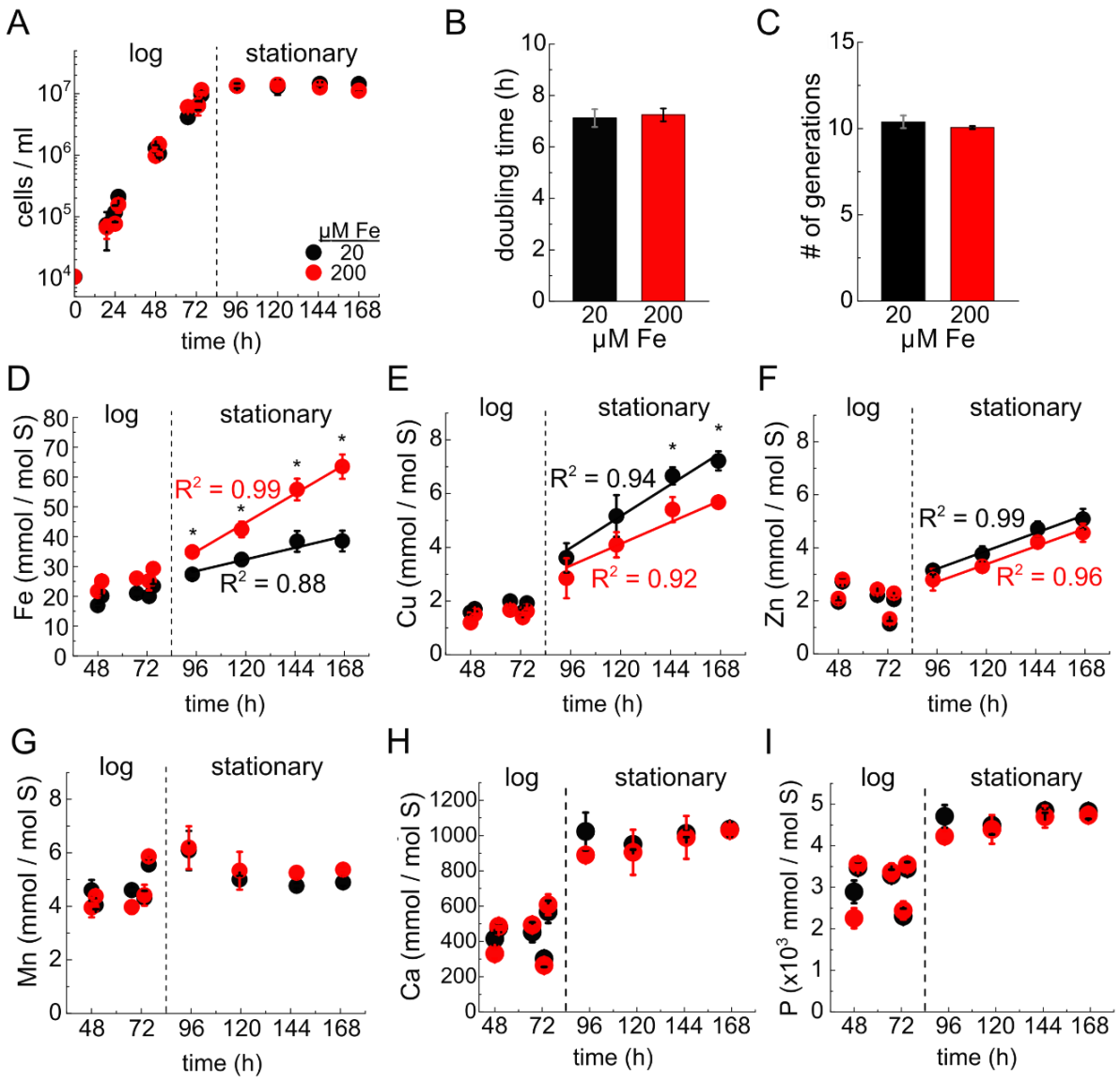

Figure 2.2. Fe, Cu, and Zn accumulate in stationary phase linearly with respect to time. (A) Growth curve. Cultures of wild-type Chlamydomonas (CC-4533) grown in 20 (black) or 200 (red) μM Fe-containing media were sampled at the indicated hours post-inoculation. The doubling time is shown in (B). The total number of generations until stationary phase of cells is shown in (C). (D-I) Fe (D), Cu (E), Zn (F), Mn (G), Ca (H), and P (I) contents associated with the cells were measured by ICP-MS/MS and are presented normalized to the S content of the cells. Asterisks indicate significant differences (t-test, $p \leq 0.05$) between the 20 and 200 μM Fe conditions. Averages are shown with error bars indicating standard deviation of 3 independent cultures. R^2 values correspond to linear regression fitting of the time points in stationary phase.

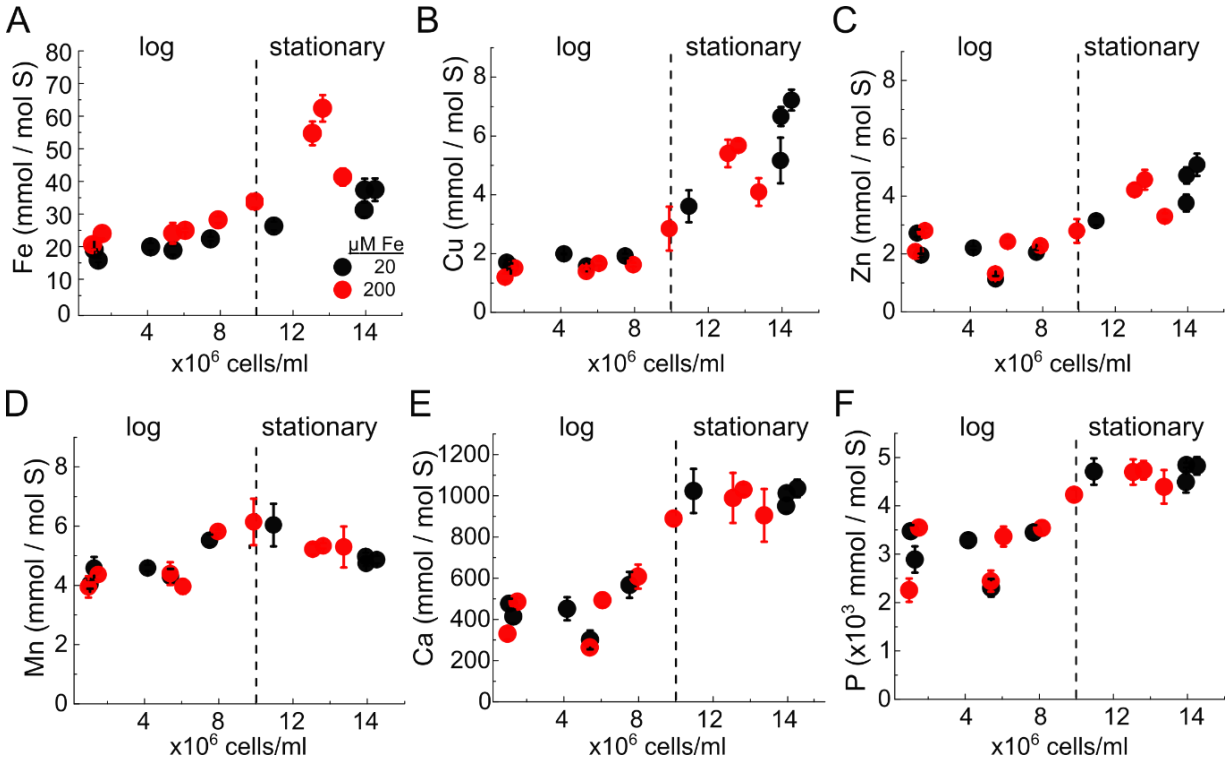

Figure 2.3. The increase of Fe, Cu, and Zn in cells does not depend on cell density per se. Cell grown in 20 (black) or 200 (red) μM Fe-containing media were sampled at the indicated culture densities. Cell-associated Fe, Cu, Zn, Mn, Ca, and P contents were measured by ICP-MS/MS and normalized to cellular S content. Averages are shown with error bars indicating standard deviation of 3 independent cultures.

2.3.2 Cells specifically over-accumulate Fe under alkaline pH condition.

The Chlamydomonas TAP growth medium uses Tris/acetate as its major buffer system. The medium becomes gradually more alkaline when cells consume the acetate as a source of reduced carbon. pH affects Fe solubility, which can consequently impact the bioavailability of Fe, as well as how cells assimilate Fe and grow (131). Therefore, I first monitored how exactly the TAP medium pH changed as cells grew photoheterotrophically. When cells were inoculated into TAP medium adjusted to pH 7.0, the medium pH increased to about 8.5 by the time cells entered late stationary phase (1-week from the time of inoculation); when cells were inoculated directly into medium at pH 8.5, the medium pH increased ~2.5 units in the same period of time (Figure 2.4A). Whether there was a replete or excess amount of Fe in the medium (20 vs. 200μM, respectively) did not affect the change in medium pH. The greater amplitude of change in medium

pH under an alkaline condition is probably largely attributed to the fact that Tris, with a pK_a of 8.1, does not have good buffer capacity above pH 9.

In terms of growth, the doubling time of cells inoculated into the pH 8.5 medium was i) significantly longer than the cells inoculated into the pH 7.0 medium, and ii) dependent on the medium Fe concentration (~10 h under replete Fe condition vs. ~14 h under excess Fe condition) (Figure 2.4B). However, cells in all cultures eventually produced the same number of generations (Figure 2.4C). No chlorosis was evident in any cultures (data not shown).

The elemental content of cells was analyzed by ICP-MS/MS and TOC. The cellular S content, measured by ICP-MS/MS, correlated well with the biomass of cells, which was quantified by TOC as non-purgeable organic carbon (Supplementary Figure 2). The strong correlation allowed the use of cellular S for normalization for the other elements in the analysis. Interestingly, cells inoculated into alkaline medium accumulated more biomass and S during log phase than did cells inoculated into the neutral medium (Supplementary Figure 2). However, this phenomenon was only temporary; in stationary phase, the S and C contents in the alkaline medium-inoculated cells were reduced to the level observed in the neutral medium-inoculated cells.

From the ICP-MS/MS analysis, the most notable result was that the cells experiencing alkaline stress accumulated drastically more Fe compared to cells inoculated into the neutral medium (Figure 2.5A). Also, the extent of how much excess Fe was taken up by the cells was dependent on external Fe concentration. This over-accumulation effect appeared to be Fe-specific; the cellular Cu, Zn, and Mn levels did not differ significantly between samples in the alkaline vs. neutral pH medium (Figure 2.5B-D). Difference in the medium Fe concentration did not make an impact on the accumulation of these metals either. In contrast, Ca and P contents decreased 10-fold and 2-fold, respectively, in cells inoculated into the alkaline medium compared to the cells inoculated into the neutral medium (Figure 2.4E-F).

Since Fe solubility is reduced with increasing pH, it was possible that the Fe observed in the ICP-MS/MS measurements was merely the result of precipitation during sampling. To determine whether this was the case, standard pH 7.0 TAP medium was titrated to pH 8.5, 9.0, 9.5, 10.0, 10.5, and 11.0. To assess whether any precipitated Fe could be re-solubilized at neutral pH, a separate batch of the different alkaline media were also titrated back to pH 7.0. The medium samples were analyzed for aggregates from precipitation by filtration through 0.22 µm filters. The ICP-MS/MS results indicated that at pH 8.5 in TAP with 200 µM Fe, there was no aggregation of Fe (Supplementary Figure 3). Fe significantly aggregated when the medium pH surpassed 9.5, and acidification back to pH 7.0 did not re-solubilize the precipitated Fe (Supplementary Figure 3). All ICP-MS/MS cell samples for the pH experiment were collected during mid-log growth (~70 h and ~90 h post-inoculation under neutral and alkaline condition, respectively). At that point, the medium pH of the cultures under alkaline condition was only between 8.5 and 9.0 (Figure 2.4A). As such, the excess Fe associated with the alkaline pH cell samples in the ICP-MS/MS measurements was unlikely to be a result of precipitation.

The slower growth of cells under alkaline vs. neutral pH condition is consistent with previous studies, which indicated that the optimal pH for Chlamydomonas growth is ~6.7, and deviation from this pH reduces growth rate (132, 133). Other studies on metal uptake in relation to algal growth suggested that the toxicity of Cu and Zn increases with elevating medium pH due to metal speciation (134–136). Ion gradients across the plasma membrane and/or internal organelle boundary membrane could be impacted as well due to the increased pH (137, 138). These might be additional factors contributing to the slower growth of cells under alkaline stress. Meanwhile, the further reduced cell growth in alkaline medium when excess Fe was provided hints to toxicity related to the over-accumulation of Fe. In addition to the impact of Fe on ROS production in aerobic cells, overloading Fe in cells can result in disruption in the uptake of other essential nutrients, such as nitrogen and P, which would slow growth (139–141). In plants, while Fe deficiency can lead to chlorosis due to restricted expression of essential Fe-containing

enzymes in the plastids (*e.g.* ferredoxins) (142, 143), excess Fe can also hinder the biosynthesis of chlorophyll and other photosynthetic pigments due to elevated ROS production (144). However, chlorosis was not observed in the Chlamydomonas cultures under alkaline condition in this experiment, suggesting that at least chlorophyll production was not affected, potentially because ROS production was limited as excess Fe was safely stowed away.

The specific over-accumulation of Fe in cells in the alkaline medium is intriguing and counter-intuitive, because alkaline pH reduces Fe solubility and would typically lower Fe bioavailability. Plants grown in alkaline soil are usually chlorotic due to limiting Fe acquisition and the consequential Fe deficiency (106, 145, 146). As a solution, plants can try to increase Fe solubility in the rhizosphere by inducing outward proton fluxes via the plasma membrane ATPases to acidify soil (147, 148). Yet, as mentioned, the Chlamydomonas cultures in this experiment were not chlorotic. Indeed, the Fe in the TAP medium was still soluble for the most part of the cells' growth cycle; even when the medium pH reached 11, a considerable portion of the Fe pool was still found in solution (Supplementary Figure 3). The Fe^{3+}-EDTA used in the TAP medium is more stable and soluble between pH 7-9 than the Fe that organisms would encounter in nature (149, 150). This likely helps preserve Fe bioavailability in moderate alkaline conditions, thereby allowing cells to continue uptake as desired and prevent chlorosis. Supporting this notion, studies have shown that *S. cerevisiae* has a greater tolerance for alkaline stress when Fe uptake is improved, either by overexpressing Fe transport proteins or by supplying additional Fe to the growth medium (151–153). The underlying mechanism by which Chlamydomonas cells could over-accumulate Fe in alkaline condition was investigated by a comparative transcriptomic analysis of cells grown at pH 8.5 vs. 7.0. The results are shown and discussed in Chapter 4.

Separately, the reduced Ca and P contents in Chlamydomonas cells under alkaline condition might be explained by a disrupted electrochemical gradient between the cytosol and vacuoles, like acidocalcisomes. A substantial fraction of the cellular P and most of the intracellular Ca are found within acidocalcisomes in Chlamydomonas (63). Also, in both *S. cerevisiae* and

Chlamydomonas, acidic vacuoles and acidocalcisomes have been linked to the entry and storage of Ca as well as polyP (69, 128, 151, 154–156). Exposure to high external pH might cause an imbalance of intracellular protons and/or other cations, disturbing the biochemistry that is required for functional transport of Ca, P, and other nutrients. Impaired acidocalcisomes might also lead to degradation of polyP stock and contribute to a lower P level in the cells, a phenomenon that has been described in *S. cerevisiae* when medium alkalinizes (151, 157). However, it is worth noting that a reduced content of Ca and P does not preclude the formation of acidocalcisomes. In the Chlamydomonas *vtc1* mutant strain, which is defective in Ca and P accumulation, acidic compartments have been observed (62, 63). Whether the acidocalcisome might be a storage site for the excess Fe that cells accumulated under alkaline condition was investigated by a variety of elemental imaging analyses. The results are reported in Chapter 3.

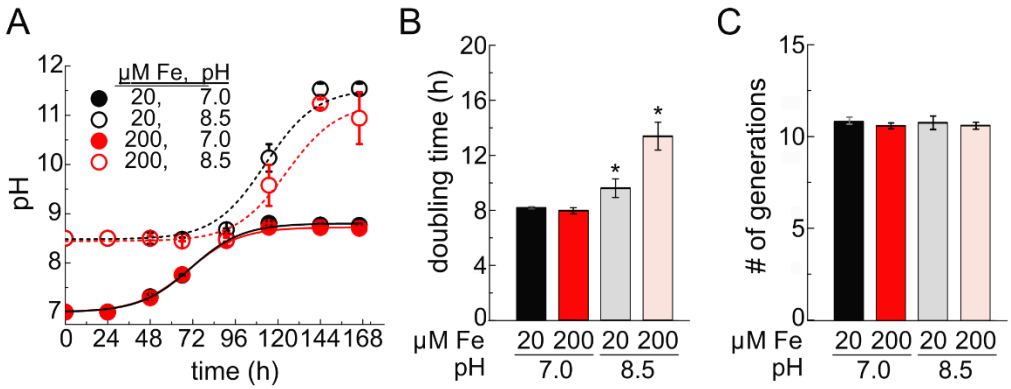

Figure 2.4. Chlamydomonas cells acclimate slowly to an alkaline environment. (A) A record of the pH of spent media, collected at the indicated timepoints post-inoculation from media containing 20 (black) or 200 (red) μM Fe, starting at either pH 7.0 (filled circles) or pH 8.5 (open circles). Solid and dotted lines represent exponential fittings for the pH values. (B) Doubling time and (C) number of generations until stationary phase of cells grown in TAP at the indicated Fe concentrations and starting medium pH. Asterisks indicate significant differences (t-test, $p \leq 0.05$) to cells grown in 20 μM Fe at pH 7.0. Averages are shown with error bars indicating standard deviation of 3 independent cultures.

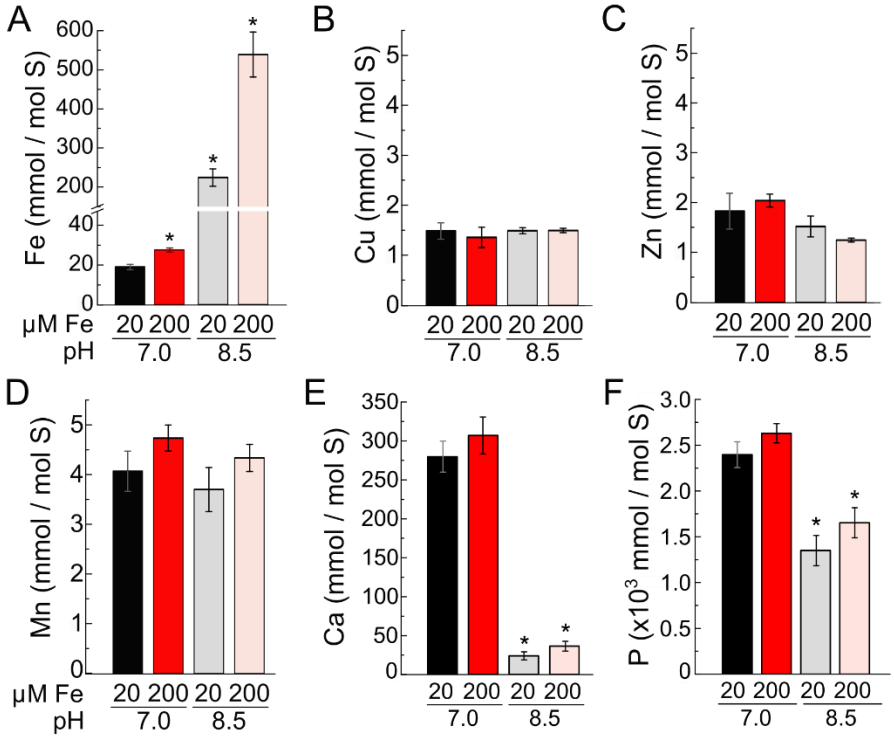

Figure 2.5. Cells in alkaline medium over-accumulate Fe and have reduced Ca and P. (A-F) Abundances of Fe (A), Cu (B), Zn (C), Mn (D), Ca (E), and P (F) associated with the same cells described in Figure 2.4, as measured by ICP-MS/MS. The cells were collected during mid-log growth (2-4 x 10^6 cells/ml). The corresponding Fe concentration and pH of the growth media are as indicated. Asterisks represent significant differences (t-test, $p \leq 0.05$) to cells grown in 20 μM Fe at pH 7.0. Averages are shown with error bars indicating standard deviation of 3 independent cultures.

2.3.3 Cell growth and Fe content are largely unaffected by moderate variations in photon flux density and aeration parameters.

Photon Flux Density:

The quantity of light accessible to cells depends on the intensity of the light source and where the culture vessel is placed with respect to the light source, in terms of both distance and angle. The farther away a culture is placed from the light source, the weaker the light it perceived. Meanwhile, as the angle of incidence increases, the transmission of light decreases. The properties of the vessel and the positions of other objects in the vicinity (*e.g.* other cultures) also influence the actual amount of light received by the culture. Within an illuminated incubator, the cultures placed along the edges and in the corners generally receive less light than those positioned in the center, as bulbs are typically installed on the top center of the incubator. Furthermore, a shading effect arises in liquid cultures when culture density increases, since light penetration decreases proportionally (Figure 2.6A). Such variations in light intensity are often inevitable when cultivating cells, but they do contribute to the overall differentiation between cultures grown in parallel. In order to study the impact of light intensity on trace metal content, I have monitored Chlamydomonas cultures grown under an array of different PFD in the same incubator (30, 50, 95, and 180 μmol photon·m^{-2}·s^{-1}), and have analyzed their elemental composition by ICP-MS/MS. In this experiment, the light quality was maintained the same for all cultures (Figure 2.1), and other indirect effects on light intensity within the incubator were mitigated.

The results, taken together, showed minor impacts from variations in light intensity, at least in the tested range, on cell growth and elemental composition. Neither growth, assessed by doubling time and number of generations (Figure 2.6B-C), nor the accumulation of Fe or Cu (Figure 2.6D-E) was significantly affected by the tested differences in PFD. Cells grown under low PFDs (30 and 50 μmol·m^{-2}·s^{-1}) appeared to have less Zn compared to the reference cells grown under standard light intensity (95 μmol·m^{-2}·s^{-1}) (Figure 2.6F). Interestingly, Zn levels almost

doubled in cells grown under 180 μmol·m^{-2}·s^{-1} compared to the reference cells under replete Fe condition, but not when excess Fe was provided. A similar occurrence was also observed with Ca content (Figure 2.6H). Meanwhile, cells seemed to accumulate marginally more Mn as PFD increased (Figure 2.6G). While cellular P content was unchanged by the varied PFDs under replete Fe condition, some fluctuations were noted under excess Fe condition (Figure 2.6I). S content of cells under each light condition was similar and was used for normalization (Supplementary Figure 4A).

Some studies have reported changes in the metal nutrition of photosynthetic organisms in response to variations in light intensity (23, 158–162). However, frequently either very weak or more intense incident lights (*e.g.* below 25 and above 400 μmol·m^{-2}·s^{-1}) are used in these experiments. Such intensities of light typically induce low or high light stress in cells, which is often accompanied by significant, observable molecular changes. In comparison, potential impacts of moderate variations in light intensity are under-investigated. The data presented here showed that Chlamydomonas cells grow well and have a largely similar trace metal profile when given light between 30 and 180 μmol photons·m^{-2}·s^{-1}. Yet, substantial alterations in metabolite levels and protein abundances (*e.g.* those involved in photosynthesis) have been observed within this range of PFDs (163). Given my results, however, these changes do not appear to hugely affect the trace metal content. Likewise, whether cells were supplied with replete or excess Fe in the medium did not produce vastly different results in the accumulation of trace metals, Ca, and P either.

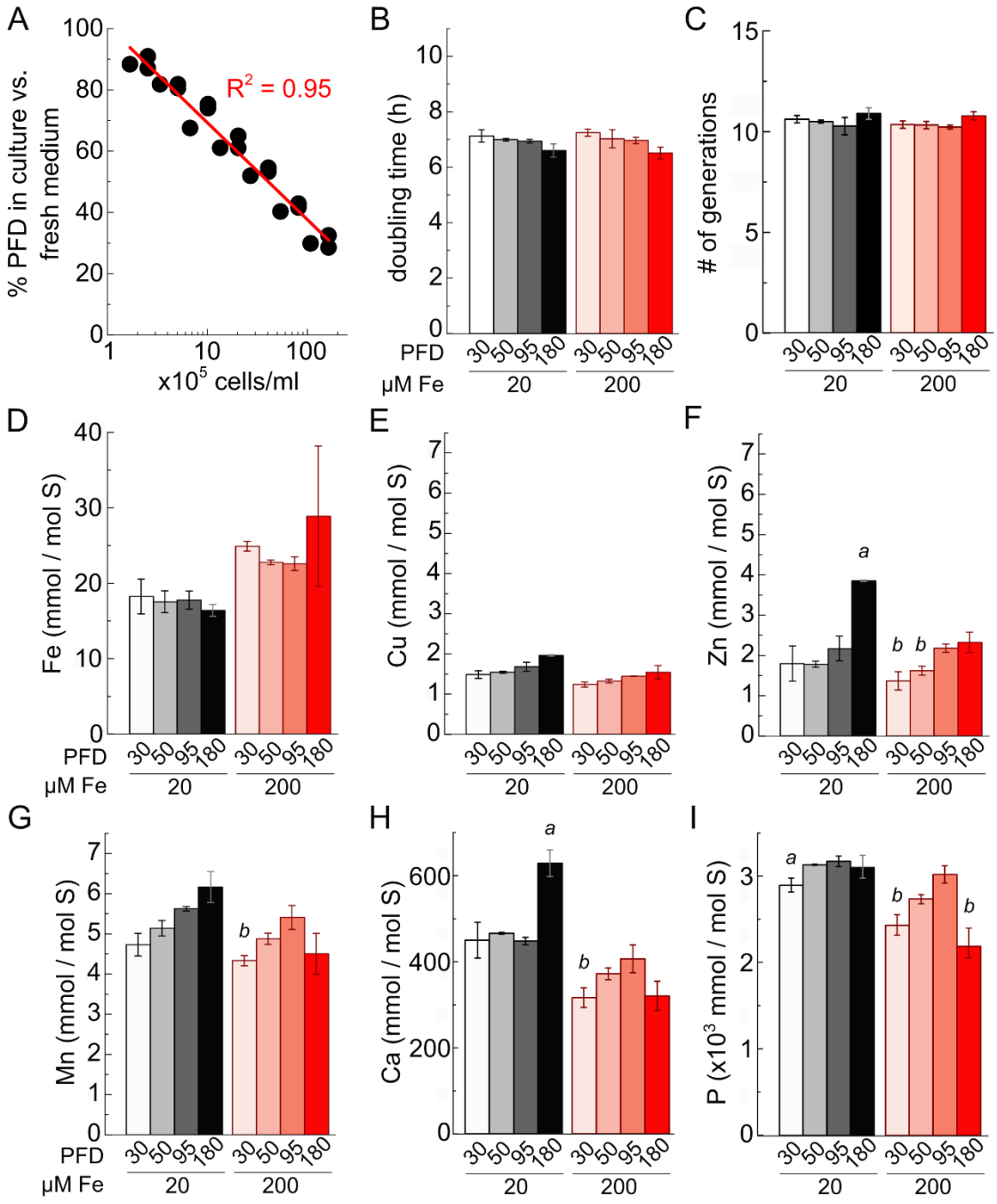

Figure 2.6. Moderate variations in PFD does not impact cell growth or Fe accumulation. (A) Photon flux density (PFD, in μmol photons·m^{-2}·s^{-1}) in CC-4533 cultures at different densities as a percentage of PFD permittable in fresh medium. Data points represent measurements from 3 cultural replicates. R^2 value corresponds to linear regression fitting of the data points. (B) Doubling time and (C) number of generations until stationary phase of cells grown in media containing 20 or 200 μM Fe at the indicated PFDs, measured inside medium. (D-I) Cell-associated Fe (D), Cu (E), Zn (F), Mn (G), Ca (H), and P (I) abundance as measured by ICP-MS/MS, collected during mid-log growth (2-4 x 10^6 cells/ml). *a* and *b* indicate significant differences (t-test, $p \leq 0.017$, multiple Bonferroni-corrected) to cells grown in 20 μM Fe at 95 μmol m^{-2} s^{-1} (*a*) and to 200 μM Fe at 95 μmol m^{-2} s^{-1} (*b*). Averages are shown with error bars indicating standard deviation of 3 independent cultures.

Aeration (Culture Volume, Vessel Size, Shaker Speed):

I have also analyzed the impact of i) culture volume, ii) vessel size, and iii) shaker speed on Chlamydomonas cultures, as these parameters can predominately alter aeration during cell cultivation and are often varied between experiments, depending on the operator's goals and needs.

Overall, as with PFD, variations in these parameters in the tested ranges have only minor effects on cell growth and elemental composition. In terms of growth, doubling times increased by ~1.5 h when cells were grown in Erlenmeyer flasks filled with growth medium equivalent to 60% or more of the flask's volume (Figure 2.7A). However, compared to the standard 40% fill level, the growth rate did not significantly improve at reduced volumes (20% and below) (Figure 2.7A). The size of the culture vessel (125-2800 ml), provided that the medium volume was not more than 40% of the vessel capacity, did not affect growth either, nor did the shape difference between the Erlenmeyer flasks (125- to 1000-ml capacity) and the Fernbach flask (2800-ml capacity) (Figure 2.8A). The speed of agitation applied to cultures also only marginally affected the growth rate (Figure 2.9A). Interestingly, the cultures that were not agitated at all grew as well as those that were given ample agitation (120-180 RPM), implying that even without additional shaking, gas exchange was not growth-limiting under photoheterotrophic conditions.

ICP-MS/MS analysis revealed that, compared to the reference conditions (40% filled in 250-ml flask, 180 RPM applied), Mn content was reduced when the fill-fraction of culture-to-flask volume was 20% or below (Figure 2.7F-H), and Cu content significantly increased in cells with no or minimal agitation (0-60 RPM) (Figure 2.9D). The three perturbations affecting aeration efficiency have no major impact on Ca, P, or S accumulation (Figure 2.7, Figure 2.8, Figure 2.9, Supplementary Figure 4B-D). Cellular S quantification was used for normalization.

The impact of aeration on algal growth and physiology has been a key research topic, particularly because primary production by algae has been recognized as a solution for carbon capture. In line with this focus, researchers often investigate the effects of substantial, intentional

changes in aeration modes (*e.g.* atmospheric vs. elevated levels of CO_2). Their studies have shown that variants in aeration can influence the cells' chemical composition, metabolic profile, as well as lipid and biomass production (164–168). In relation, my studies showed that subtle changes in aeration supply likewise affect oxygenation of the cultures and can have small but significant impacts on certain elemental quotas, like Cu and Mn. In particular, a less oxygenated Chlamydomonas culture, such as one that was not agitated, appeared to be more favorable for Cu uptake. One explanation could be that the culture was more reducing, and thereby increased the amount of Cu^{1+} in the medium, which is the form of Cu transported by CTR1 and CTR2, the two major Cu assimilation permeases in Chlamydomonas (80, 169). It is also worth noting that aeration can influence pH (170) and the cells' response to light and temperature (171, 172). Thus, it is critical to control the aeration parameters during experimentation, even when the consequences on elemental composition are minor.

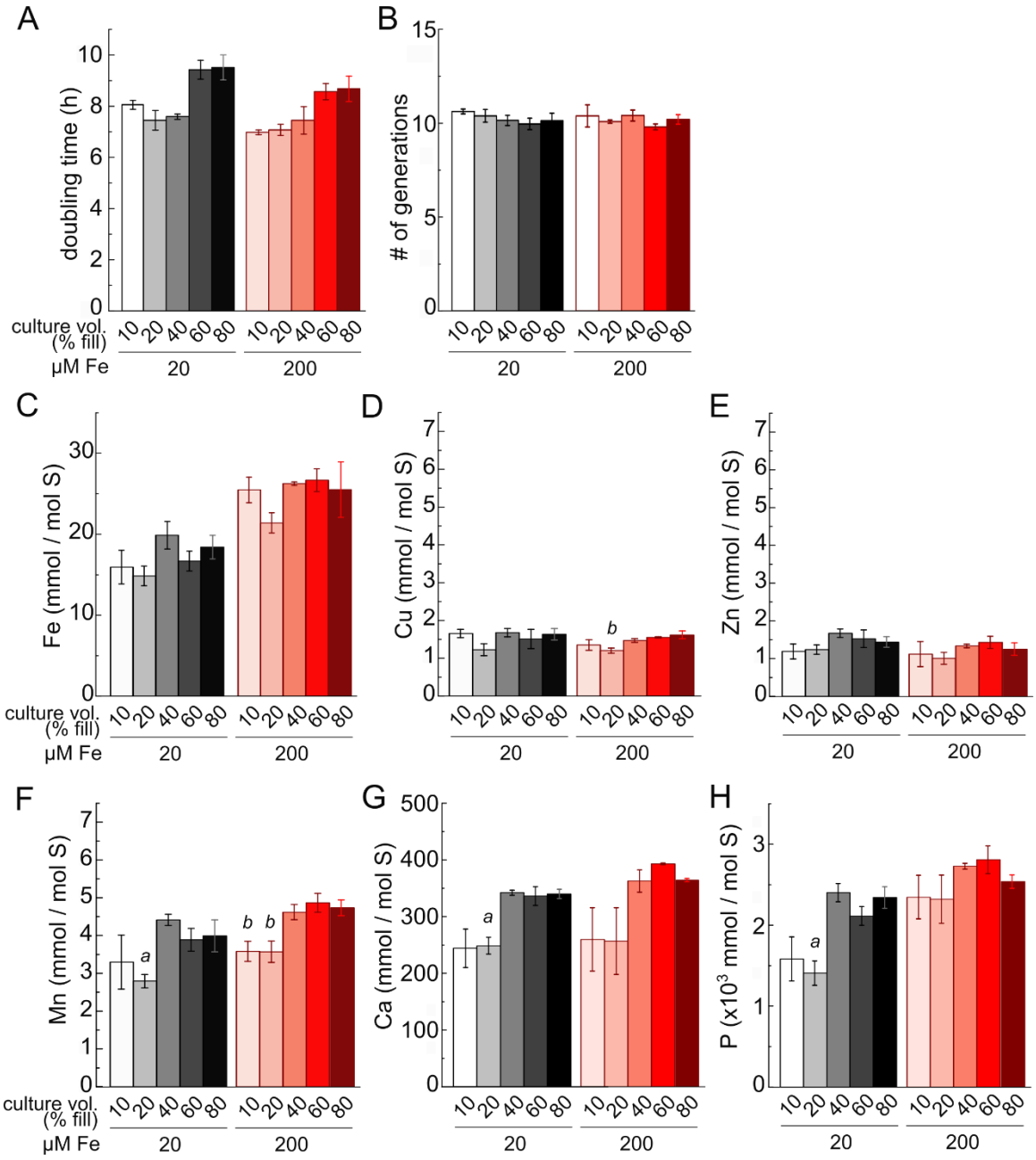

Figure 2.7. Fill-fraction of growth vessel has a small impact on cell growth and Mn content. (A) Doubling time and (B) number of generations until stationary phase of cells grown in replete (20 μM) or excess (200 μM) Fe condition with the indicated fill-fractions in growth vessels. (C-H) Cell-associated Fe (C), Cu (D), Zn (E), Mn (F), Ca (G) and P (H) content as measured by ICP-MS/MS, collected during mid-log growth (2-4 x 10^6 cells/ml). *a* and *b* indicate significant differences (t-test, $p \leq 0.013$, multiple Bonferroni-corrected) to cells grown in 20 μM Fe at 40% filled level (*a*) or 200 μM Fe at 40% filled level (*b*). Averages are shown with error bars indicating standard deviation of 3 independent cultures.

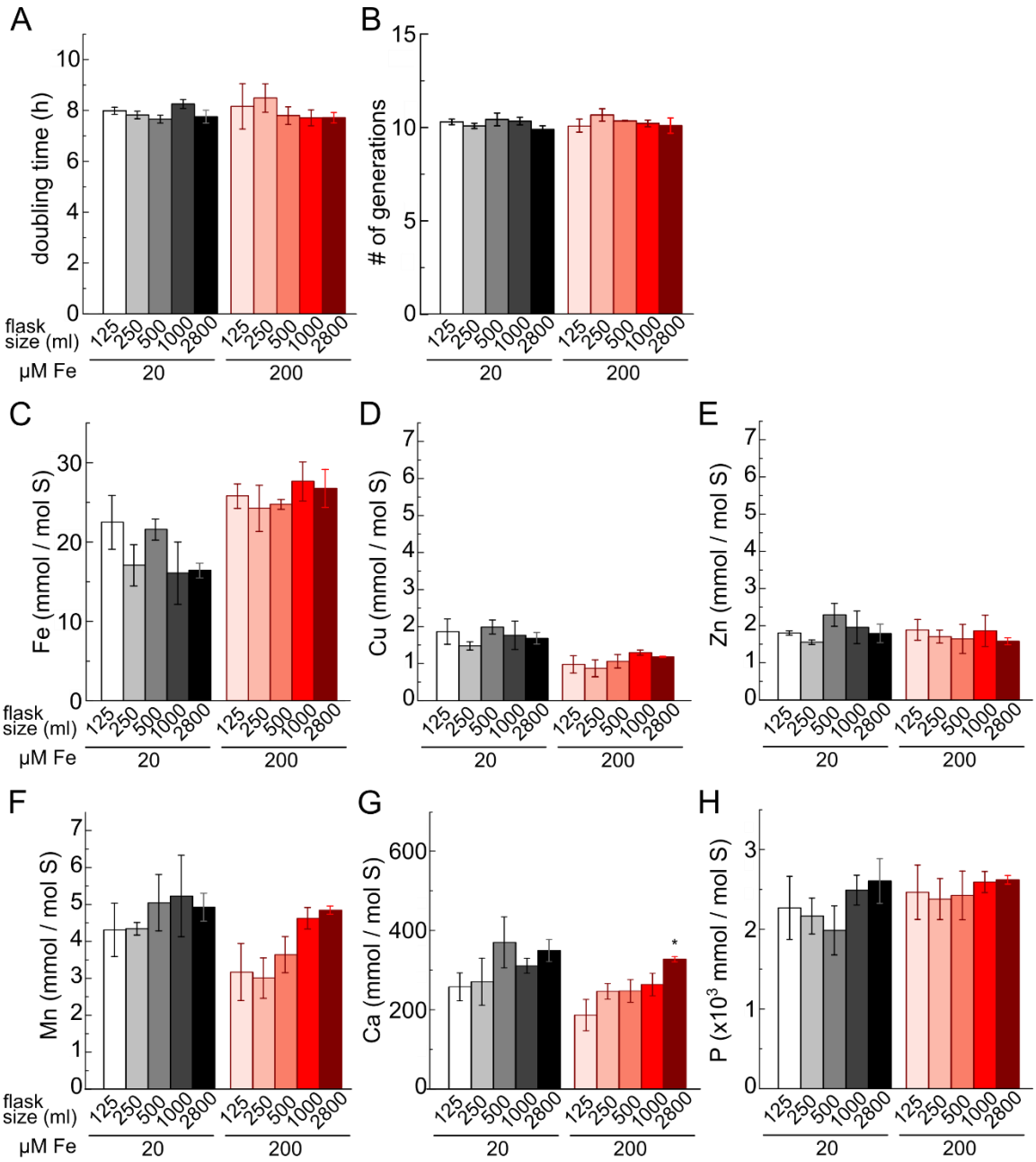

Figure 2.8. Size of the culture vessel does not impact growth or trace metal content. (A) Doubling time and (B) number of generations until stationary phase of cells grown in flasks of the indicated sizes in medium representing 40% of the flask capacity, with replete (20 μM) or excess (200 μM) medium Fe. (C-H) Cell-associated Fe (C), Cu (D), Zn (E), Mn (F), Ca (G) and P (H) content measured by ICP-MS/MS at mid-log growth (2-4 x 10^6 cells/ml). Asterisk indicates a significant difference (t-test, $p \leq 0.013$, multiple Bonferroni-corrected) to cells grown in the 250-ml flasks with 200 μM Fe; no significant difference by the same comparison and criterium was found within the 20 μM Fe dataset. Averages are shown with error bars indicating standard deviation of 3 independent cultures.

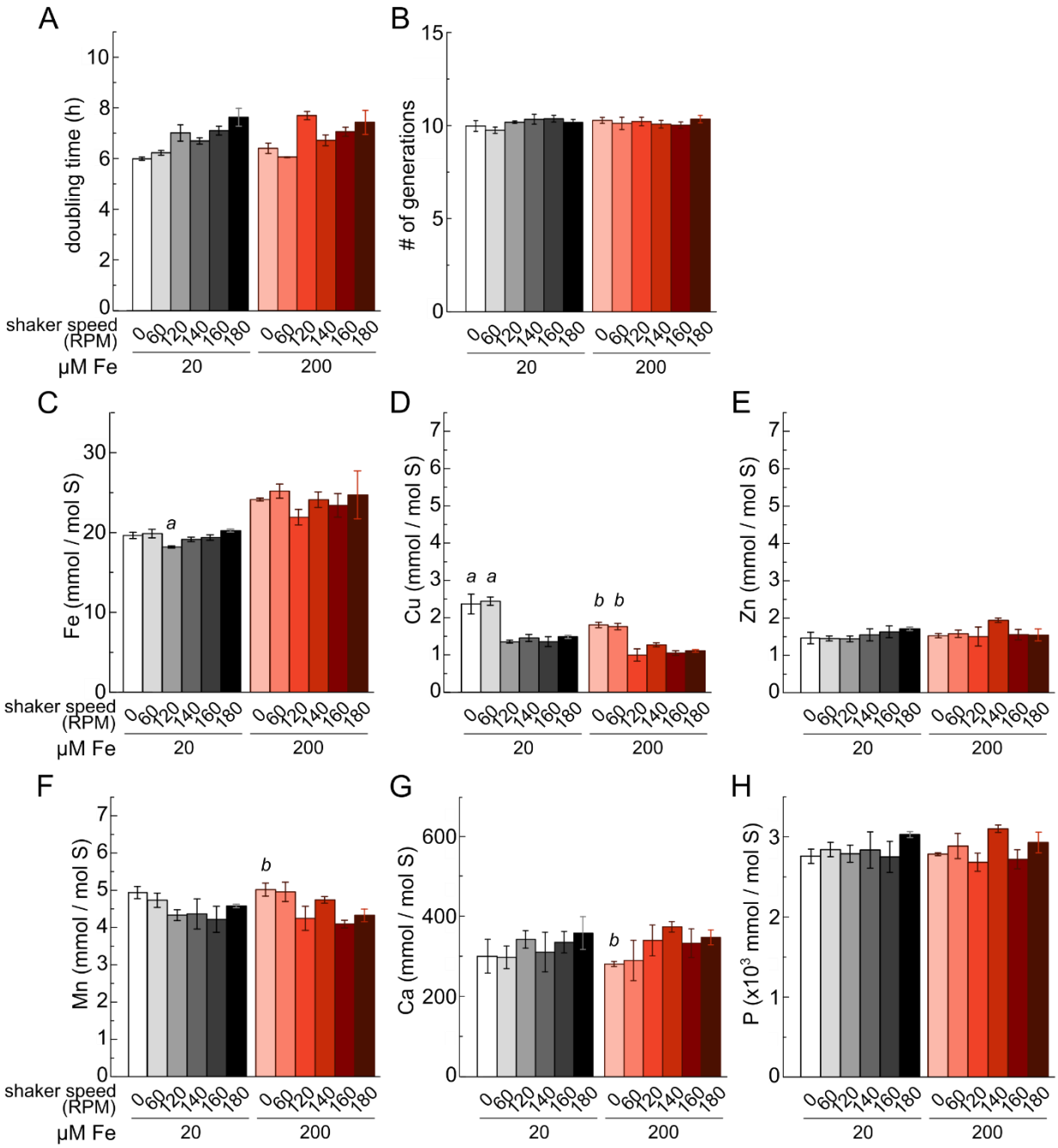

Figure 2.9. Culture agitation decreases the Cu quota. (A) Doubling time and (B) number of generations until stationary phase of cells grown at the indicated shaker speeds under replete or excess Fe condition (20 vs. 200 μM Fe). (C-H) Cell-associated Fe (C), Cu (D), Zn (E), Mn (F), Ca (G) and P (H) content as measured by ICP-MS/MS at mid-log growth (2-4 x 10^6 cells/ml). *a* and *b* indicate significant differences (t-test, $p \leq 0.01$, multiple Bonferroni-corrected) to cells grown in 20 μM Fe at 180 RPM (*a*) or 200 μM Fe at 180 RPM (*b*). Averages are shown with error bars indicating standard deviation of 3 independent cultures.

2.3.4 Temperature impacts growth rate and has subtle effects on trace metal content.

Most chemical reactions are temperature sensitive. Effects of moderate changes in cultivation temperature on Chlamydomonas growth and elemental composition were therefore analyzed. Growth assessment showed that decreasing the culturing temperature from the standard 24ºC to 21ºC or below substantially slowed cell growth, but the cells eventually acclimated to the colder conditions and were able to generate the same biomass (number of generations) as the reference cells grown at 24ºC (Figure 2.10). Between 24-30ºC, growth was virtually the same.

Temperature, unlike the other cultivation parameters discussed in this chapter, did affect cellular S content. ICP-MS/MS and TOC data revealed that as temperature increased, cellular S level decreased subtly while biomass was maintained in a relatively stable range (Figure 2.11). As such, the other elements from the ICP-MS/MS analysis in this experiment were normalized to cell number in addition to S content. Interestingly, as the culturing temperature increased, a trend of decreasing Fe, Cu, Zn, and Mn level per cell was observed, albeit the differences were not significant with respect to the reference cells (Figure 2.12A-D). A similar trend in Ca and P contents under replete Fe condition was noted as well (Figure 2.12E-F). When the same data were normalized to S, the Fe, Cu, Mn, Ca and P contents in fact correlated linearly with S level, whereas Zn level was significantly higher in cells grown at 18 and 21ºC vs. 24ºC (Supplementary Figure 5).

Temperature is known to strongly influence growth, cellular uptake of nutrients, and the chemical composition in algae (173–178). My data here described how growth and trace metal, Ca, and P contents are affected in Chlamydomonas when temperature changes between 18 and 30ºC. Chlamydomonas has been reported to grow optimally between 20-25ºC (179, 180). Consistently, my results showed that Chlamydomonas cells do grow markedly slower at 21ºC and below, but can in fact acclimate very well to temperatures from 24 up to 30ºC. Within the range from 18 to 30ºC, the increase in temperature appeared to slightly reduce cellular S content, which

might be associated with the parallel, subtle decrease in trace metal (Zn in particular), Ca, and P levels, given that S is pivotal to protein synthesis and metabolism in general (181). This change in the chemical composition of cells might be related to modifications in their synthesis and inventory of lipids and carbohydrates in response to temperature fluctuations. Studies have shown that in various algal species, including *C. reinhardtii*, increasing cultivation temperature leads to modulation in the fatty acid profile and lipid accumulation (175, 182–185). Effects of temperature on cells are also interconnected to light and nutrient supply, which likewise impacts cell physiology and in relation, the elemental profile (182, 184, 186). Therefore, temperature control is yet another crucial element for obtaining culture homogeneity during algal growth.

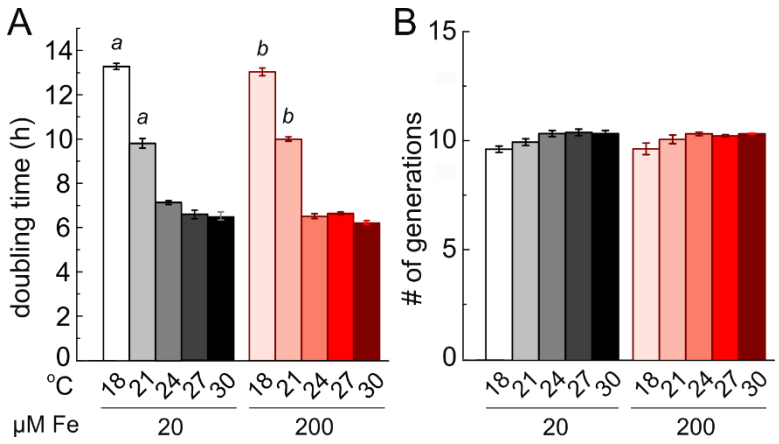

Figure 2.10. Temperature at 21ºC or below reduces cell growth rate. (A) Doubling time and (B) number of generations until stationary phase of cells grown at the indicated temperatures under replete (20 µM) or excess (200 µM) Fe condition. *a* and *b* indicate significant differences (t-test, $p \leq 0.013$, multiple Bonferroni-corrected) to cells grown at 24ºC with 20 µM Fe (*a*) or 200 µM Fe (*b*). Averages are shown with error bars indicating standard deviation of 3 independent cultures.

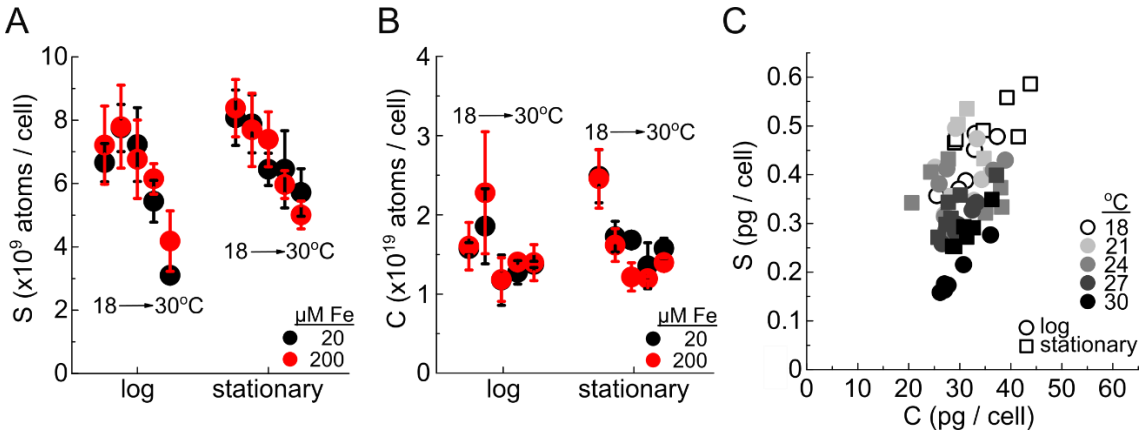

Figure 2.11. Increasing temperature subtly reduces cellular S content. (A) S content and (B) biomass of cells grown at 18, 21, 24, 27, and 30ºC at mid-log (2-4 x 10^6 cells/ml) and stationary phase (5 days post-inoculation, ~1 x 10^7 cells/ml) under replete (20 µM) and excess (200 µM) Fe conditions. S content was measured by ICP-MS/MS, while biomass was measured by TOC analyzer as non-purgeable organic carbon. No significant difference (t-test, $p \leq 0.013$, multiple Bonferroni-corrected) to cells grown at 24ºC was found in either the 20 or 200 µM Fe datasets. Averages are shown with error bars indicating standard deviation of 3 independent cultures. (C) Correlation of the S content and biomass presented in (A) and (B). All individual data points are shown.

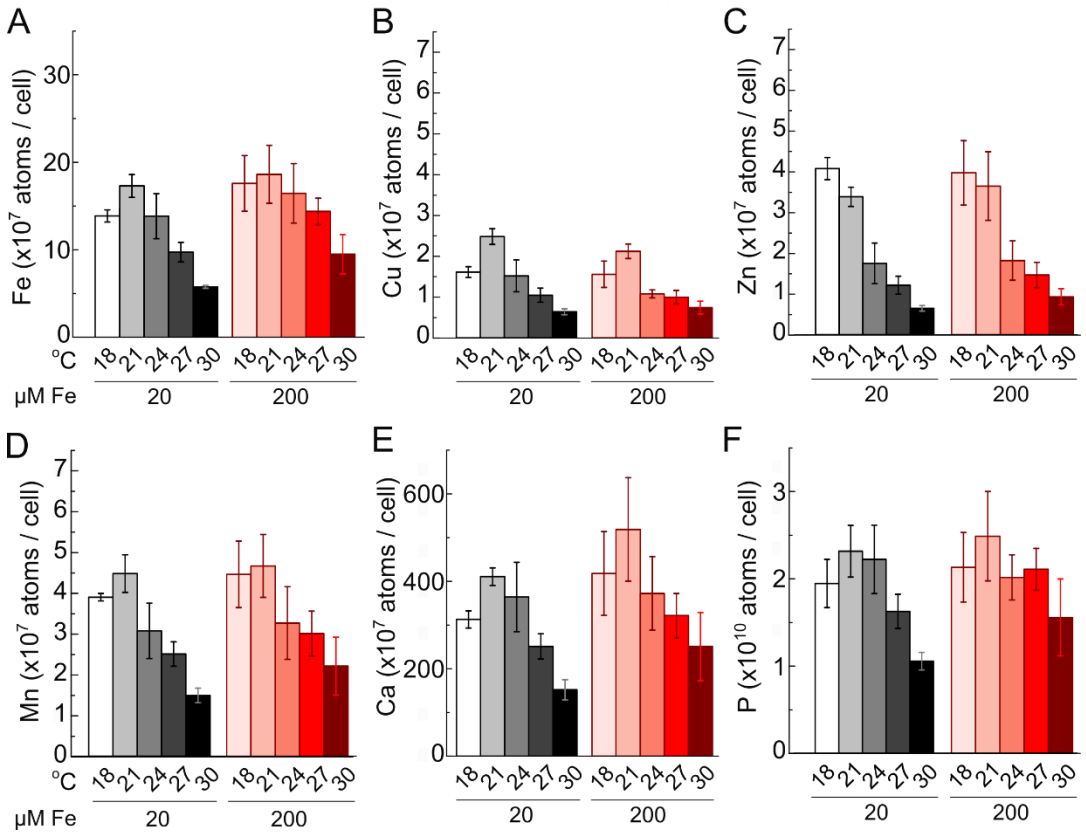

Figure 2.12. Temperature can affect cellular trace metal, Ca and P contents. Cell-associated Fe (A), Cu (B), Zn (C), Mn (D), Ca (E) and P (F) content at the indicated temperatures under replete (20 µM) and excess (200 µM) Fe conditions, as measured by ICP-MS/MS at mid-log growth (2-4 x 10^6 cells/ml), normalized per cell. No significant difference (t-test, $p \leq 0.013$, multiple Bonferroni-corrected) to cells grown at 24ºC was found in either the 20 or 200 µM Fe datasets. Averages are shown with error bars indicating standard deviation of 3 independent cultures.

2.3.5 Growth and cellular Fe content are similar among seven common laboratory wild-type strains with distinctive genetic backgrounds.

Chlamydomonas has been a subject of research for decades, and a complex network of interrelated strains has been developed during this time for many different works. The lineage of these strains is reported to trace back to a single isolation event, when Gilbert Smith isolated a zygospore from a soil sample collected in a potato field in Massachusetts in 1945 (20, 112). Although these are all “wild-type” strains, there are differences in their backgrounds. A recent survey of laboratory strains has revealed genetic diversity among 39 Chlamydomonas wild-type strains, all commonly used in laboratories (112). Almost all of the observed genetic diversity was attributable to two alternate haplotypes, which are proposed to be the remnants of an ancestral cross between parental strains with ~2% relative divergence. The presence of these haplotype regions can lead to variations in gene expression and phenotypes.

Therefore, I compared seven Chlamydomonas wild-type strains with respect to their growth and elemental composition under a photoheterotrophic condition provided with replete or excess Fe. These seven strains include: i) CC-4533, ii) CC-4532, iii) CC-124, iv) CC-125, v) CC-1690, vi) CC-1691, and vii) CC-1009. CC-4533 is the reference strain used in all experiments in this dissertation and the background strain of a collection of insertional mutants used in Aim 3 (17, 18). CC-4532 is a wild-type strain commonly used in trace metal studies in Chlamydomonas. Each of the other five strains is an exemplar representing a distinct Chlamydomonas lineage with a unique haplotype pattern (112).

All tested strains grew well at similar rates and produced the same number of generations, independent of medium Fe concentration (Figure 2.13). ICP-MS/MS data showed that at mid-log growth, the S content of strains was comparable (Supplementary Figure 6) and was thus used for normalization. Only a few slight but significant differences in the trace metal content were observed among CC-4533 vs. the others: CC-1690 and CC-1009 have reduced Fe and Zn, respectively, and CC-1691 has a higher Cu content than the other tested strains (Figure 2.14A-

D). While P levels in all strains were maintained in a similar range, CC-1690 and CC-1691 both have less Ca, ~60% of what the other strains accumulated (Figure 2.14E-F). The reduced Ca content led to the speculation that the levels of potassium (K) and magnesium (Mg), two other important cations in cells, might also be different. Indeed, CC-1690 has a significantly higher amount of K than CC-4533, but Mg contents were similar in all strains (Figure 2.14G-H).

The discovery that CC-1690 has a lower Ca but higher K content than the other wild-type strains is interesting. Perhaps in this strain, K is used for functions that are typically facilitated by Ca in the other strains. Yet, this complementary effect was not observed in CC-1691, which also accumulated significantly less Ca than the other strains, suggesting that the reduced content of Ca might be related to other unrecognized genetic and/or metabolic aspects.

Overall, the results from this experiment revealed that under photoheterotrophic condition supplied with replete nutrients, cellular growth and elemental composition among the seven tested common laboratory strains are largely comparable. However, others have found that this is not the case when cells are grown under various physiological stresses (119, 123, 187). For example, CC-1691 cannot remain green when grown in the dark while CC-1690 can, but CC-1691 grows better than CC-1690 under Fe limitation (112, 188). Therefore, one cannot assume that all wild-type strains would behave identically until they have been tested under the same culturing conditions.

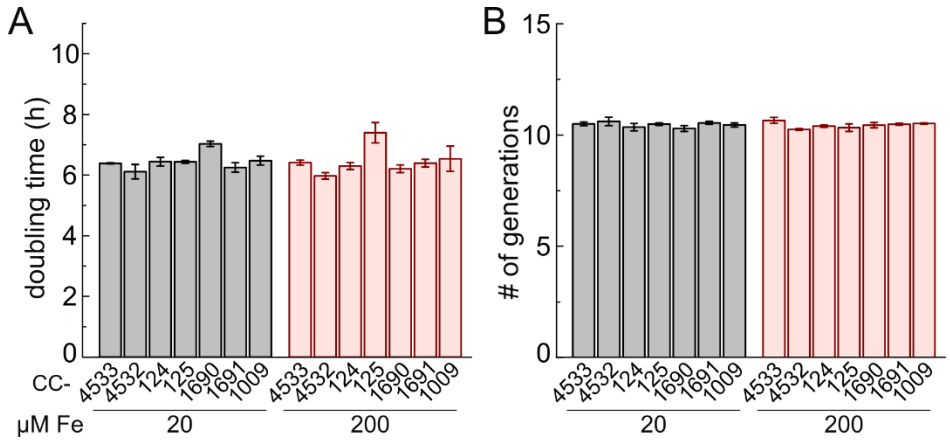

Figure 2.13. Growth among the 7 tested laboratory strains is very similar. (A) Doubling time and (B) number of generations until stationary phase of cells from the indicated Chlamydomonas strains grown in replete (20 µM) and excess (200 µM) Fe conditions. No significant difference (t-test, $p \leq 0.01$, multiple Bonferroni-corrected) was found comparing to CC-4533 under either 20 or 200 µM Fe condition. Averages are shown with error bars indicating standard deviation of 3 independent cultures.

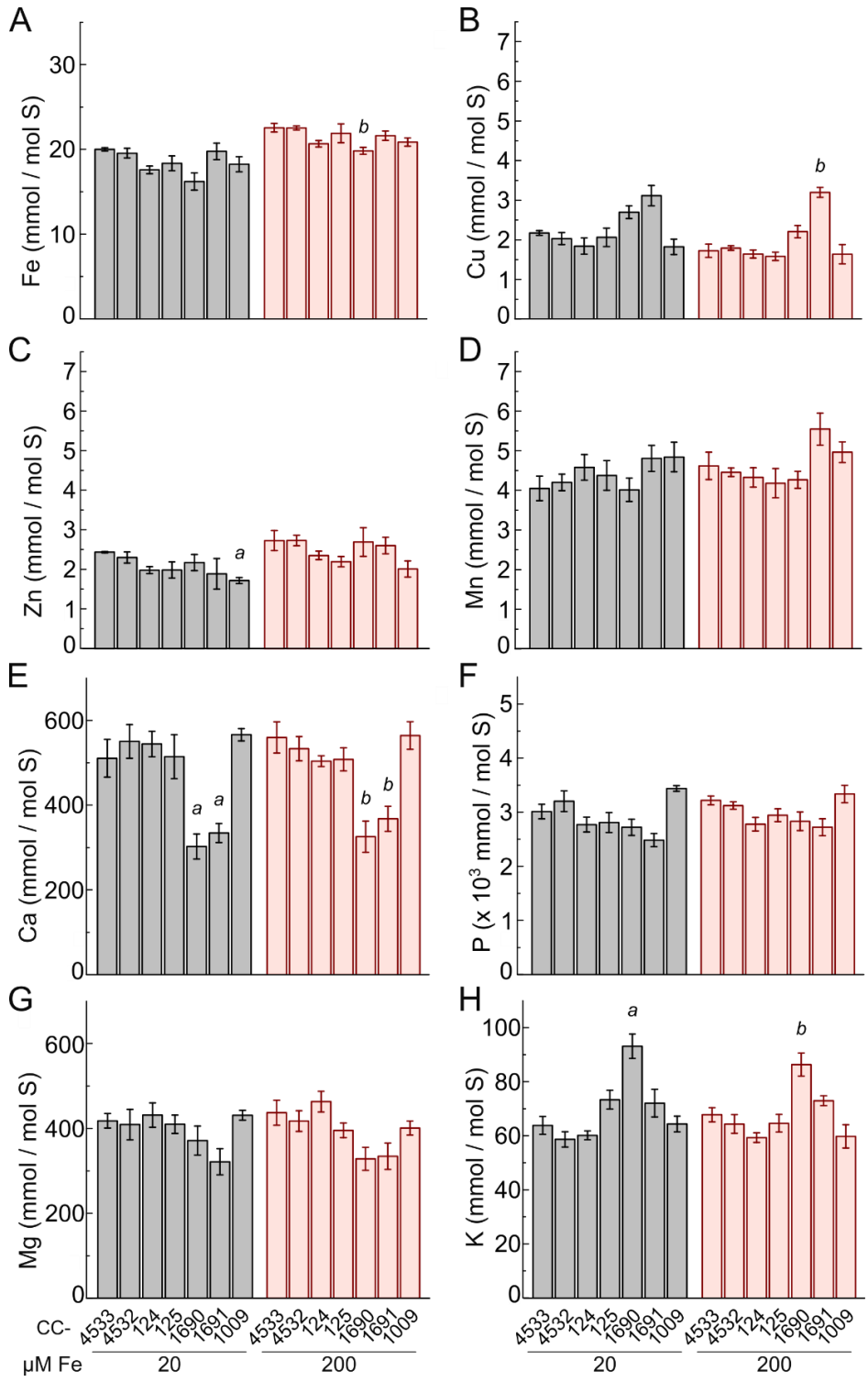

Figure 2.14. Trace metal, Ca, P, Mg, and K contents are largely comparable among the seven wild-type strains. (A-H) Cell-associated Fe (A), Cu (B), Zn (C), Mn (D), Ca (E), P (F), Mg (G), and K (H) contents from the indicated strains grown under replete or excess Fe condition (20 vs. 200 µM Fe), as measured by ICP-MS/MS at mid-log growth (2-4 x 106 cells/ml). *a* and *b* indicate significant differences (t-test, $p \leq 0.01$, multiple Bonferroni-corrected) to CC-4533 with 20 µM Fe (*a*) or 200 µM Fe (*b*). Averages are shown with error bars indicating standard deviation of 3 independent cultures.

2.3.6 Conclusions

Secondary cultivation variables must be tightly controlled during experimentation, in order to generate consistent and reproducible elemental composition data qualitatively and quantitatively, as demonstrated by the outcomes of this systematic analysis. A few key results can be summarized: 1) Chlamydomonas cells over-accumulate Fe during stationary phase linearly to time, and to a greater extent, under alkaline condition. In both situations, an excess Fe supply in the growth medium allows for greater cellular Fe assimilation. These experimental conditions that induce Fe accumulation were used in subsequent Aims for investigations into Fe storage and transport in Chlamydomonas; 2) Moderate alterations in the levels of photon flux density, aeration, and temperature do not significantly impact cellular Fe content, but can affect the quotas of other trace metals to various extent. Collectively, these results indicated that the accumulation of different nutrients in cells is specific in response to fluctuations in different environmental stimuli; and lastly, 3) Cell growth and elemental composition are generally comparable among common wild-type strains under photoheterotrophic, replete nutrient conditions, despite the differences in their genetic backgrounds.

CHAPTER 3

Distinguishing the Roles of Acidocalcisomes in Fe Storage

3.1 Background

When Fe is assimilated into cells, the metal ions are preferentially distributed to various sites of utilization, such as organellar targets in the chloroplasts or mitochondria, or secondarily, to sites of storage like ferritin or acidocalcisomes (6, 46, 80). In the former case, the Fe is used directly as a cofactor in proteins to support functions like electron transport and antioxidant defense. An example is the chloroplast ferredoxin protein family, which is crucial for photosynthesis and chloroplast metabolism. Ferredoxins are especially abundant. As a major Fe sink, they are central to many processes, including nitrogen assimilation and the transfer of electrons from photosystem (PS) I to NADPH, which is used in the Calvin cycle for CO_2 assimilation (189, 190). Another prominent example of an important chloroplast Fe protein is the Fe superoxide dismutase (FeSOD), which serves as a primary defense against oxidative stress (4). In Chlamydomonas, FeSOD is not only the dominant SOD under nutrient-replete condition (124), but its abundance and activity are also preferentially maintained under Fe deficiency over many other Fe proteins, including ferredoxins, thus highlighting its importance (191).

Once the demand of Fe for utilization in Fe protein biosynthesis is satisfied, any unused Fe in the cell is presumably stored to prevent unwanted ROS-induced damage. As introduced in Section 1.3.2, ferritin and the acidocalcisome are two candidate Fe storage or accumulation sites in Chlamydomonas. The major ferritin isoform in Chlamydomonas, FER1, is less abundant in the cells grown with excess Fe than in the cells that are Fe-deficient, although the Fe content of the FER1 complex is greater in the Fe-excess cells (36). Accordingly, ferritin in Chlamydomonas appears more likely to be an Fe buffer and/or a dynamic reservoir rather than a long-term Fe storage unit (33, 36, 38). Meanwhile, previous works have shown that acidocalcisomes sequester excess Fe and other metals in algae (61–63, 66, 192), but it is unclear if all excess Fe is un-

specifically localized to acidocalcisomes in Chlamydomonas. Thus, my second Aim was to test the hypothesis that acidocalcisomes are a default storage site for over-accumulated Fe in Chlamydomonas.

For this purpose, I turned to methodologies that enable high-resolution elemental imaging in organisms. Through these methods, the localization and distribution of Fe and other relevant elements in cells can be visualized. One such technique is nanoscale secondary ion mass spectrometry (NanoSIMS). NanoSIMS is a powerful surface elemental analysis technique that combines an ion microprobe with high spatial resolution (up to 50 nm) and analytical sensitivity (193, 194). The microprobe emits a focused, high-energy ion beam onto a sample surface, which "sputters" materials and generates secondary ions from the sample that are subsequently analyzed in a mass spectrometer. The analysis software then uses the data to create distribution maps of the target ion species. Five ion species may be simultaneously detected and relatively quantified. For my experiments, I accessed the NanoSIMS instrument at Lawrence Livermore National Laboratory (LLNL), which is specifically set up for addressing biological questions and subcellular elemental imaging (61, 62, 195). The NanoSIMS samples are also compatible for electron microscopy (EM), which is usually performed in addition to the NanoSIMS analysis to obtain correlative, high resolution structural information. However, sample preparation for NanoSIMS is time-consuming, involving chemical fixation or high-pressure freezing, embedding and then sectioning.

Another mass spectrometry-based technique for elemental imaging is laser ablation inductively coupled plasma mass spectrometry (LA-ICP-MS). Like NanoSIMS, LA-ICP-MS is a destructive imaging technique. It operates in principle similarly to NanoSIMS: A laser beam is focused onto a sample surface, which generates fine particles from the sample. The particles are then carried via a constant flow of Noble gases, typically argon and/or helium, into an ICP-MS instrument attached to the sample chamber, where the particles are ionized and analyzed based on their mass-to-charge ratio (196, 197). The diameter of the laser beam, *i.e.* the ablation "spot"

size, generally defines the spatial resolution of the resulting images. The presently available models typically offer spatial resolution up to 5 to 10 µm (196), which is about the size of a Chlamydomonas cell and is unfortunately insufficient for distinguishing subcellular elemental localization. The mass resolution power of LA-ICP-MS is also lower than that of NanoSIMS. Nevertheless, up to 70 different elements can be simultaneously detected and quantified by LA-ICP-MS, which is a distinctive strength of the technique (196).

X-ray fluorescence microscopy (XFM) has also gained recognition as a powerful, direct elemental analysis technique (198–200). It utilizes synchrotron-based X-rays to specifically eject the innermost (K-shell) electrons of target elements present in the sample. As a result, to stabilize the electronic structure of the elements, electrons in a higher orbital would transition back to the ground state to fill the void, releasing energy as fluorescence in the process. Because the energy transitions are highly element-specific (201), the distribution of target elements in the sample can be mapped based on detection of the corresponding fluorescence. Absolute elemental quantification is achievable with the use of standards. Unlike NanoSIMS, which analyzes a cross-section of the cell sample, XFM uses high energy X-rays (> 10 keV) that penetrates biological materials, enabling whole-cell analysis without the need for sectioning. The spatial resolution of XFM is comparable to that of NanoSIMS (< 100 nm), albeit with a lengthy analysis time (up to 3 h per Chlamydomonas cell). Together with the technique's strict requirement of synchrotron radiation, these drawbacks restrict the number of samples that can be analyzed per experiment, especially because the availability of the instrument, accessed through Argonne National Laboratory's (ANL's) Advance Photon Source, is very limited due to high demand.

In contrast to NanoSIMS and XFM, confocal fluorescence microscopy, combined with the use of element-specific chemical probes, is an indirect analysis technique. It relies on the detection of fluorescence from dyes that specifically target the substrates of interest (202, 203). Nonetheless, using proper probes and controls, both elemental and non-elemental features (*e.g.* pH) of whole cells may be visualized. For instance, acidic organelles like lysosomes and

acidocalcisomes have been visualized using the LysoSensor dye (62, 204). It is a commercially-available, pH-sensitive probe that accumulates in acidic environments (pH 4.4 - 5.5) as the result of protonation (pKa ~5.1), thereby emitting fluorescence. Some probes can also reveal information about the oxidation states of target elements. One example is the custom-made Fe probe, IP1. It has a highly selective turn-on response to Fe^{2+} over other cellular metal ions, as the oxidative dealkylation reaction that releases the fluorescent product in the dye requires Fe^{2+} binding (205). With confocal fluorescence microscopy, either fixed- or live-cell imaging is possible, allowing for steady state as well as dynamic studies. Also, sample preparation and the analysis procedure are much quicker and more straightforward than those for NanoSIMS and XFM. However, the results are only qualitative.

Based on the applicability of the techniques and the availability of the instruments, I used NanoSIMS, XFM, and confocal fluorescence microscopy to visualize the localization of intracellular Fe in wild-type cells grown under different luxury Fe conditions. I tested two sets of samples: 1) cells collected from log vs. stationary growth phase at neutral pH, and 2) cells grown in pH 7.0 vs. pH 8.5 medium collected during log growth phase. These conditions were selected based on work for Aim 1, which identified the culture conditions for Fe over-accumulation, *i.e.* stationary phase and alkaline pH (see Chapter 1 for details). Acidocalcisomes contain a high concentration of Ca and polyP, which can be visualized along with Fe by the above imaging techniques. Thus, if acidocalcisomes are a default storage site for excess Fe, then cells sampled from all Fe over-accumulating conditions should show more intense or a higher number of Fe/Ca/P colocalized foci compare to the reference cells not accumulating extra Fe. Collectively, the combination of the mentioned imaging techniques allowed me to analyze in detail the localization and distribution of excess Fe in Chlamydomonas under different Fe-over-accumulating conditions. The results also provide information regarding the internal biochemistry of the cells.

3.2 Methods and Materials

3.2.1 Strains and culture conditions

Chlamydomonas reinhardtii wild-type strain CC-4533 was cultured in TAP medium, exactly as described in Section 2.2.2. All growth variables were maintained the same except the following for the indicated comparisons. Cells in each culture were counted as described in Section 2.2.4 to assess density. For all experiments, samples were collected from two to three independent cultures grown in parallel.

1) Log vs. stationary growth:
    a. For NanoSIMS analysis: Cells were inoculated at 1 x 10^4 cells/ml into TAP at pH 7.0 containing either 20 or 200 µM Fe and were subsequently sampled at the four following timepoints: i) When culture density was 2-4 x 10^6 cells/ml (mid-log growth, occurred on day 3 post-inoculation), ii) When culture density initially reached 7-9 x 10^6 cells/ml (early stationary growth, occurred on day 4 post-inoculation), iii) 7 days post-inoculation (stationary growth, ~1 x 10^7 cells/ml), and iv) 10 days post-inoculation (late stationary growth, also ~1 x 10^7 cells/ml).
    b. For immunoblot analysis: Cells grown in TAP at pH 7.0 with 200 µM Fe were collected at the same timepoints as for NanoSIMS described in (a) and one additional time on day 14 post-inoculation (prolonged stationary growth, ~1 x 10^7 cells/ml).
    c. For XFM analysis: Only mid-log (2-4 x 10^6 cells/ml) and stationary cells (7-day post-inoculation) grown with 200 µM Fe in TAP at pH 7.0 were collected for XFM analysis (*i.e.* time points (i) and (iii) described in (a)).
2) Alkaline vs. neutral pH: Cells were inoculated into TAP with 200 µM Fe at either pH 7.0 or pH 8.5 (media were titrated as described in Section 2.2.2). Samples were collected from both sets of cultures during mid-log growth (2-4 x 10^6 cells/ml) for NanoSIMS, XFM, and confocal fluorescence microscopy analyses.

3.2.2 Sample preparation for NanoSIMS and EM

Cells collected for NanoSIMS and EM analyses may be chemically fixed or high-pressure frozen prior to embedding into resin and sectioning. Chemical fixation is a well-established, conventional method that has been applied to Chlamydomonas cells in many studies (61, 62, 206, 207). In comparison, high-pressure freezing followed by freeze-substitution is a newer technique, but since its development, it has been considered a gold standard for optimal structural preservation (208). High-pressure freezing has also been tested on Chlamydomonas cells and produced excellent ultrastructure images (209, 210).

Recently, questions were raised about whether the fixing and dehydration process during chemical fixation might perturb the *in vivo* localization of mobile elements (*e.g.* metal ions). Previous work (211) has shown very similar cell morphology and chemical distribution in cereal samples that were chemically fixed vs. high-pressure frozen. I performed a similar comparison of the two preparation methods using Chlamydomonas cells grown under two conditions: i) transitioning from Fe limitation to Fe excess, and ii) in Zn deficiency. These conditions were selected because the resulting cellular physiology and chemical composition have been determined from previous studies (61, 63), and therefore provided context for sample quality assessment. The culture conditions are described below. Unless specified, the TAP media were prepared and all other growth variables were set as described in Section 2.2.2. All nutrient-deficient media were prepared in acid-washed flasks and graduated cylinders (*i.e.* 6N HCl treatment overnight, and then rinsed seven times with Milli-Q water before use). The acid-washing step was performed to minimize trace metal contamination from the vessels.

1) Transition from Fe starvation to Fe-excess: Replete-grown, mid-log cells were inoculated into TAP medium (pH 7.0) with 0.1 µM Fe at 1 x 10^4 cells/ml. When the culture ceased growth (stationary phase ~1 x 10^6 cells/ml), 200 µM of Fe was added to the medium. Cells were collected for EM and NanoSIMS analyses 24 h after the addition of Fe.

2) Zn deficiency: Replete-grown, mid-log cells were inoculated into Zn-free TAP medium (pH 7.0) with 10 µM (excess) Cu-EDTA (25) at 1 x 10^5 cells/ml. Cells were collected for EM analyses at stationary phase (~1 x 10^6 cells/ml).

Briefly, EM and NanoSIMS results indicated that in the cells grown in condition (i), chemical fixation and high-pressure freezing preserved morphology and elemental distribution to a similar extent, although the high-pressure frozen cells generally produced higher ion counts during NanoSIMS imaging (Supplementary Figure 7A, Supplementary Figure 8). In contrast, the cells grown in condition (ii) appeared unable to withstand high-pressure freezing and abnormal morphology was observed (Supplementary Figure 7B). Since chemical fixation did not appear to redistribute elements of interest in cells, and because the success of high-pressure freezing varied, chemical fixation was used for all other NanoSIMS and EM experiments reported throughout this dissertation. The methods for both chemical fixation and high-pressure freezing are described below, each followed by the same resin infiltration and embedding procedures.

Chemical fixation: At the times of sample collection as specified in the preceding sections, 1 x 10^7 cells were collected from each culture by centrifugation at 2,600 x*g* for 1 min. The cell pellets were washed once with 1 mM Na_2-EDTA and twice with 10 mM sodium phosphate (pH 7.0), and immersed in a solution containing 2% glutaraldehyde, 2% paraformaldehyde in 10 mM sodium phosphate (pH 7.0) overnight at 4ºC. The fixed samples were brought to UC Berkeley Electron Microscopy Laboratory (UCB-EML) (Berkeley, CA), where they were rinsed three times, 10 min each, with 0.1 M sodium cacodylate (pH 7.2) and post-fixed in 1% OsO_4 in 0.1 M sodium cacodylate (pH 7.2) at room temperature for 1 h. After rinsing again with sodium cacodylate, samples were dehydrated in an acetone gradient (35, 50, 70, 80, 95, 100, 100, 100%) for 10 min each, followed by resin infiltration.

High-pressure freezing and freeze-substitution: When samples were ready for collection, the culture volume needed for 1 x 10^7 cells of each sample was measured into conical tubes and immediately brought to UCB-EML. The cells were then concentrated into a pellet by centrifugation at 700 x*g* for 2 min, washed once with 1 mM Na_2-EDTA and twice with 10 mM sodium phosphate (pH 7.0). Most of the supernatant was removed and the cells were left in a paste-like mixture. The cells were transferred to high-pressure freezing planchettes between 50- and 200-µm deep (Wohlwend Engineering) and frozen in a Bal-Tec HPM-010 high-pressure freezer (Bal-Tec AG). The frozen cells were transferred to cryovials containing 1.5 ml of acetone with 1% OsO_4 and 0.1% uranyl acetate, stored in liquid nitrogen (LN_2) for 1-4 days. The freeze-substitution process was performed as described in (212, 213). Briefly, the cryovials were transferred from the LN_2 dewar and placed horizontally inside a LN_2-cooled metal block with 13-mm holes (-195ºC), placed within an insulated container filled with LN_2. The block/container was placed on an orbital shaker operating at 120 RPM. The cells warmed to ~20ºC after 3 h and were removed from the planchettes. They were then rinsed three times with pure acetone and infiltrated with resin.

Resin infiltration, embedding, and sectioning: Samples were infiltrated in a mixture of pure acetone and Epon-Araldite resin in the following sequence: i) 30 min in 2:1 mixture of acetone : resin, ii) 30 min in 1:1 mixture, iii) 30 min in 1:2 mixture, iv) 30 min in resin (no acetone), v) 1 h in resin, vi) 1-2 h in resin. The samples were then embedded in fresh resin and cured at 60ºC for 48 h. Sections of 200-nm thickness were cut on an ultramicrotome (Leica EM UC6) at LLNL (Livermore, CA) using a diamond knife and deposited on 200-mesh carbon- and Formvar-coated copper grids. Sections were post-stained with 1% uranyl acetate for 4 min and lead citrate for 2 min.

3.2.3 NanoSIMS and EM

Sectioned cells were analyzed in the CAMECA NanoSIMS 50 (Gennevilliers, France) at LLNL to image the intracellular distribution of Fe, Ca, and P as described in (62). Briefly, a focused negative oxygen ion primary beam was scanned over the sample to generate secondary ions. The secondary ion mass spectrometer was tuned for ~3,500 mass resolving power, and $^{12}C^+$, $^{31}P^+$, $^{40}Ca^+$, and $^{56}Fe^+$ were detected simultaneously by electron multipliers in pulse counting mode. The correct metal ion peaks were identified using NBS610 glass (National Institute of Standards and Technology, USA). The analysis areas were pre-sputtered at high current (~1.2 nA O^-) to establish sputtering equilibrium, then scanned at a moderate spatial resolution (~400 nm; 100 pA O^-, 40 x 40 μm^2 raster, 256 x 256 pixels, 1 ms/pixel, 30 cycles) or at a higher spatial resolution (~150 nm; 30 pA O^-, 15 x 15 μm^2 raster, 256 x 256 pixels, 1 ms/pixel, 25 cycles) to collect serial secondary ion images. The samples were imaged on a transmission electron microscope (FEI Tecnai TEM at UCB-EML) and/or a scanning electron microscope (FEI Inspect F FEG-SEM at LLNL) either before or after the NanoSIMS analyses to obtain the correlated images of cell structures.

The NanoSIMS data were quantitatively processed using custom software (L'Image, L.R. Nittler, Carnegie Institution for Science, Washington, D.C.). The raw ion images were corrected for detector dead time (44 s) before being used to produce the final images. Regions of interest (ROIs) were defined using an automated algorithm that subdivided the analyzed area into particles. Particles that were not on cells were manually deleted. Ion ratios ($^{31}P/^{12}C$, $^{40}Ca/^{12}C$, and $^{56}Fe/^{12}C$) for each ROI were calculated by averaging the ratios over replicate scans, which gave relative quantitative composition. Because the NanoSIMS data were not standardized by a matching standard, concentrations could not be deduced.

3.2.4 XFM

XFM experiments were performed as described in (63). Briefly, 3 x 10^6 cells were collected from cultures at the times specified in Section 3.2.1 by quick centrifugation (16,000 x*g* for 15 s). The cell pellets were washed twice in 1X PBS and fixed in 4% paraformaldehyde in 1X PBS at room temperature for 10 min. Then, 100 µl of the fixed cell suspension, thoroughly mixed, was pipetted onto a poly-L-lysine-coated silicon nitride membrane window (5 x 5 x 0.2 mm frame, 2 x 2 x 0.0005 mm Si_3N_4 membrane, Silson) and allowed to settle for 30 min. Residual supernatant on the windows was removed by gentle suction and the windows were subsequently washed twice with 1X PBS, once with 0.1 M ammonium acetate, and once with Milli-Q water. The windows were air dried and stored at room temperature. The samples were transported to the Bionanoprobe at ANL's Advance Photon Source (Lemont, IL) (214). The analyses were performed at either beamline 21-ID-D or 9-ID-B, where the Bionanoprobe was located at each time of visit. The incident X-ray energy was tuned to 10 keV to target direct excitation of atomic K transitions of elements up to z = 30 (Zn). Two coarse scans were performed to identify the coordination of cells on the windows, followed by a high-resolution scan for each cell (~70 nm spatial resolution). Data were fitted and analyzed using the MAPS software package (215).

3.2.5 Confocal fluorescence microscopy

From each culture, 4 x 10^6 cells were collected at the targeted time (see Section 3.2.1) by centrifugation at 2,600 x*g* for 1 min. The cell pellets were washed twice with 10 mM sodium phosphate (pH 7.0), and then resuspended in 50 µl of the diluted fluorescent dyes. All dyes were diluted in 10 mM sodium phosphate (pH 7.0), with LysoSensor DND189 (Thermo Fisher Scientific) to a final concentration of 2 M, and IP1 ((205), custom made by H. Nelson, UCLA, Los Angeles, CA) to a final concentration of 200 µM. Cells were then mounted on glass slides for visualization. Confocal microscopy was performed as described in (62). Briefly, images were captured on a Zeiss LSCM Airyscan 880 equipped with a X63/1.4 oil immersion objective in channel mode.

Exposure time, fluorescent emission signals from the dyes and chlorophyll, and other imaging controls were adjusted via the Zeiss ZEN Black software. Between 2 and 12 cells were imaged for each sample.

3.2.6 Immunodetection of Chlamydomonas proteins

At the times of sample collection as indicated in Section 3.2.1, ~2 x 10^7 cells were collected by centrifugation at 1,500 x*g* for 3 min at 4ºC and washed twice with 10 mM sodium phosphate (pH 7.0). Proteins were released from the cells by three slow freeze-thaw cycles (-80ºC to -20ºC to room temperature, (216)). Protein concentrations were determined with Pierce BCA assay against BSA as standard (Thermo Fisher Scientific). The proteins were separated by SDS-PAGE (15 µg of proteins per lane plus 50%, 25%, and 12.5% serial dilutions), then transferred to 0.45 µM nitrocellulose membranes by semi-dry electroblotting. The membranes were blocked in 3% non-fat dried milk in 1X PBS with 0.1% (w/v) Tween 20 for 1 h at room temperature, then incubated with primary antibodies in fresh aliquots of the above dried milk/PBS solution at 4ºC overnight. Primary antibodies were used at the following dilutions: FDX1 (189) and FER1 (36) at 1:1,000; FeSOD (191) at 1:2,000; V-PPase (L. Davidi, K. Holbrook, & D. Strenkert, unpublished, UCLA, Los Angeles, CA) at 1:15,000; OEE1 (T. Yeates, UCLA, Los Angeles, CA) at 1:4,000; and CF_1 (217) at 1:100,000.

On the following day, membranes were washed three times with 1X PBS with 0.1% (w/v) Tween 20, then incubated with an alkaline phosphatase-conjugated goat anti-rabbit IgG secondary antibody (Southern Biotechnology Associates) for 1 h at room temperature, diluted at 1:10,000 in 3% non-fat dried milk in 1X PBS with 0.1% (w/v) Tween 20. Bound antibodies were detected according to the manufacturer's instructions.

3.3 Results and Discussion

3.3.1 Most Fe accumulated during stationary phase does not colocalize with Ca and P, and is likely stored in sites other than the acidocalcisome.

To examine how the localization of intracellular Fe changes during cell growth, cells collected during log phase (3 days post-inoculation) and at progressing times during stationary phase (collected 4-, 7-, and 10-days post-inoculation) were analyzed by NanoSIMS imaging. The images revealed an increasing count of $^{56}Fe^{+}$, $^{40}Ca^{+}$, and $^{31}P^{+}$ ions in cells as they grew from log into stationary phase under both replete and excess Fe conditions (20 and 200 μM Fe in growth medium) (Figure 3.1, Figure 3.2). The ion counts can be used as a proxy for relative elemental quantification. As such, this result is consistent with the ICP-MS/MS data reported in Chapter 1, which showed that cells accumulated Fe, Ca, and P in stationary phase (Figure 2.2C,G,H). Significantly, the NanoSIMS images showed a gradually increasing number of Fe foci as cells progressed from log to late stationary phase, most prominently between stationary and late stationary phases (collected on day 7 and 10 post-inoculation, respectively). This indicated that the excess Fe was sequestered into a specific site rather than evenly distributed within the cell.

To distinguish whether this Fe accumulation site might be the acidocalcisome, I compared the location and the ion quantity of the Fe foci to those of Ca and P. The comparison was accomplished qualitatively, by overlaying the distribution of $^{56}Fe^{+}$, $^{40}Ca^{+}$, and $^{31}P^{+}$ (Figure 3.1A, Figure 3.2A), and quantitatively, by subdividing each cell into non-overlapping regions of interest (ROIs) and correlating ion counts of $^{56}Fe^{+}$, $^{40}Ca^{+}$, and $^{31}P^{+}$, normalized to $^{12}C^{+}$, in each ROI (Figure 3.1B-D, Figure 3.2B-D). The ROIs were defined based on $^{12}C^{+}$ distribution using automated algorithms in the NanoSIMS analysis software (Supplementary Figure 9A-B). Analyses by both methods showed that most Fe, especially in the cells collected before late stationary phase, did not colocalize with Ca and P. Visually, colocalized areas of Fe (shown in green), Ca (red), and P (blue) would be seen in white on the overlaid images. Such white spots, however, were not evident

in cells under replete Fe condition (Figure 3.1A), and were observed in only ~25% of the clear Fe foci (foci with $^{56}Fe^{+}$ count >12) in the late stationary-gown cells under excess Fe condition (Figure 3.2A). Likewise, relative quantification of $^{56}Fe^{+}$ using ROIs that covered all cell areas in the images correlated weakly, albeit positively, with that of $^{31}P^{+}$ (Figure 3.1B, Figure 3.2B) and $^{40}Ca^{+}$ (Figure 3.1C, Figure 3.2C). In the late stationary-phase cells in which Fe counts were the highest among the analyzed samples, the R^2 value between $^{56}Fe^{+}/^{12}C^{+}$ and $^{31}P^{+}/^{12}C^{+}$ was 0.35 in replete Fe condition and 0.53 in excess Fe condition; and between $^{56}Fe^{+}/^{12}C^{+}$ and $^{40}Ca^{+}/^{12}C^{+}$, R^2 = 0.14 in replete Fe and 0.15 in excess Fe condition. The R^2 values for the same sets of correlation in all other samples were lower. Quantification using only ROIs with a high Fe count ($^{56}Fe^{+}$ count >12) reduced background noise but did not improve correlations between Fe and Ca or P (Supplementary Figure 10). This outcome suggested that most of the Fe that cells accumulated during stationary phase, at least up to 10 days post-inoculation, was unlikely to be localized to a site with high Ca and P, *e.g.* the acidocalcisome. However, there might be colocalization for a small fraction of Fe with P and Ca in late stationary-phase cells, when excess Fe was provided in the medium.

Separately, the relationship between $^{40}Ca^{+}$ and $^{31}P^{+}$ in the cells was also evaluated to approximate the relative abundance of acidocalcisomes, regardless of the presence of Fe within. By the same correlative quantification described above, data showed a weak positive correlation between $^{40}Ca^{+}/^{12}C^{+}$ and $^{31}P^{+}/^{12}C^{+}$ in the log-grown cells (R^2 = 0.16 and 0.25 under replete and excess Fe conditions, respectively). In all the samples collected from the different stationary phases, the correlations between $^{40}Ca^{+}/^{12}C^{+}$ and $^{31}P^{+}/^{12}C^{+}$ were more positive, with R^2 values between 0.45 and 0.57 (Figure 3.1D, Figure 3.2D). This result suggested that cells in stationary phase might contain more acidocalcisomes than those at log phase, as reported by Goodenough et al. (130). Note, however, that 100% correlation between Ca and P is never expected, since P was also present in various metabolites and as polyP in cells outside of the acidocalcisome.

To complement the NanoSIMS analysis, log and stationary cells (collected 3- and 7-days post inoculation, respectively) grown with excess Fe were also imaged by XFM at single-cell, subcellular resolution. The XFM images revealed Fe diffused within the log-grown cells, whereas in the stationary cells, Fe foci were clearly observed, but the foci did not colocalize with Ca or P (Figure 3.3). The observation of these Fe foci suggested that the Fe acquired by cells during stationary phase was sequestered into a specific site without much Ca or P, as also indicated by the NanoSIMS data. Nevertheless, Ca- and P-colocalized foci were detected in the peripheral region of some of the stationary cells imaged by XFM, suggesting that acidocalcisomes were formed. These acidocalcisomes might have an alternative function than to store excess Fe, such as balancing ion gradients in the cells. The acidocalcisome might also play a role in nutrient sensing. Studies have shown that Chlamydomonas mutant strains that are defective in polyP accumulation are unable to acclimate normally to sulfur or nitrogen deprivation (218–220).

Both the NanoSIMS and XFM data suggested that excess Fe accumulated during stationary phase in Chlamydomonas was sequestered into a specific site that has little Ca and P, hinting that the Fe was unlikely to be stored in the acidocalcisome. Thus, alternatively, the Fe could be bound to other Fe proteins or small molecule ligands in the cell. Following up on this thought, I probed the abundance of several essential Fe proteins, including the major isoform of ferritin (FER1), ferredoxin, a product of the *PETF* gene (FDX1), and Fe superoxide dismutase (FeSOD), by immunodetection in cells grown with excess Fe collected from log and stationary growth phases (collected on day 3, 4, 7, 10, 14 post-inoculation). The abundance of the vacuolar H^+-pyrophosphatase (V-PPase) typically present in the boundary membrane of acidocalcisomes was also assessed. Results showed that the abundances of FDX1 and FeSOD were unchanged in cells throughout the time course, while the abundance of FER1 was constant from log to stationary phase (day 3 to 7 post-inoculation) but was reduced by ~50% by late stationary phase (day 10 post-inoculation) (Figure 3.4). The abundance of V-PPase appeared slightly diminished

when cells transitioned from log to early stationary phase, but was increased again in cells in late stationary phase.

The lack of change in the abundance of FDX1 and FeSOD suggested that the excess Fe was not being used to facilitate additional synthesis of Fe proteins (*e.g.* to enhance metabolism). As such, the Fe was more likely kept in storage sites, potentially in ferritin, even though the abundance of FER1 decreased as cells transitioned from log to late stationary phase. Nevertheless, the abundance of FER1 is not necessarily linked in parallel to the Fe content of the protein complex (36). In Fe-starved Chlamydomonas cells, FER1 is increased in abundance but reduced in its Fe content compared to Fe-replete cells. Therefore, although the abundance of FER1 was reduced in cells in late stationary phase, each FER1 complex might be holding a greater quantity of Fe atoms. Work on measuring the Fe content of FER1 in log- vs. different stationary-phase cells is presently ongoing; the results could help determine more accurately whether ferritin plays a role in Fe sequestration during stationary growth.

The NanoSIMS and XFM results suggesting an increased presence of acidocalcisomes in stationary- vs. log-grown cells were not surprising. Consistent with my data, Goodenough et al. (130) have shown, using quick-freeze deep-etch electron microscopy, that replete, stationary Chlamydomonas cells (collected 7-days post-inoculation) produced abundant polyP granule-containing acidocalcisomes, which were not evident in log-grown cells. However, it is unclear whether the acidocalcisomes in these stationary cells were intended for sequestering trace elements and/or other molecules beside polyP. In the studies where metals were well distinguished within acidocalcisomes (*i.e.* strong colocalization between the metals, Ca, and P by NanoSIMS and/or XFM), the cells were subjected to nutritional stresses that led to extreme metal overload ($\geq$ 10-fold increase compared to standard conditions) (61–63). Thus, it is possible that during standard stationary growth, when the otherwise healthy cells accumulated only a moderate excess of Fe (< 5-fold compared to log-grown cells), acidocalcisomes were formed only to store polyP, whereas the surplus Fe was kept elsewhere.

Another interesting note is that log-grown Chlamydomonas cells in fact contain acidocalcisomes, but these acidocalcisomes generally lack polyP granules, as pointed out in (130) based on comparison of ultrastructures. These acidocalcisomes are not electron-dense, making them difficult to be identified by TEM. It is also challenging to detect them by NanoSIMS and XFM, since both techniques rely on visualizing strong colocalization of Ca and P as a marker of the organelle. Hence, NanoSIMS and XFM imaging might only be effective for detecting polyP-abundant acidocalcisomes, such as those in stationary-phase cells. In log-grown cells, the abundance of acidocalcisomes per se, neglecting their content, might actually be comparable to that in stationary-phase cells. In relation, the subtle fluctuation in the abundance of V-PPase from log to stationary phase is intriguing. Assuming that the abundance of V-PPase is proportional to the abundance of acidocalcisomes in the cell, this trend would imply degradation, followed by re-synthesis of a small fraction of acidocalcisomes as cells transitioned from log to early stationary to late stationary phase.

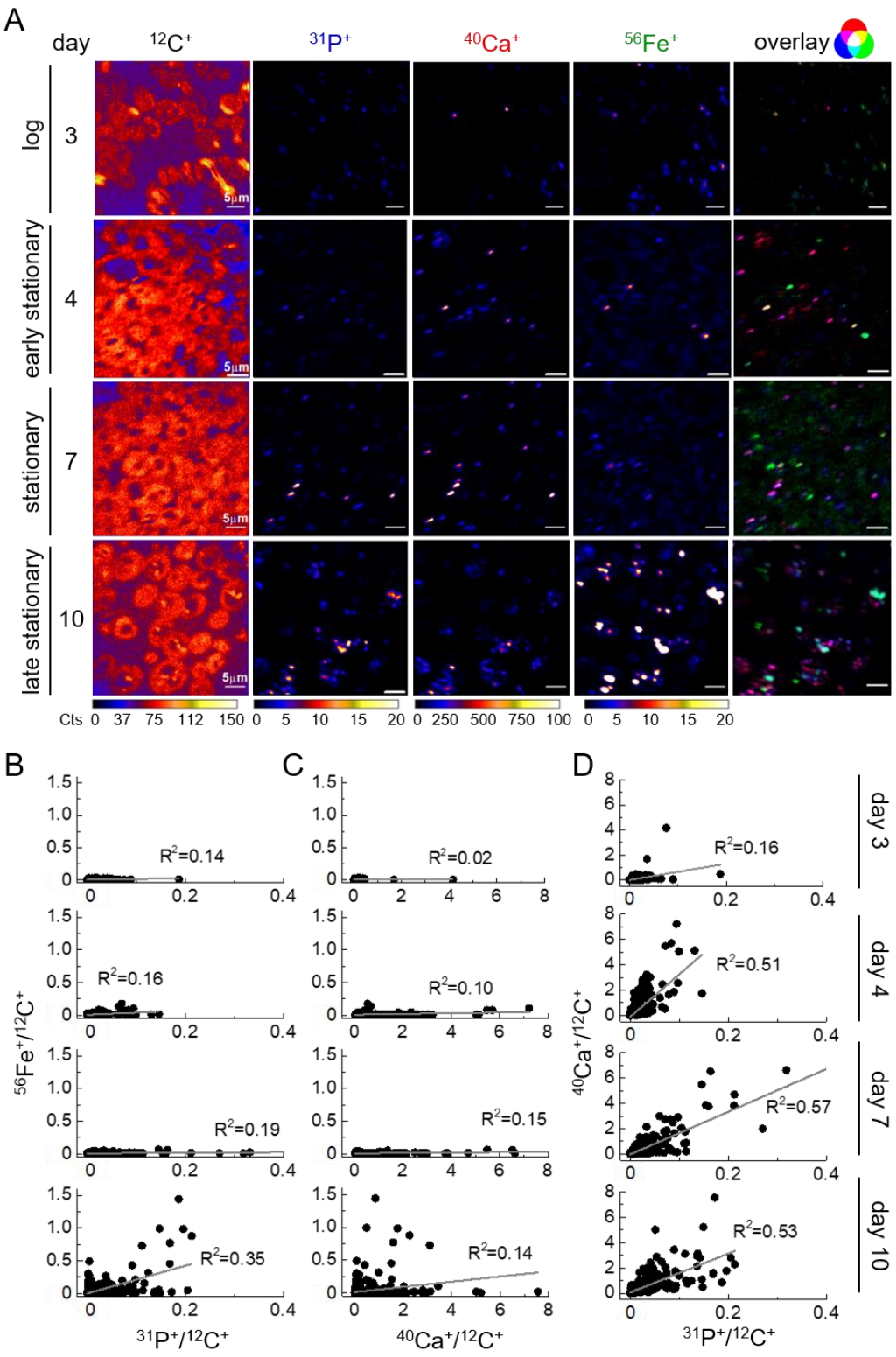

Figure 3.1. Fe foci in cells increase in number from log to stationary phase in replete Fe condition, but are only loosely correlated with Ca and P. (A) NanoSIMS images of cells grown in TAP medium with 20 μM Fe (pH 7.0), collected during log and various stationary phases on the indicated day post-inoculation,

and the corresponding overlaid RGB images of the $^{31}P^+$ (blue), $^{40}Ca^+$ (red), and $^{56}Fe^+$ (green) images. Sections of fixed cells were imaged in positive secondary ion mode. Scale bar, 5 µm. (B, C, D) Subcellular correlative quantification of $^{12}C^+$-normalized $^{56}Fe^+$ with $^{31}P^+$ (B) and $^{40}Ca^+$ (C), and of $^{40}Ca^+$ with $^{31}P^+$ (D), from the NanoSIMS imaged cells shown in (A) and one other replicate. Each point in the plots corresponds to a non-overlapping ROI generated by an automated algorithm in the analysis software (see Supplementary Figure 9A). R^2 values correspond to linear regression fitting of the data points.

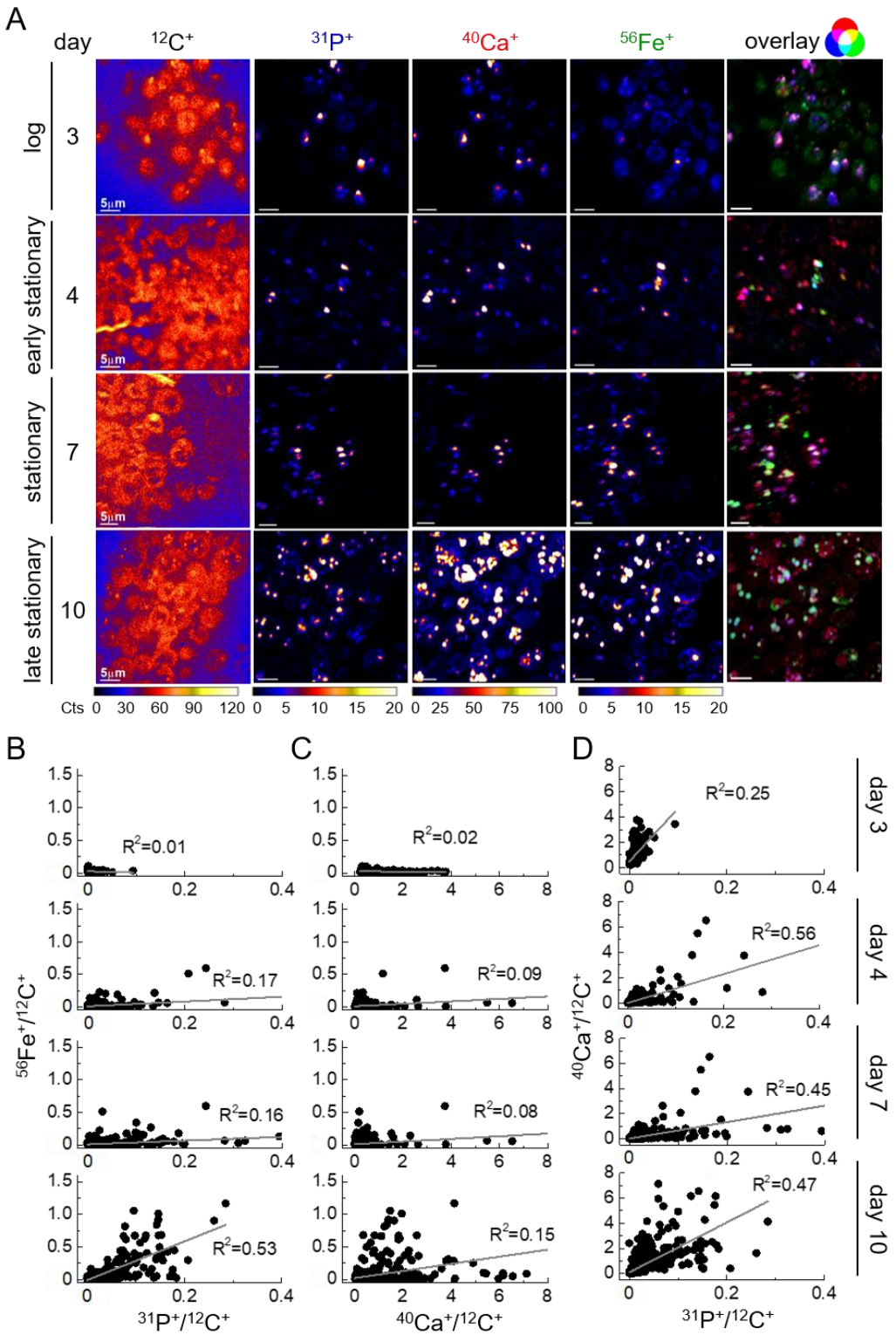

Figure 3.2. Cells supplied with excess Fe form more Fe foci as they grew from log to stationary phase, but the foci mostly correlate weakly with Ca and P. (A) NanoSIMS images of cells grown in TAP medium with 200 μM Fe (pH 7.0), collected during log and various stationary phases on the indicated day post-inoculation, and the corresponding overlaid RGB images of the $^{31}P^+$ (blue), $^{40}Ca^+$ (red), and $^{56}Fe^+$

(green) images. Sections of fixed cells were imaged in positive secondary ion mode. Scale bar, 5 μm. (B, C, D) Subcellular correlative quantification of $^{12}C^+$-normalized $^{56}Fe^+$ with $^{31}P^+$ (B) and $^{40}Ca^+$ (C), and of $^{40}Ca^+$ with $^{31}P^+$ (D), from the NanoSIMS imaged cells shown in (A) and one other replicate. Each point in the plots corresponds to a non-overlapping ROI generated by an automated algorithm in the analysis software (see Supplementary Figure 9B). R^2 values correspond to linear regression fitting of the data points.

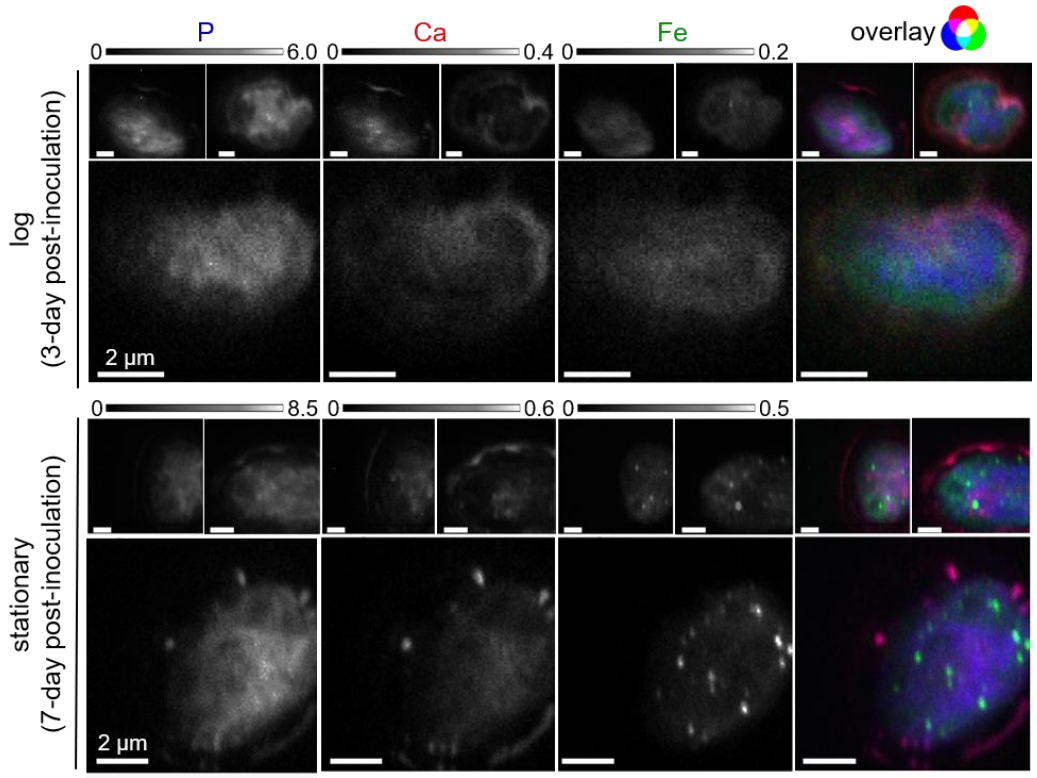

Figure 3.3. Fe foci in stationary-phase cells are separated from Ca- and P-colocalized foci. XFM images of P, Ca, and Fe distribution in three individual cells, grown in TAP medium with 200 μM Fe (pH 7.0), collected during log and stationary phase on the indicated day post-inoculation, and the corresponding overlaid RGB images of the three elements ($^{31}P^+$, blue; $^{40}Ca^+$, red; $^{56}Fe^+$, green). The elemental distributions are depicted between the minimal (black) and maximal (white) elemental concentrations in μg/cm^2, labeled above the images. Scale bar, 2 μm.

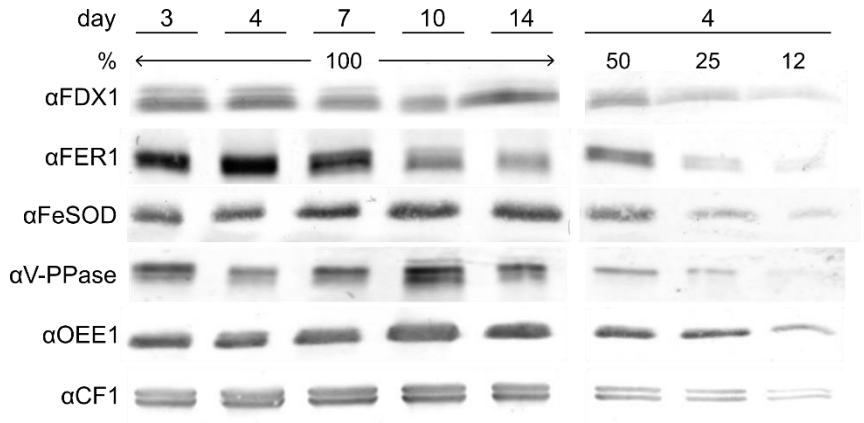

Figure 3.4. The abundance of ferritin1 decreases in cells in late stationary phase. Cells grown in TAP medium with 200 μM Fe (pH 7.0) were collected on the indicated day post-inoculation for immunoblot analysis. Total protein samples (15 μg per lane plus dilution series) were separated by denaturing SDS-PAGE, followed by immune-detection with antibodies raised against the indicated proteins; OEE1 and CF1 were used as loading controls. The immune-detection for each protein was performed 2-3 times on independent samples.

3.3.2 Alkaline pH-grown cells contain strong Fe/Ca/P-colocalized foci, acidic vacuoles, and a Fe^{2+} pool, suggesting the acidocalcisome as the Fe accumulation site.

Cells grown at alkaline pH (pH 8.5) accumulated 10-fold or more Fe than did cells grown at neutral pH (pH 7.0), especially when excess Fe was provided (Figure 2.5A). NanoSIMS and XFM were again exploited to visualize the localization and distribution of intracellular Fe in these conditions. To start, NanoSIMS was used to image a raster with 15-18 cells from each condition. The cells subjected to alkaline pH showed much stronger $^{56}Fe^+$ signals compared to those grown at neutral pH, with a 13x-difference in ion counts between the regions with the highest Fe signal from each sample (Figure 3.5A-C). In the alkaline pH sample, most of the Fe was found in foci and colocalized with P and Ca (Figure 3.5A), whereas in the neutral pH sample, Fe was predominantly evenly distributed throughout the cells, with 1-2 hotspots and limited colocalization with P and Ca noted in a few cells (Figure 3.5C). Relative quantification using ROIs covering all cell areas (Supplementary Figure 9C-D) revealed a strong positive correlation between $^{56}Fe^+/^{12}C^+$ and $^{31}P^+/^{12}C^+$ as well as $^{56}Fe^+/^{12}C^+$ and $^{40}Ca^+/^{12}C^+$ in the alkaline pH sample (R^2 = 0.90 and 0.88, respectively), which was not observed in the neutral pH sample (R^2 = 0.08 and 0.13 for $^{56}Fe^+/^{12}C^+$ vs. $^{31}P^+/^{12}C^+$ and $^{56}Fe^+/^{12}C^+$ vs. $^{40}Ca^+/^{12}C^+$, respectively) (Figure 3.6A-B).

To better visualize the subcellular localization of the Fe foci in alkaline pH-grown cells, individual cells were imaged by NanoSIMS as well as by XFM at a higher spatial resolution. TEM used in parallel with NanoSIMS indicated the Fe/Ca/P foci locating toward the cell periphery or in the periplasmic space (Figure 3.5B). Likewise, XFM also revealed strong colocalization of Fe, Ca, and P in distinct foci in alkaline pH-grown cells, with the foci locating mostly within or adjacent to the periplasm of the cells (Figure 3.7). No hotspot where Fe, Ca, and P colocalized was evident in cells grown at neutral pH by XFM. Altogether, both the NanoSIMS and XFM data suggest that most of the excess Fe taken by alkaline pH-grown cells was sequestered to a site containing Ca and P, likely the acidocalcisome.

As mentioned in the previous section, correlation between $^{40}Ca^{+}$ and $^{31}P^{+}$ from the NanoSIMS analysis may be used to estimate the relative abundance of polyP-containing acidocalcisomes in cells. From the analysis, relative quantification showed a strong positive correlation between $^{31}P^{+}/^{12}C^{+}$ and $^{40}Ca^{+}/^{12}C^{+}$ in the alkaline pH sample (R^2 = 0.80), while this correlation in the neutral pH sample was weaker (R^2 = 0.49) (Figure 3.6C). This result suggested a higher number of Ca- and P-overlapping foci (*e.g.* acidocalcisomes) in cells grown under alkaline pH than those under neutral pH.

To further complement the NanoSIMS and XFM data, confocal fluorescent microscopy was used to image alkaline and neutral pH-grown cells stained with the LysoSensor DND189 dye, which releases fluorescence in acidic compartments. Consistent with the elemental distribution images, the LysoSensor probe detected a substantially higher number of acidic bodies in the cells sampled from the alkaline pH culture than the cells from the neutral pH culture (Figure 3.8).

Beside LysoSensor, alkaline and neutral pH-grown cells were also imaged by confocal fluorescent microscopy using the IP1 dye, a synthetic Fe^{2+} probe (205), because spectroscopic data have suggested acidic vacuoles as the likely compartments for storing Fe^{2+} in Chlamydomonas (221). The microscopy images showed Fe^{2+} foci in the alkaline pH-grown cells, locating mostly around or near the peripheral region, whereas none was detected in the cells grown at neutral pH (Figure 3.9). This result, in line with the NanoSIMS and XFM data, suggested that Fe was indeed sequestered in foci around the cell periphery in cells grown in alkaline condition. However, the distribution of Fe^{3+} is unknown, for IP1 chelates Fe^{2+} specifically. Studies have shown that while ferritin in plants has a ferroxidase domain and binds Fe^{3+} exclusively (29, 222), vacuoles in algae, plants, and yeasts can store both Fe^{2+} and Fe^{3+} (221, 223, 224). Chlamydomonas cells contain transporters of both Fe^{2+} and Fe^{3+}, although two candidate vacuolar Fe importers, CVL1 and CVL2, are hypothesized to bind Fe^{2+} (46). A follow-up confocal fluorescence microscopy experiment is to image the cells with IP1 and LysoSensor and/or DAPI concurrently, which allows visualizing colocalization between Fe^{2+} and acidic compartments

and/or polyP (225), respectively. The result could help determine whether the Fe^{2+} foci are within acidocalcisomes.

Interestingly, while acidic bodies, detected by LysoSensor, were distributed throughout the cells grown in alkaline condition, the Fe/Ca/P-colocalized foci observed in the NanoSIMS and XFM images were mostly evident around the peripheral space of the cells. Likewise, the Fe^{2+} foci detected through IP1-staining were mainly noted in the peripheral region. This location of the Fe foci might be an indication that the excess Fe was to be expelled by the cells to prevent toxicity, as opposed to storage for future use. Studies have found heavy metals in the polyP granules of yeast, fungi, algae, and bacteria, and have linked polyP degradation and phosphate efflux to detoxification of the heavy metals (226–228). Also, Goodenough et al. showed autophagy-related, polyP granules-containing vacuoles in Chlamydomonas cells under stressed conditions (130). To more conclusively determine whether the excess Fe in alkaline pH-grown cells is stored or trashed, a time course experiment monitoring the cells and the localization of the Fe would be necessary.

Meanwhile, exposure to external high pH likely disrupts the balance of intracellular pH. As a result, the formation of acidic bodies throughout the alkaline pH-grown cells might be a way to restore proton gradients across the plasma membrane, in addition to housing overloaded Fe. In yeast, the vacuolar H^+-ATPase (V-ATPase) is a crucial component for maintaining cytosolic pH homeostasis (152, 229), which is required for generating a well-balanced proton gradient to enable smooth uptake of various nutrients (230, 231). Furthermore, it has been shown that a higher extracellular pH stabilizes V-ATPase complexes, making them less susceptible to dissociation and increasing their activity (152, 232). Mutants lacking structural or assembling components of the V-ATPase were found to be extremely sensitive to even moderate alkalinization of the growth medium (152, 230, 233). It is possible that functional acidic vacuoles or components on the vacuole play a similar role in alkaline pH tolerance in Chlamydomonas. This might be another reason for cells to accumulate acidic vacuoles in an alkaline environment.

Collectively, all the experimental results are consistent and suggested that the acidocalcisome was likely an accumulation site for excess Fe when cells are grown under alkaline pH. This outcome clearly contrasts with the outcome from the experiments with stationary cells (Section 3.3.1), in which the excess Fe was mostly found not associated with Ca and P. There are two major differences between the two sets of cells: 1) the fitness of the cells, and 2) the extent of Fe over-accumulation. The alkaline pH-grown cells (collected during log phase) were physiologically stressed, as evident by their slow growth (Figure 2.4B), and they accumulated 10-fold more Fe compared to the reference cells (neutral pH-, log-grown cells). In comparison, the stationary-phase cells (grown at neutral pH) exhibited no unhealthy phenotypes but accumulated only 3 to 4-fold more Fe compared to the reference cells. By these distinctions, one explanation for the different outcomes of Fe storage is that the acidocalcisome may be an Fe accumulation site only when cells are under physiological stress, and/or when the intracellular Fe content exceeds a certain capacity, perhaps that of ferritin. This hypothesis would also be consistent with the results from previous studies, where a high amount of Cu, Fe, and Mn were detected in acidocalcisomes in stressed Chlamydomonas cells that heavily overload with metals (61–63). However, it is unclear from the imaging data how bioavailable and accessible is the Fe kept within the acidocalcisome vs. other Fe proteins (*e.g.* ferritin). This is discussed in Chapter 4.

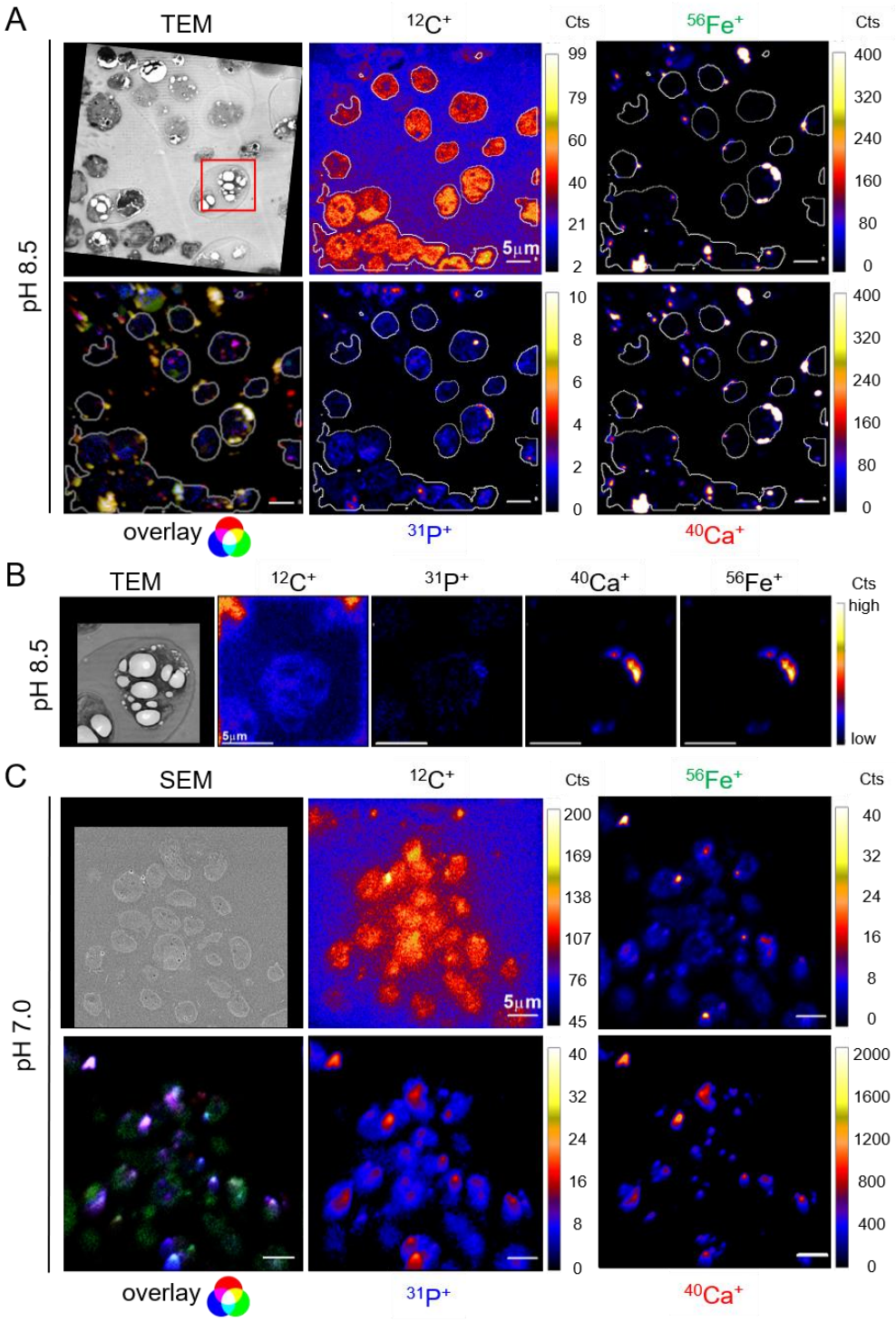

Figure 3.5. Fe accumulated in cells under alkaline pH growth colocalizes with Ca and P. (A, C) Correlated EM (top left) and NanoSIMS images (top & bottom in center & right) of cells grown in pH 8.5 (A) and pH 7.0 (C) TAP medium with 200 µM Fe, and the overlaid RGB images of $^{31}P^{+}$ (blue), $^{40}Ca^{+}$ (red), and $^{56}Fe^{+}$ (green) (bottom left). The red box on the EM image in (A) indicates the analyzed area shown in (B). White lines outline the cell areas that contain the ROIs used for the correlative quantification in Figure 3.6. (B) Correlated TEM and NanoSIMS images of a cell from the section shown in (A). Sections of fixed cells were imaged in positive secondary ion mode. Scale bar, 5 µm.

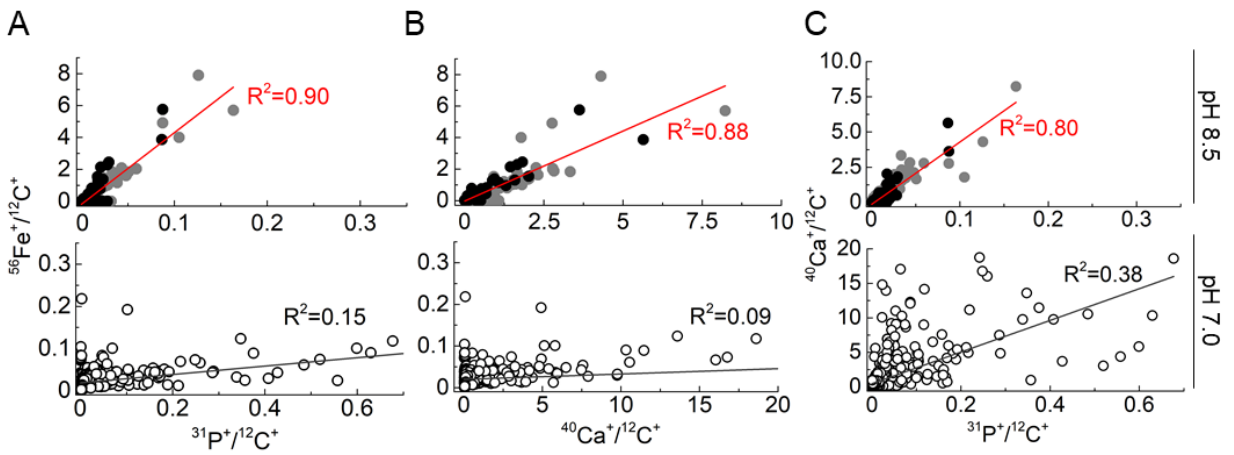

Figure 3.6. Subcellular relative quantification by NanoSIMS shows strong positive correlations between Fe, Ca, and P in cells grown at alkaline pH. (A, B, C) Correlative quantification of $^{12}C^+$-normalized $^{56}Fe^+$ with $^{31}P^+$ (A) and $^{40}Ca^+$ (B), and $^{40}Ca^+$ with $^{31}P^+$ (C), from NanoSIMS imaged cells grown in pH 8.5 (top) vs. pH 7.0 (bottom) TAP medium with 200 µM Fe (three replicates each). Each point in the plots corresponds to a non-overlapping ROI generated by an automated algorithm in the analysis software (see Supplementary Figure 9C). Black points in the pH 8.5 correlation plots represent quantifications from the images shown in Figure 3.5, while gray points represent data from two other replicates. R^2 values correspond to linear regression fitting of all data points in each plot.

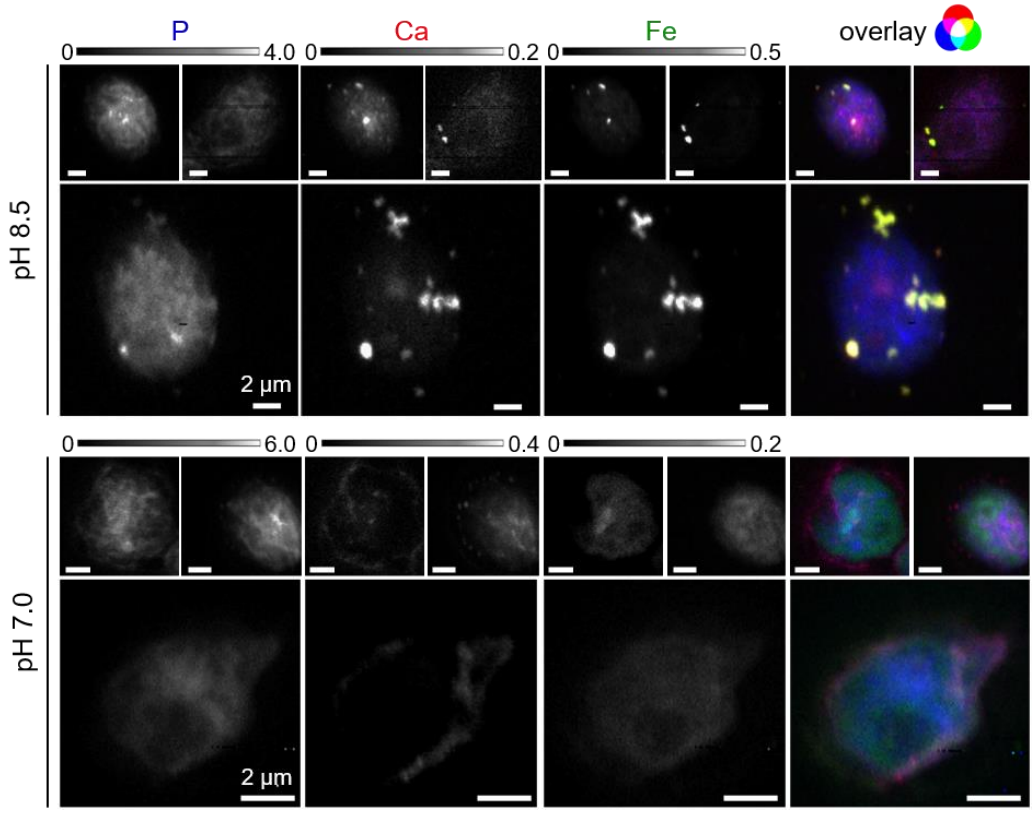

Figure 3.7. Fe, Ca, and P colocalize in foci in the peripheral region of alkaline pH-grown cells. XFM images of P, Ca, and Fe distribution in three individual cells grown in pH 8.5 or pH 7.0 TAP medium with 200 µM Fe. On the rightmost are the corresponding overlaid RGB images of the three elements ($^{31}P^{+}$, blue; $^{40}Ca^{+}$, red; $^{56}Fe^{+}$, green). The elemental distributions are depicted between the minimal (black) and maximal (white) elemental concentrations in µg/cm^2, labeled above the images. Scale bar, 2 µm.

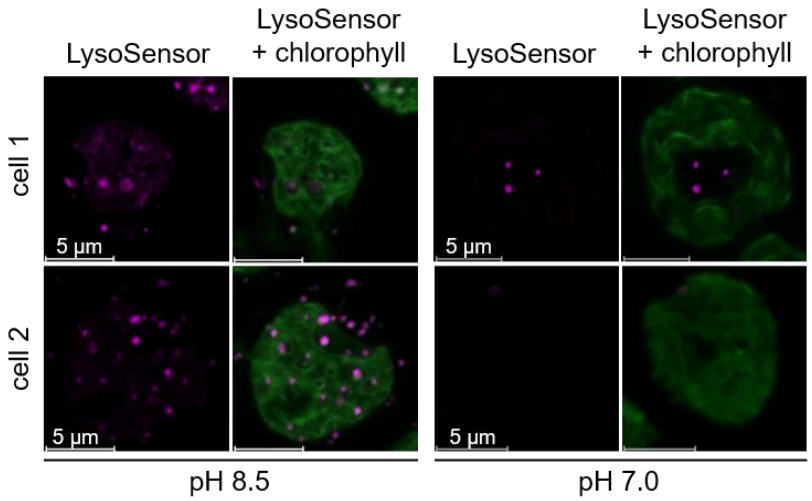

Figure 3.8. Cells grown at alkaline pH contain more acidic bodies than those at neutral pH. Low pH compartments (shown in purple) in cells grown in pH 8.5 or pH 7.0 TAP medium with 200 µM Fe were detected by LysoSensor DND-189. Chlorophyll autofluorescence is shown in green in the overlaid images with LysoSensor. The confocal images were collected on a Zeiss LSCM 880 microscope using Airyscan in channel mode. Exposures were adjusted as needed to observe intracellular staining. Scale bar, 5 µm.

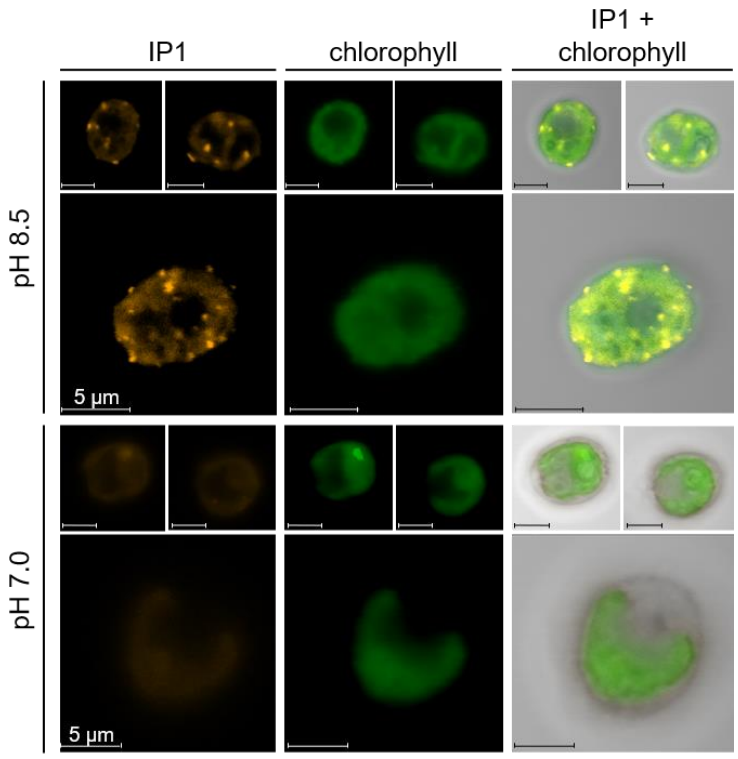

Figure 3.9. Fe^{2+} foci are observed in alkaline pH-grown cells but not in neutral pH-grown cells. The custom-made dye, IP1, was used to visualize Fe^{2+} distribution (shown in orange) in cells grown in pH 8.5 vs. pH 7.0 TAP medium with 200 µM Fe. Chlorophyll autofluorescence is shown in green. The overlaid images of IP1 and chlorophyll are shown on the right (IP1, yellow; chlorophyll, green). The confocal images were collected on a Zeiss LSCM 880 microscope using Airyscan in channel mode. Exposures were adjusted as needed to observe intracellular staining. Scale bar, 5 µm.

3.3.3 Conclusions

Imaging results from NanoSIMS, XFM, and confocal fluorescence microscopy suggested that Chlamydomonas might have selective housing of excess Fe under different over-accumulating conditions. In stationary-phase cells, which accumulated less than 5-fold of Fe compared to log-grown cells, the correlation between intracellular Fe, Ca, and P was weak. In alkaline pH-grown cells, which accumulated 10-fold or more Fe compared to neutral pH-grown cells, a strong positive correlation was observed between Fe, Ca, and P. A substantial number of acidic bodies and Fe^{2+} foci were also detected in the cells grown at alkaline pH, but not in the cells grown at neutral pH. However, under the alkaline condition, cell growth was delayed. The stationary-phase cells, in comparison, exhibited no irregular growth phenotypes. Therefore, the acidocalcisome appears to be an Fe accumulation site when the cells are physiologically stressed (*e.g.* in an alkaline environment) and/or when the intracellular Fe content exceeds a certain biological capacity. When the cells are healthy and/or accumulating only a moderate amount of excess Fe (*e.g.* during stationary growth), ferritin and potentially other Fe proteins may be picking up most of the surplus Fe.

CHAPTER 4

Identifying the Molecular Mechanisms for Excess Fe Sequestration and Mobilization

4.1 Background

In many organisms including Chlamydomonas, the mechanism of high-affinity Fe uptake under Fe limitation has been of particular interest, as it is a trait important for survival in many habitats. The results of these studies have helped distinguish components of Fe acquisition pathways in various organisms, which are typically induced under Fe deficiency. In Chlamydomonas, as introduced in Section 1.3.3, acclimation to low Fe availability includes stimulated expressions of the FOX1/FTR1 ferroxidase/permease system, the FRE1 ferric reductase, the IRT ferrous Fe transporters, and the algal-specific proteins FEA1 and FEA2 (80). In contrast, Fe sequestration in cells under luxury Fe condition, as well as the distribution and mobilization of intracellular Fe, are less studied, even though these aspects are just as crucial for cells to successfully acclimate to and compete in environments with fluctuating Fe supplies. Nevertheless, several candidate intracellular Fe transporters have been distinguished in Chlamydomonas, including CVL1, CVL2, and NRAMP4 (46, 80). They were identified based on protein sequence similarity and comparative transcriptional analyses of homologous transporters known in plants and fungi. CVL1 and CVL2 are hypothesized to mobilize Fe into vacuoles like the acidocalcisome, while NRAMP4 is hypothesized to move Fe out of vacuoles (a more in-depth introduction of the CVL and NRAMP transporters is presented in Section 1.3.3 and the references therein). However, none of these transporters has been biochemically characterized in detail in Chlamydomonas.

As shown in the earlier chapters, Chlamydomonas cells can indeed accumulate excess Fe and might have a couple of selective storage sites for it. To follow up on the transport aspect of excess Fe in Chlamydomonas, I targeted two specific questions: 1) What is the molecular mechanism underlying the over-accumulation of Fe in cells? And 2) What are the proteins

responsible for mobilizing excess intracellular Fe to support growth, if such Fe is bioavailable during Fe limitation?

To address the first question, I completed a comparative transcriptomic analysis of wild-type cells grown in alkaline vs. neutral media, given that alkalinity has been shown to be an impactful factor for Fe over-accumulation (see Chapter 2). The results identified candidate components of the Fe acquisition pathways that play a role in enabling over-accumulation of Fe in cells, which, significantly, included the FEA proteins. Accordingly, the cellular Fe content and localization in the mutant strains with a disrupted *fea1* or *fea2* gene were analyzed under alkaline condition by ICP-MS/MS and NanoSIMS imaging. Data comparison between the mutant strains and the wild-type strain provided further evidence of the contributions of the FEA proteins on Fe accumulation and distribution in Chlamydomonas.

Meanwhile, to address the second question, I first assessed the bioavailability of excess Fe stored in wild-type cells by monitoring their growth and elemental composition during a transition from Fe-excess to Fe limitation. Wild-type cells that over-accumulated Fe, induced by medium alkalinity or during stationary phase, were washed and inoculated into Fe-free medium. If the excess Fe stored within cells is bioavailable, then cell growth in the Fe-free medium should occur according to the quantity of Fe retained in the cells prior to the medium transfer, until either the minimal Fe quota is reached or until another nutrient becomes limiting and stationary phase is reached. The experimental condition under which the wild-type cells were able to readily utilize their internal Fe supply during Fe starvation was implemented in the following studies of mutants.

In a similar, targeted manner, 10 separate mutant strains with loss of function in proteins of known or presumed involvement in Fe uptake, intracellular distribution, or storage were screened for their potential roles in acquiring and/or allocating excess Fe. Cell growth and Fe content were monitored during the accumulation (under the excess Fe condition) and the release of Fe (during subsequent Fe limitation) into and out of storage sites. Under the excess Fe condition, the mutant strains with loss of function of a component needed for accumulating Fe

would have a lower cellular Fe content compared to the wild-type strain. In the other direction, if the affected gene product is required for distributing Fe from a storage site (*e.g.* ferritin and/or acidocalcisomes), then the corresponding mutant strain would grow poorly after transiting from Fe-excess to Fe-free medium, as the cells are unable to utilize their internal Fe supply. I tested three groups of mutant strains: i) *fre1*, *fea1*, and *fea2*; each of these strains lacks the respective high-affinity Fe uptake protein that facilitates Fe assimilation under Fe deficiency; ii) *cvl1*, *cvl2*, *nramp1*, and *nramp4*; the genes disrupted in these strains encode proteins that are hypothesized to have a role in intracellular Fe distribution; and iii) *fer1*, which lacks ferritin1, and *vtc1* as well as *v-ppase*, which are defective in polyP synthesis in the acidocalcisome and acidification of the organelle, respectively. The three strains in this last group are potentially affected in the intracellular storage of excess Fe. All mutant strains listed were created by insertional mutagenesis using the background strain CC-4533, and have been made publicly available by the Chlamydomonas Library Project (CLiP) (17, 18). The CC-4533 strain was used as the reference wild-type strain in all experiments presented in this dissertation. The strains were obtained through the Chlamydomonas Resource Center (http://chlamycollection.org/) and were each genotypically confirmed by PCR (by P. Salome, Merchant group, UCLA).

Altogether, the results of these experiments established a molecular framework for how cells sequester and mobilize Fe intracellularly in Chlamydomonas.

4.2 Methods and Materials

4.2.1 Strains

Wild-type *Chlamydomonas reinhardtii* strain CC-4533 was used for all experiments. In the analysis probing for components important for Fe accumulation and distribution, the following mutant strains were used: *fre1* (LMJ.RY0402.217414), *fea1* (LMJ.RY0402.144450), *fea2* (LMJ.RY0402.070229), *cvl1* (LMJ.RY0402.170889), *cvl2* (LMJ.RY0402.253084), *nramp1* (LMJ.RY0402.068314), *nramp4* (LMJ.RY0402.187341), *vtc1* (LMJ.RY0402.126297), *v-ppase*

(LMJ.RY0402.114778), and *fer1* (LMJ.RY0402.112447). The insertion junction IDs shown in parentheses are as specified in the CLiP mutant library. All strains were obtained from the Chlamydomonas Resource Center (http://chlamycollection.org/). Upon receipt of the strains, their insertion sites were individually verified by PCR (by P. Salome, Merchant group, UCLA).

4.2.2 Culture conditions

Other than the conditions specified individually in the subsequent sections, all strains were cultured with growth parameters controlled exactly as described in Section 2.2.2. All media were titrated using trace metal grade acetic acid (Fisher, A507-P212) and KOH before cell inoculation to pH 7.0 or pH 8.5, as specified in the subsequent sections.

All Fe-free media were prepared in flasks and graduated cylinders that were treated with 6N HCl overnight, and then rinsed seven times with Milli-Q water before use to minimize trace metal contamination from the vessels. The Fe-free TAP media were prepared as described in Section 2.2.2 but without any Fe added.

4.2.3 RNA extraction and library preparation

For the comparative transcriptomic analysis, total RNA was extracted from cells grown in TAP medium containing the micronutrient composition according to (25), but with 200 µM instead of 20 µM of Fe. Prior to cell inoculation, the medium was titrated to either pH 7.0 or 8.5. Four cultures were grown in parallel for each pH condition with all other parameters controlled as described in Section 2.2.2. When the density of the cultures reached ~2 x 10^6 cell/ml, 5 x 10^7 cells from each culture were collected by centrifugation at 1,500 x*g* for 5 min at 4ºC. Cells were lysed in a solution containing 100 mM Tris-Cl (pH 7.5), 300 mM NaCl, 30 mM Na_2-EDTA (from a stock at pH 8.0), 4% SDS, and 80 ng/ml proteinase K (Fisher BP700-100). Total RNA from the lysate was isolated with the TRIzol reagent (Invitrogen) according to the manufacturer's protocol, except that 100% chloroform was used instead of 24:1 chlorofrom : isoamyl alcohol. DNA was removed

by digestion with RNase-free Turbo DNase (Ambion) according to the manufacturer's instructions. RNA concentration and quality were determined on a Nanodrop 2000 (Thermo Fisher Scientific) and an RNA 6000 microfluidic chip on a Bioanalyzer 2100 (Agilent). RNA-Seq libraries were generated from total RNA with the KAPA Stranded mRNA-Seq Kit (Roche) following the manufacturer's protocol and sequenced on the Illumina HiSeq 3000 platform.

4.2.4 Transcriptomic data analysis

Analysis of the resulting transcriptomic data above was performed as described in (112) (by S. Gallaher, Merchant group, UCLA). Briefly, sequenced reads were mapped to the *C. reinhardtii* v.5.5 genome assembly and annotations (available at https://phytozome.jgi.doe.gov/) using RNA STAR v2.0.4j (234) with --maxIntronSize 3000. Transcript abundance estimates in terms of Fragments Per Kilobase of transcript per Million mapped fragments (FPKM) were calculated for all genes with cuffdiff v2.0.2. (235) using the following settings: --multi-read-correct --max-bundle-frags 1000000000 --library-type fr-firststrand. Transcriptomic data including raw sequencing reads and FPKM determinations were deposited in the National Center for Biotechnology Information Gene Expression Omnibus repository at accession number GSE169762. Differentially expressed genes were identified from raw counts per gene with the DESeq2 package in the R statistical computing platform using the following criteria: A) Benjamini-Hochberg-adjusted *p*-value of < 0.01; B) mean FPKMs across all sampled libraries > 1 FPKM; and C) |fold change| $\geq$ 2. The mean FPKMs were calculating from averaging the FPKM of all four cultural replicates. The fold change was calculated as the average FPKM of the pH 8.5 sample relative to that of the pH 7.0 sample. All genes that were at least 2-fold differentially expressed were entered into the Algal Functional Annotation Tool (http://pathways.mcdb.ucla.edu/algal/) to be categorized based on the MapMan ontology terms. Genes that were not assigned by the annotation tool into any category were curated manually, based on literature functions.

4.2.5 Analysis of cell growth, elemental composition, and intracellular Fe distribution of the *fea* mutant strains under alkaline condition

Wild-type CC-4533 strain and the *fea1* and *fea2* mutant strains were inoculated at 1 x 10^4 cells/ml into 100 ml of 200 µM Fe-containing TAP medium at either pH 7.0 or pH 8.5. See Sections 4.2.1 and 4.2.2 for strain information and culture condition. Cells were inspected visually and counted every 24 h post-inoculation for one week. When the culture density reached 2-4 x 10^6 cells/ml, 5 x 10^7 cells from each culture were collected for ICP-MS/MS analysis. In parallel, 1 x 10^7 cells were also collected from the pH 8.5 cultures of both the wild type and the mutant strains for NanoSIMS imaging. The procedure for ICP-MS/MS analysis is described in Section 4.2.9. NanoSIMS sample preparation and analysis were performed as described in Sections 3.2.2 and 3.2.3. Samples were collected from three independent cultures grown in parallel throughout the experiment.

4.2.6 Assessment of bioavailability of stored Fe in cells

To determine whether excess Fe in cells was available for use in face of Fe starvation, wild-type CC-4533 cells were transferred from two different Fe-over-accumulating conditions, as listed below, into Fe-free condition. Cell growth and elemental composition were assessed before and after the transition. In all experiments, samples were collected from three independent cultures grown in parallel. The procedures are described as follows:

i) Fe accumulation under alkaline pH condition: Cells were inoculated at 1 x 10^4 cells/ml into 100 ml of 200 µM Fe-containing TAP medium at pH 8.5. Cells were visually monitored and counted every 24 h post-inoculation for 10 days. During mid-log growth phase (~2-4 x 10^6 cells/ml), 5 x 10^7 cells were collected for ICP-MS/MS analysis. In parallel, 1 x 10^7 cells were collected separately by centrifugation at 2,600 x*g* for 1 min. The cell pellet was washed once with 1 mM Na_2-EDTA and twice with 10 mM sodium phosphate (pH 7.0), and then resuspended in 100 ml of Fe-free TAP medium at either pH 7.0 or pH 8.5 (initial

cell density of 1 x 10^5 cells/ml). Cells in the Fe-free media were counted every 24 h post-inoculation for 10 days to establish growth curves, and 5 x 10^7 cells were collected for ICP-MS/MS analysis at 10-days post-inoculation. Spent medium from each culture was also collected and analyzed by ICP-MS/MS to verify that there was no external Fe contamination.

ii) Fe accumulation during stationary phase: Cells were inoculated at 1 x 10^4 cells/ml into 100 ml of TAP medium with 200 µM Fe at pH 7.0. Cultures were visually monitored and the cells were counted every 24 h post-inoculation for 10 days. A total of 5 x 10^7 cells was collected for ICP-MS/MS analysis on day 4, 7, and 10 post-inoculation; the time points corresponded to early stationary phase when culture density first reached 7-9 x 10^6 cells/ml (day 4), stationary phase when culture density reached ~1 x 10^7 cells/ml (day 7), and late stationary phase (day 10), at which point culture density remained at ~1 x 10^7 cells/ml. In parallel to sample collection for ICP-MS/MS analysis, 1 x 10^7 cells were separately collected by centrifugation at 2,600 x*g* for 1 min. Cell pellets were washed once with 1 mM Na_2-EDTA and twice with 10 mM sodium phosphate (pH 7.0). Each cell pellet was resuspended in 100 ml of Fe-free TAP medium at pH 7.0. Cells from the Fe-free media were counted every 24 h post-inoculation for one week and sampled for ICP-MS/MS analysis at 7-days post-inoculation. Spent medium from each culture was also analyzed by ICP-MS/MS to verify that there was no external Fe contamination.

4.2.7 Identifying candidate components for excess Fe accumulation and distribution

Wild-type strain CC-4533 and the 10 mutant strains listed in Section 4.2.1 were inoculated at 1 x 10^4 cells/ml into 100 ml of TAP medium with 200 µM Fe at pH 7.0. All cultures were visually monitored, and the cells were counted every 24 h post-inoculation for 14 days. A total of 5 x 10^7 cells was collected for ICP-MS/MS analysis at 3-, 4-, 7-, 10-, and 14-days post-inoculation. The time points corresponded to i) log phase, when culture density was at 2-4 x 10^6 cells/ml (day 3);

ii) early stationary phase, when culture density first reached 7-9 x 10^6 cells/ml (day 4); iii) stationary phase, when culture density reached ~1 x 10^7 cells/ml (day 7); iv) late stationary phase (day 10); and v) prolonged stationary phase (day 14). At late and prolonged stationary phase, culture density remained at ~1 x 10^7 cells/ml. At 10-days post-inoculation, 1 x 10^7 cells were also collected separately by centrifugation at 2,600 x*g* for 1 min. The cell pellets were washed once with 1 mM Na_2-EDTA and twice with 10 mM sodium phosphate (pH 7.0), and then resuspended in 100 ml of Fe-free TAP medium at pH 7.0. Cultures in the Fe-free media were visually inspected, and the cells were counted every 24 h post-inoculation for one week. At 7-days post-inoculation, the cells from the Fe-free media were sampled for chlorophyll quantification and ICP-MS/MS analysis. Spent medium from each culture was also analyzed by ICP-MS/MS to verify that there was no external Fe contamination. All samples were collected from three independent cultures grown in parallel throughout the experiment.

4.2.8 Determination of growth rate and number of generations

Cell count, as well as calculations of the growth rate of cells and their total number of generations until stationary phase were performed as described in Section 2.2.4.

4.2.9 Quantitative elemental content analysis by ICP-MS/MS

Sample preparation and analysis for ICP-MS/MS were performed as described in Section 2.2.5. However, due to considerable variation in the cellular S content between samples (*e.g.* wild-type vs. mutant strains), cell number instead of S content was used as the normalization factor in all ICP-MS/MS analyses reported in this chapter.

4.2.10 Chlorophyll content quantification

Chlorophyll content was measured as described in (62). Briefly, cells were collected by centrifugation at 12,000 x*g* for 2 min from 1-ml aliquots of cultures. The cell pellets were

resuspended by vortex in a 1-ml mixture of 80% acetone, 20% methanol to extract chlorophyll. Cell debris and precipitated proteins were removed by centrifugation. Total chlorophyll (*a* and *b*) content was estimated from the absorbance at 646.6 and 663.6 nm, measured on a VWR UV-6300PC UV/Visible Spectrophotometer. Absorbance at 750 nm was used as a reference to remove background from cell debris. Samples were collected from three independent cultures grown in parallel, and each sample was measured in 2-3 technical replicates.

4.3 Results and Discussion

4.3.1 The abundances of *FEA2*, *FEA1*, and *NRAMP1* transcripts increase significantly under alkaline vs. neutral pH condition.

To investigate the molecular mechanisms underlying the over-accumulation of Fe in alkaline pH-grown cells, a comparative transcriptomic analysis of Chlamydomonas cells grown in media with excess Fe (200 μM medium Fe) at pH 8.5 vs. pH 7.0 was performed. The results revealed 2523 genes (~14% of the genome) whose transcripts accumulated differentially, of which 1319 were significantly reduced and 1204 were significantly increased ($\geq$ 2-fold change) (Figure 4.1A). The corresponding genes were curated both manually and using the Algal Functional Annotation Tool (http://pathways.mcdb.ucla.edu/algal/) categories based on their proposed functions using MapMan ontology terms. Among the genes showing an increased transcript abundance, 15 of them encode proteins known for metal handling (Figure 4.1B), and about half of these are linked to Fe homeostasis (Table 1). In particular, *FEA2*, which codes for an algal-specific Fe assimilation protein in the periplasm, has a 138-fold increase in the abundance of its transcripts in the alkaline compared to the neutral pH condition. The abundance of the homologous *FEA1* transcript was elevated by just 3-fold. The abundance of *NRAMP1* transcripts, coding for a candidate Fe transporter in Chlamydomonas, increased 4-fold under the alkaline condition, and the abundance of the *FOX1* transcript, which encodes the multicopper ferroxidase essential for high-affinity Fe uptake in Chlamydomonas, was increased by 2-fold.

FOX2, encoding a second putative ferroxidase, showed a 4-fold increase in transcript abundance. In addition, two genes that encode putative Fe^{3+}-reductases, *TEF22* and Cre05.g241400, were induced by 2- and 3-fold, respectively. No metal handling-associated gene was detected with a significantly reduced transcript abundance comparing the alkaline vs. neutral pH samples.

Meanwhile, the abundances of 42 transcripts associated with transport but not with metals were elevated significantly in the alkaline pH condition (Figure 4.1B). Most of these transcripts encode transporters for Ca, protons, and/or phosphate (Table 1). They include Cre01.g036350, Cre09.g410050, Cre04.g217954, and Cre09.g410100, which code for putative plasma membrane ATPases that translocate Ca^{2+}, as well as Cre01.g044050, which codes for a putative V-type H^{+}-ATPase subunit. The transcripts encoding PTB12, PTB7, and PHT4 in the PHT phosphate transporter family were also increased by 2-fold or higher. Interestingly, two other genes in this phosphate transporter family, *PTA3* and *PTB6*, were found among the 32 transport-associated (but not metal-associated) genes whose transcripts were significantly reduced in the alkaline condition (Figure 4.1B, Table 1). Beside *PTA3* and *PTB6*, the other 30 genes in this group mostly encode various unspecified solute transporters.

The *FEA1* and *FEA2* genes in Chlamydomonas are localized on chromosome 12 next to each other in a parallel, head-to-tail orientation. They share ~70% transcript sequence identity and 56% protein sequence identity, with *FEA2* having two additional introns. Both genes are expressed in standard (neutral pH) photoheterotrophic, Fe-replete conditions and are both highly induced under Fe deficiency. However, *FEA1* is typically the dominant *FEA* expressed. Specifically, when replete Fe is provided (20 µM medium Fe), the abundance of *FEA1* transcripts is ~35-fold greater than that of *FEA2*; during Fe deficiency (1 µM medium Fe), it is ~6-fold greater; and when Fe is limiting (0.25 µM medium Fe), *FEA1* is ~1.3-fold higher than *FEA2* (Supplementary Table 1) (24, 82). Abundances of the corresponding FEA proteins change by the same patterns as observed with their transcript abundances (24, 82). It was therefore intriguing to find the abundance of *FEA2* transcripts to be ~40-fold higher than that of *FEA1* under the

alkaline condition. Comparing transcriptomic data across multiple experiments (data not shown), the abundance of *FEA2* transcripts in the alkaline condition was comparable to that observed under Fe deficiency. In contrast, the abundance of *FEA1* transcripts in the alkaline condition was similar to that noted in Fe-replete conditions. This result indicated that the FEA2 protein might have a specialized function that is not shared by FEA1, and the function might relate to location or interaction partners. Also, FEA1 may be responsive to carbon nutrition. Studies have shown that the abundance of *FEA1* transcripts is reduced in low CO_2, but the abundance of *FEA2* transcripts is not responsive to changes in CO_2 (82, 236). As cells grow, they convert bicarbonate from the growth medium into CO_2 and deplete it, which contributes to the increase in medium pH. Thus, the regulation of *FEA1* by CO_2 might relate to a role for bicarbonate in facilitating Fe binding to FEA1, and/or modification of Fe demand by carbon availability.

The abundance of the *NRAMP1* transcript increased about 4-fold in the alkaline condition compared to the neutral pH condition. As introduced in Section 1.3.3, the *NRAMP1* gene encodes a membrane-localized, divalent cation transporter (80). Studies have shown that the abundance of its transcripts is increased in Chlamydomonas cells under Mn limitation, but it is un-responsive to changes in the cellular Fe status (24, 102). Nevertheless, the expression of *NRAMP1* in yeast can rescue strains defective in either Mn or Fe transport to different extents (100, 101), indicating that NRAMP1 can mobilize both Mn and Fe. Considering that Mn accumulation was not affected by changes in the growth medium pH (Figure 2.5D), it is more likely that the induction of the *NRAMP1* transcript in the alkaline condition was associated with Fe transport rather than Mn. The subcellular localization of NRAMP1 in Chlamydomonas has not been verified, so it is unclear whether the protein might facilitate transport of Fe across the plasma membrane or intracellularly, *e.g.* to/from vacuoles and other organellar destinations. Recently, Castaings et al. showed that NRAMP1 in Arabidopsis in fact cycles dynamically between the plasma membrane and endosomal compartments in response to Mn availability to control uptake and prevent toxicity

(126). It is possible that NRAMP1 in Chlamydomonas is similarly mobile and might play a part in both the acquisition and allocation of Fe.

The increase in the abundance of the *FOX1* transcript under the alkaline vs. neutral pH conditions was not unexpected, given that FOX1 is a key component for high-affinity Fe uptake in Chlamydomonas. In comparison, the 4-fold increase in the *FOX2* transcript was more surprising. In the Chlamydomonas genome, *FOX1* and *FOX2* transcripts share 54% sequence identity (237). However, studies have shown that the expression of *FOX2* is not very sensitive to the Fe status of the cells. While the *FOX1* transcript is induced in cells within an hour of Fe-deficient growth (21, 82, 237), an increase in the abundance of *FOX2* is only observed after 2 days of Fe starvation (237). Moreover, the abundance of *FOX2* transcripts is generally much lower than that of *FOX1* (~6-fold and ~18-fold lower under excess and replete Fe conditions at neutral pH, respectively, Supplementary Table 1) (24). Accordingly, FOX2 has been thought to play a minor role in Fe homeostasis in Chlamydomonas. Some have proposed that FOX2 might be a component of a low-affinity Fe transport system (70, 237). The present transcriptomic data suggested that perhaps FOX2, like FEA2, has a specialized function under specific circumstances. Speculations aside, further characterization of FOX2 is required to determine its exact role.

Another interesting result is the moderate increase in the abundances of *TEF22* and Cre05.g241400 transcripts under the alkaline condition. The two transcripts, each encoding a putative Fe^{3+}-reductase, are also increased in abundances under Fe deficiency by ~8-fold and in Fe limitation by ~16-fold (Supplementary Table 1) (24). Proteomic studies indicated that TEF22 is located in the mitochondrion, suggesting that it might be involved in supplying Fe^{2+} for mitochondrial respiratory complexes (238, 239). Note that *TEF22* is also divergently-transcribed from the same promoter sequences as *FEA1* (240). Separately, a protein similarity network analysis showed that Cre05.g241400 is more closely related to the Fe^{3+}-reductases from plants than from bacteria and fungi (24), but its localization has not been investigated. It has been proposed that Cre05.g241400 might function to reduce intracellular Fe^{3+} when the metal is

transported into other organelles, such as the chloroplast or vacuoles, or, potentially it may work with TEF22 (24).

The result that many Ca, proton, and phosphate transporter genes were differentially regulated in the alkaline vs. neutral pH conditions is consistent with the hypothesis that an elevated external pH disrupts the electrochemical gradient across the plasma membrane and/or internal organelle boundary membranes (*e.g.* vacuoles). It is possible that cells attempt to restore gradient balance by inducing and repressing the expression of various ion transporters. In particular, the increased abundance of Cre01.g044050 transcripts, which encode a putative V-type H^+-ATPase subunit, might be linked to the large number of acidic bodies observed in alkaline pH-grown cells (Figure 3.8). The formation of acidic vacuoles might also facilitate pH homeostasis.

The four putative Ca^{2+}-translocating ATPases whose transcripts were significantly increased under the alkaline condition, Cre01.g036350, Cre09.g410050, Cre04.g217954, and Cre09.g410100, have ~70% sequence identity at the protein level with various autoinhibited Ca^{2+}-ATPases (ACA) in Arabidopsis (data not shown). In plants, the ACAs are found mainly in the plasma membrane, but also in membranes of vacuoles, the chloroplast, and the endoplasmic reticulum (241). They function in the active transport of Ca^{2+} and can also participate in Ca signaling (242, 243). In Chlamydomonas, few Ca^{2+}-ATPases have been characterized in detail. If one or more of the above Ca^{2+}-ATPases is/are localized to the plasma membrane in Chlamydomonas and function to export Ca from the cells, their increased expression could explain the substantially reduced Ca content observed in alkaline-pH grown cells (Figure 2.5E). Alternatively, their up-regulation could be a consequence of the cells' attempt to internalize more Ca due to the lack of intracellular Ca.

Many of the phosphate transporters found differentially regulated in the alkaline vs. neutral pH conditions belong to the PHT phosphate transporter family. In plants, the PHTs are transmembrane proteins that mediate both uptake and intracellular distribution of phosphates, and they are well studied (244, 245). In comparison, components for phosphate transport in green

algae are not as well characterized. Studies have found 25 putative *PHT* genes in Chlamydomonas, divided into the subfamilies *PTA*, *PTB*, and *PHT* (244, 246). The *PTA* genes encode proton/phosphate co-transporters (247), whereas the PTB proteins are hypothesized to be sodium/phosphate symporters (248). Members in the PHT subfamily might transport either protons or sodium along with phosphates. PTA and PTB proteins are both predicted to be located in the plasma membrane (244, 248). The abundances of 10 of the 25 *PHT* transcripts in Chlamydomonas are significantly increased under phosphate starvation, including *PHT4*, *PTB7*, and especially *PTB12*, indicating their potential roles as high-affinity phosphate transporters (244). Accordingly, the increase in the abundances of these three transcripts under the alkaline condition might be explained by the low intracellular P content in alkaline pH-grown cells (Figure 2.5F). In the opposite direction of regulation, the abundance of the *PTA3* transcript was found repressed both in the alkaline condition and under phosphate starvation (244, 246). Thus, PTA3 might be a low-affinity phosphate transporter that only operates in P-replete conditions, or it might function strictly as a phosphate exporter. Since the PTA proteins co-transport protons and phosphates, alteration in the expression of *PTA3* might also facilitate pH homeostasis. Lastly, as shown by the present data, the abundance of *PTB6* transcripts was reduced by ~3-fold in alkaline vs. neutral pH media. It is, however, not impacted by phosphate nutrition in Chlamydomonas (244, 246). The different patterns of expression suggested that the PTB6 protein, like FEA2, might carry a unique function in an alkaline environment.

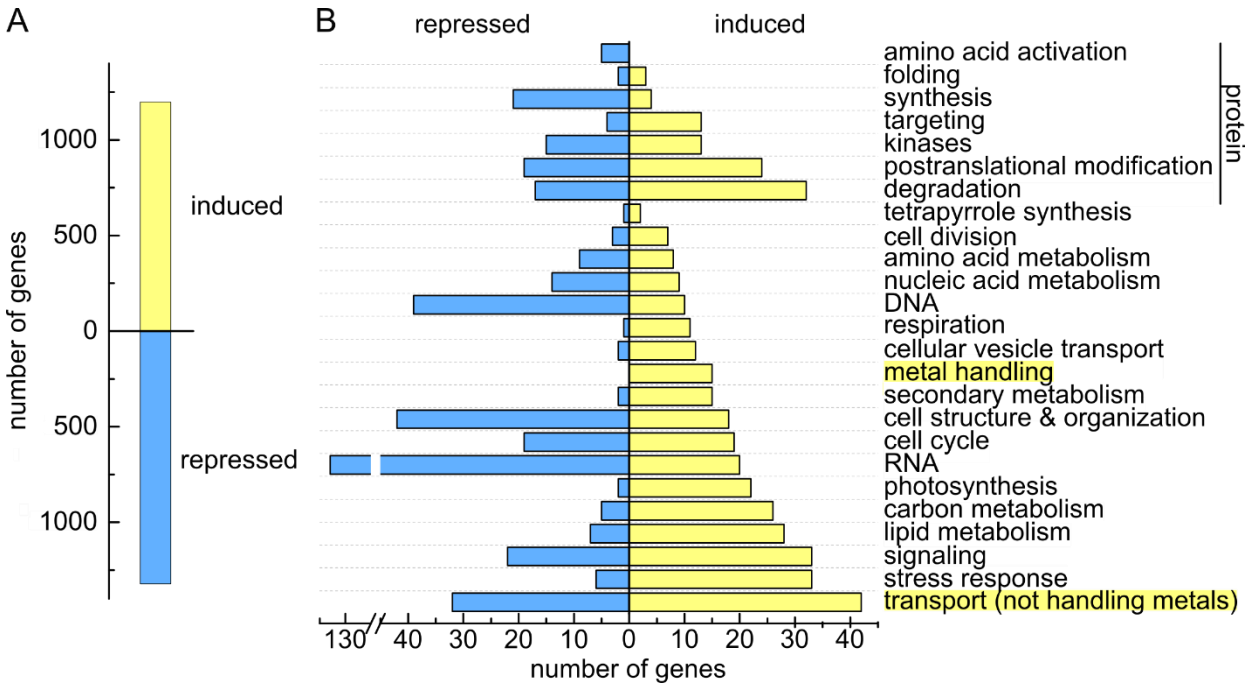

Figure 4.1. Summary of changes in the Chlamydomonas transcriptome in response to alkaline pH in excess Fe condition. Transcript abundances were estimated by RNA-Seq (Benjamini-Hochberg-adjusted $p < 0.01$). (A) Total number of genes with an absolute change in transcript abundance $\geq$ 2-fold in wild-type CC-4533 cells grown in pH 8.5 vs. pH 7.0 TAP media containing 200 µM Fe. (B) The genes represented in (A) were categorized according to MapMan ontology terms and literature functions, excluding those that were either categorized as “miscellaneous” or could not be assigned due to a lack of information. Selected genes from the highlighted categories are shown in Table 1.

Table 1. Selected metal handling- and non-metal-associated transport genes from Figure 4.1

Process	Locus ID	Gene Name	Description	mean FPKM pH 7.0	mean FPKM pH 8.5	fold change
iron homeostasis	Cre12.g546550	*FEA1*	Fe-assimilating protein	2.3	7.3	3.2
	Cre12.g546600	*FEA2*	Fe-assimilating protein	1.0	143	138
	Cre09.g393150	*FOX1*	Multicopper ferroxidase	18	41	2.2
	Cre12.g531200	*FOX2*	Multicopper ferroxidase	3.4	12	3.5
	Cre17.g707700	*NRAMP1*	Mn/Fe transporter	3.4	12	3.5
	Cre12.g546500	*TEF22*	DOMON domain; cytochrome b_{561} / Fe^{3+}-reductase domain	0.9	2.8	3.1
	Cre05.g241400		Fe^{3+} reductase-like transmembrane component *	1.6	3.1	2.0
proton, calcium, and phosphate transport	Cre16.g655200	*PTB6*	Na^+/Phosphate symporter	6.5	1.9	0.3
	Cre12.g489400	*PTB7*	Na^+/Phosphate symporter	5.8	13	2.3
	Cre02.g144650	*PTB12*	Na^+/Phosphate symporter	0.04	7.4	188
	Cre16.g686750	*PTA3*	H^+/phosphate symporter *	99	1.1	0.1
	Cre08.g379550	*PHT4*	Na^+-dependent phosphate transporter	3.0	15	5.1
	Cre16.g681750		Ca^{2+}-transporting ATPase *	0.8	5.9	7.0
	Cre01.g036350		Ca^{2+}-transporting ATPase *	0.5	2.3	4.5
	Cre09.g410050		Ca^{2+}-translocating P-type ATPase *	2.1	8.5	4.0
	Cre04.g217954		Ca^{2+} transporting P-type ATPase *	1.8	4.7	2.7
	Cre09.g410100		Ca^{2+}-translocating P-type ATPase *	0.6	1.4	2.6
	Cre01.g044050		V-type H^+-transporting ATPase subunit *e* *	91	209	2.3

Locus IDs correspond to the *C. reinhardtii* v.5.5 genome annotations, available on Phytozome. Functional annotations were manually curated. Asterisks indicate putative functions.
The mean Fragments Per Kilobase of transcript per Million mapped fragments (FPKM) were calculated from individual analyses of 4 cultural replicates.

4.3.2 The FEA proteins likely facilitate Fe uptake but do not impact intracellular Fe distribution.

The comparative transcriptomic analysis reported in the preceding section revealed a significant increase in the abundance of the *FEA1* and especially *FEA2* transcripts in cells grown in alkaline vs. neutral pH media. Following up on this result, in order to further investigate their roles in the over-accumulation of Fe in alkaline condition, *fea1* and *fea2* insertional mutants were obtained from the Chlamydomonas Resource Center. Along with the congenic wild-type strain (CC-4533), the mutant strains were grown in medium at pH 8.5 or pH 7.0 with excess Fe (200 μM). Cell growth and the elemental composition of each strain at mid-log growth was assessed and compared.

In terms of growth, both the *fea1* and *fea2* strains grew at virtually the same rate and produced the same number of generations as the wild-type strain, regardless of pH conditions (Figure 4.2). ICP-MS/MS data showed that the S content in both mutant strains was comparable to that in the wild-type strain. The S content was higher in all strains in the alkaline medium than in the neutral pH medium (Supplementary Figure 11D). Although previous data indicated that cellular S content linearly correlates with biomass in the wild-type strain (Supplementary Figure 2), this relationship has not been confirmed in the *fea* strains. Therefore, cell number instead of S was used as a normalization factor for the other elements in this ICP-MS/MS analysis.

At neutral pH, the Fe content in the *fea* mutant strains was similar to that in the wild type. However, under alkaline pH condition, the *fea1* and *fea2* mutants accumulated 1.8-fold and 2.4-fold less Fe, respectively, relative to the wild-type strain (Figure 4.3A). Separately, Cu content in the *fea1* mutant was comparable to that in the wild type under both pH conditions, but the *fea2* mutant accumulated significantly more Cu than did the wild-type and the *fea1* strains, particularly in alkaline condition (Supplementary Figure 11A). Both the *fea1* and *fea2* strains showed a slight but significant increase in their Zn contents relative to the wild type at alkaline pH, but not at neutral pH (Supplementary Figure 11B). Mn accumulation did not change in either *fea* strain

between the two different pH conditions, and it was at the same level as observed in the wild-type strain (Supplementary Figure 11C).

Consistent with previous results (Figure 2.5E-F), Ca and P accumulation in the wild-type strain were substantially reduced under alkaline vs. neutral pH conditions (Ca by 8-fold, and P by 2-fold) (Figure 4.3B-C). In contrast, in the *fea* mutants, the Ca and P contents were either not reduced or only mildly affected by medium alkalinity. In particular, at alkaline pH, the Ca content in the *fea1* mutant was 4-fold greater than that in the wild type, but it was still 2-fold less than the amount that was accumulated at neutral pH (Figure 4.3B). The P content in the *fea1* strain was unchanged in the alkaline vs. neutral pH conditions (Figure 4.3C). This level of P was comparable to that in the wild type at neutral pH, but ~2-fold greater than the amount observed in the wild type at alkaline pH. The *fea2* mutant showed virtually no difference in either Ca or P accumulation between the alkaline and neutral pH conditions. Interestingly, its P content in both pH conditions was significantly greater than the P content observed in the wild-type and the *fea1* strains. Specifically, at neutral pH, the P level in the *fea2* mutant was 1.3-fold higher than that in the *fea1* mutant and the wild type; at alkaline pH, it was 1.5-fold higher compared to the *fea1* mutant and 2.5-fold higher compared to the wild type.

To find out whether the FEA proteins also affect intracellular distribution of Fe, the *fea1* and *fea2* mutants along with the wild-type strain, grown under alkaline pH condition with excess Fe, were analyzed by NanoSIMS. In line with the ICP-MS/MS data, a lower count of $^{56}Fe^{+}$ but higher counts of $^{31}P^{+}$ and ^{40}Ca were detected in the *fea* strains relative to the wild type (Figure 4.4A). Nonetheless, most Fe in all the strains was observed in foci, suggesting that the Fe in the mutants was sequestered into a specific site as in the wild type. A substantially higher number of P and Ca foci was noted in the mutants compared to the wild type. Also, an even distribution of P and Ca at lower intensities could be seen within the cells in the mutant strains, which was less obvious in the wild-type strain, possibly because of the lower counts of P and Ca detected in the wild-type sample.

The extent of colocalization between the Fe, Ca, and P foci in the mutant vs. wild-type strains was estimated qualitatively and quantitatively, as described in Sections 3.2.3 and 3.3.1. Briefly, NanoSIMS images of the $^{56}Fe^+$, $^{40}Ca^+$, and $^{31}P^+$ distributions were overlaid to visually reveal colocalized areas of Fe (shown in green), Ca (red), and P (blue) (Figure 4.4A). Meanwhile, relative quantitative correlations of ion count between the three elements were plotted (Figure 4.4B-D) using non-overlapping regions of interest (ROIs) defined based on $^{12}C^+$ distribution, which approximated the cell areas in the images (Supplementary Figure 12). Results revealed similar correlative patterns between the two *fea* mutants, as shown in both the overlaid images and the correlative plots. Specifically, in both mutant samples, two groups of ROIs could be clearly distinguished: in one group, $^{40}Ca^+$, $^{31}P^+$, and a significant count of $^{56}Fe^+$ (count > 2) were detected (represented by black points in Figure 4.4B-D), whereas in the other group, only $^{40}Ca^+$ and $^{31}P^+$ but no $^{56}Fe^+$ were observed (represented by gray points in Figure 4.4B-D). In the wild-type sample, all three elements were detected in most of the defined ROIs. Using only the ROIs with a significant $^{56}Fe^+$ count, relative quantification showed strong positive correlations between $^{56}Fe^+/^{12}C^+$ and $^{31}P^+/^{12}C^+$ as well as $^{56}Fe^+/^{12}C^+$ and $^{40}Ca^+/^{12}C^+$ in all three strains (Figure 4.4B-C). In the wild-type sample, $R^2 = 0.89$ for both $^{56}Fe^+/^{12}C^+$ vs. $^{31}P^+/^{12}C^+$ and $^{56}Fe^+/^{12}C^+$ vs. $^{40}Ca^+/^{12}C^+$, which is consistent with previous data (Figure 3.6). In the *fea1* and *fea2* samples, the R^2 values ranged from 0.92 to 0.96 for the two sets of correlations. This outcome suggested that under alkaline condition, most Fe accumulated in the *fea* mutant strains colocalized with Ca and P, as in the wild-type strain.

The relationship between $^{40}Ca^+$ and $^{31}P^+$ was also similar among the wild-type and the *fea* strains (Figure 4.4D). Using all ROIs, regardless of their Fe counts, the correlations between $^{40}Ca^+/^{12}C^+$ and $^{31}P^+/^{12}C^+$ in the mutant strains were strongly positive, with $R^2 = 0.88$ for the *fea1* mutant and 0.80 for the *fea2* mutant; that in the wild-type sample was slightly weaker, with $R^2 = 0.46$. Using only ROIs with an $^{56}Fe^+$ count > 2 improved correlations between Ca and P in all samples, especially the wild type ($R^2 = 0.73$ for the wild type, 0.93 for *fea1*, and 0.91 for *fea2*).

This result suggested that in alkaline condition, most Ca colocalized with P in cells, regardless of the presence of Fe, in the wild-type strain and particularly in the *fea* strains.

Under Fe deficiency, the loss of the FEA proteins results in poor growth of cells (82). Yet, the asymptomatic growth of the *fea* mutants compared to the wild type in excess Fe conditions, independent of medium pH, suggested that the functions of the FEA proteins are non-essential when Fe is abundant. Nonetheless, the FEA proteins appear to be at least partially responsible for the accumulation of excess Fe in Chlamydomonas, as indicated by the ~2-fold reduction in Fe content in the *fea* mutants relative to the wild-type strain at alkaline pH. In Arabidopsis, the introduced expression of Chlamydomonas FEA1 also enhances Fe accumulation (92), but the specific effect of FEA2 has not been shown in literature. Note that even with the ~2-fold reduction, the Fe content observed in the *fea* strains under alkaline condition was still substantially greater than the amount of Fe that the cells accumulated at neutral pH. This implied that while FEA1 and FEA2 likely facilitate Fe uptake, neither protein alone is the predominant component for the over-accumulation of Fe. It is possible that FEA1 and FEA2 both contribute to the Fe accumulation by complementing and potentially compensating each other in function. Experiments using a double mutant strain lacking both FEA proteins can help distinguish the functions between the two FEAs. However, generating such a strain may be challenging, given the adjacent location of the *FEA1* and *FEA2* genes in the Chlamydomonas genome, although the use of CRISPR may help in this endeavor. Furthermore, because Fe accumulation in neither *fea* strains was affected at neutral pH, it suggested that the FEA proteins might operate specifically under conditions that motivate acquisition of additional Fe; for instance, upon alkaline stress and during Fe limitation. Indeed, in both of these situations, the abundances of *FEA1* and *FEA2* transcripts increase significantly (Table 1) (24, 82). Consistently, the abundances of the FEA1 and FEA2 polypeptides are also elevated under Fe limitation (82), and preliminary data likewise revealed a higher abundance of the FEA proteins in cells grown in alkaline vs. neutral pH media (data not shown).

It was interesting to find the effect of medium alkalinity on Ca and P accumulations reversed in the *fea* mutants compared to the wild type. In the *fea1* strain, Ca accumulation was still partially reduced under the alkaline condition, but P accumulation was completely unaffected. In the *fea2* strain, not only was its Ca and P accumulation similar at alkaline vs. neutral pH, but its P content was in fact in excess compared to that in the wild type under both pH conditions. Such changes might be linked to the reduced Fe content in the mutant strains. Studies have shown that overloading Fe in cells can adversely affect the transport of other essential nutrients, including Ca and P (139, 249, 250). Thus, perhaps a lower accumulation of Fe in the alkaline condition allows for more regular accumulation of Ca and P. Changes in the quotas of other trace elements might also affect Ca and P accumulation. For instance, greater uptake of Cu, as observed in the *fea2* mutant, might consequentially induce the formation of acidocalcisomes for storage, which requires more Ca and P (61). In addition, the absence of FEA1 or FEA2 might have influenced the extent of Ca and P accumulations, since the difference in Fe contents between the two *fea* strains was not proportional to that in their Ca and P contents. In particular, FEA2 appears to have an effect on P accumulation, given the increased quantity of P observed in the *fea2* strain under both alkaline and neutral pH conditions, but the underlying reason is unclear.

Transport and accumulation aside, the intracellular distribution of Fe did not appear to be affected by the loss of functions of either FEA proteins. NanoSIMS data showed similarly strong and positive correlations between Fe (where Fe count was significant), P, and Ca in both *fea* strains as in the wild-type strain. This result suggested that as in the wild type, the Fe in the *fea* mutants was sequestered into a Ca- and P-filled site, likely the acidocalcisome, considering that a substantial fraction of the cellular P and Ca are found within acidocalcisomes in Chlamydomonas (63). While the FEA proteins are unlikely to play a direct role in distributing intracellular Fe, their impacts on the sequestration of other elements (*e.g.* Cu, Ca, and P) might indirectly affect the distribution patterns of those elements. The presence of foci containing only

Ca and P and no Fe, as observed in high number in the *fea* mutants, indicated that acidocalcisomes might be intended for purposes other than Fe storage. For example, they might serve as a reservoir for other trace metals and metabolites, and/or to balance ion gradients in cells that are substantially disrupted by high external pH.

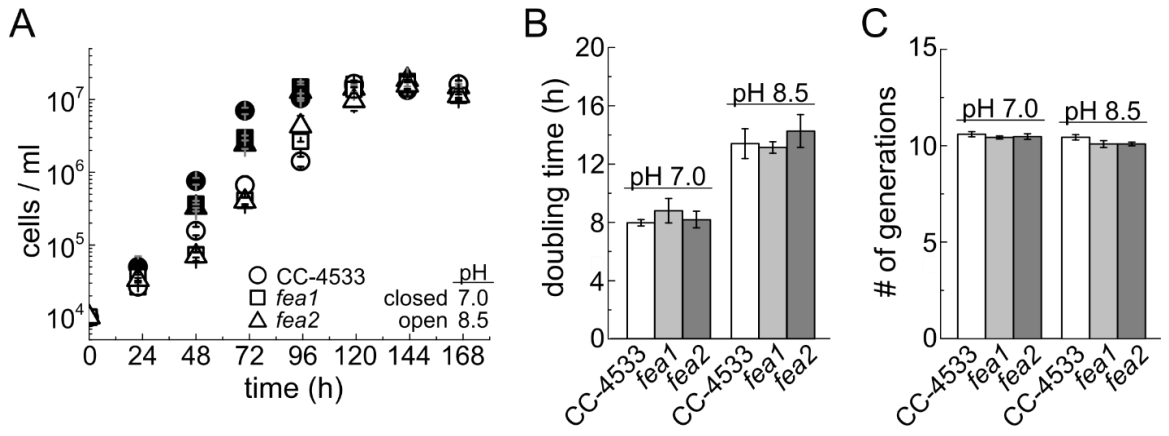

Figure 4.2. Cell growth is not perturbed in the *fea1* or *fea2* mutant strains under excess Fe condition at alkaline or neutral pH. (A) Growth curves of wild-type Chlamydomonas CC-4533 cells and the *fea1* and *fea2* mutant cells grown in 200 μM Fe-containing TAP media at pH 7.0 or pH 8.5. (B) The doubling time and (C) the total number of generations until stationary phase of cells. No significant difference (t-test, $p \leq 0.05$) was found comparing either mutant to the CC-4533 cells. Averages are shown with error bars indicating standard deviation of 3 independent cultures.

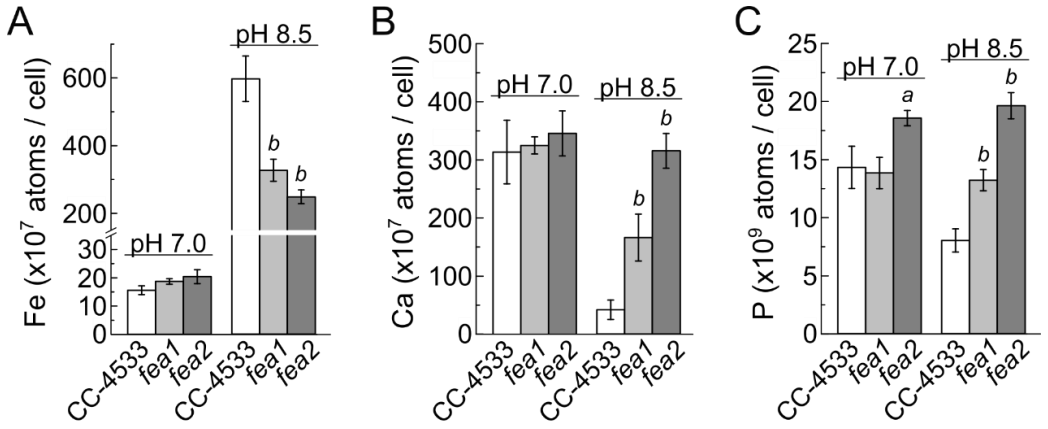

Figure 4.3. Fe accumulation in both the *fea1* and *fea2* strains is significantly reduced under alkaline pH condition. (A-C) Abundances of Fe (A), Ca (B), and P (C) associated with the same cells described in Figure 4.2, as measured by ICP-MS/MS. The cells were collected during mid-log growth (2-4 x 10^6 ells/ml). The corresponding strains and pH of the growth media are as indicated. *a* and *b* represent significant differences (t-test, $p \leq 0.05$) to the wild-type CC-4533 cells in the neutral pH condition (*a*) and in the alkaline pH condition (*b*). Averages are shown with error bars indicating standard deviation of 3 independent cultures.

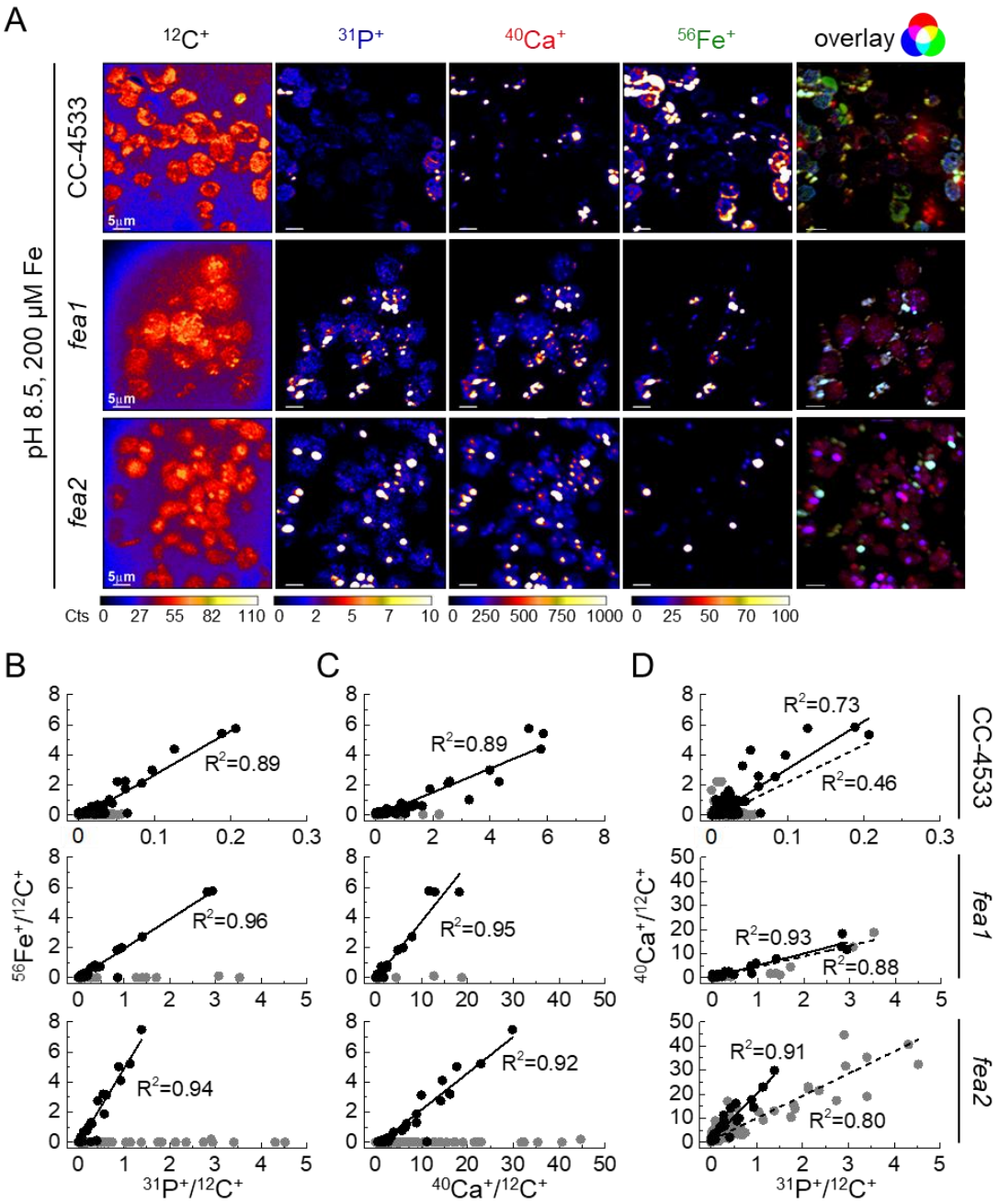

Figure 4.4 Fe accumulated in the *fea* mutant strains under alkaline pH growth colocalizes with Ca and P as in the wild type. (A) NanoSIMS images of cells from the wild-type CC-4533 strain and the *fea1* and *fea2* mutant strains grown in TAP medium with 200 µM Fe at pH 8.5, collected during mid-log growth, and the corresponding overlaid RGB images of the $^{31}P^+$ (blue), $^{40}Ca^+$ (red), and $^{56}Fe^+$ (green) images. Sections of fixed cells were imaged in positive secondary ion mode. Scale bar, 5 µm. (B, C, D) Subcellular correlative quantification of $^{12}C^+$-normalized $^{56}Fe^+$ with $^{31}P^+$ (B) and $^{40}Ca^+$ (C), and of $^{40}Ca^+$ with $^{31}P^+$ (D), from the NanoSIMS imaged cells shown in (A). Each point in the plots corresponds to a non-overlapping ROI generated by an automated algorithm in the analysis software (see Supplementary Figure 12). The black points highlight the ROIs with an $^{56}Fe^+$ count > 2, while the gray points represent all the remaining ROIs. The black lines indicate the linear regression fitting for only the black points; the dash lines indicate the linear regression fitting for all points (black and gray). R^2 values correspond to each linear regression fitting.

4.3.3 Excess Fe in both alkaline pH-grown and stationary-phase cells is bioavailable, but that in stationary-phase cells is more readily accessible.

The bioavailability of excess Fe in cells grown (i) in alkaline condition, and (ii) to different stages of stationary phase was investigated. The experimental setup for the alkaline condition is shown in Figure 4.5A. Briefly, a culture growing in TAP medium at pH 8.5 with excess Fe (200 μM) was sampled for ICP-MS/MS during mid-log growth to assess the amount of Fe accumulated in alkaline condition. These cells were then inoculated into Fe-free media at pH 7.0 or pH 8.5. Before inoculation, the cells were washed with 1 mM EDTA to remove cell surface-associated metals, so as to ensure that no external Fe was carried over from the high Fe medium into the Fe-free media. The cultures in the Fe-free media were monitored for growth and were sampled for ICP-MS/MS after 10 days from the time of inoculation, when growth became stationary.

At stationary phase, the density of the culture in the alkaline medium with excess Fe was ~1 x 10^7 cells/ml (Figure 4.5B), which is the same as that typically observed in cultures grown in standard (neutral pH) conditions (Figure 2.2A). This density appears to be the maximum or saturating culture density in all experiments reported in this dissertation, provided that all cultivation parameters were set as described in Section 2.2.2. Consistent with previous data (Figure 2.4B, Figure 2.5), the cells were doubling approximately every 13 h during log growth phase (Figure 4.5C) and accumulated a great excess of Fe at mid-log growth (~550 x 10^7 atoms per alkaline-pH grown cell, compared to ~15 x 10^7 atoms per neutral pH-grown cell) (Figure 4.5D).

Cell growth was significantly slower upon transfer from the alkaline, Fe-excess medium into Fe-free media at both alkaline and neutral pH; the doubling time of cells was ~33 h in the pH 7.0 culture and ~40 h in the pH 8.5 culture (Figure 4.5C). Nevertheless, regardless of pH conditions, both cultures in Fe-free media eventually reached stationary phase after ~6 generations of cell division, at ~1 x 10^7 cells/ml as observed in the Fe-excess culture (Figure 4.5B).

As Fe limitation inhibits growth (1, 7, 21), and because Fe was not supplied in the Fe-free media, the cells must have utilized the stored Fe that they accumulated from the alkaline, excess

Fe medium to support growth in the Fe-free conditions. Indeed, ICP-MS/MS analysis confirmed the reduction in the Fe content of cells before and 10-days after the medium transfer. Each cell in the Fe-free media retained ~9 x 10^7 Fe atoms at stationary phase (Figure 4.5D). Note that ICP-MS/MS analysis of spent media from the cultures verified that there was no loss of Fe from the cells nor external metal contamination in the Fe-free media (data not shown). As medium Fe was not provided, the Fe quota within these cultures should reduce gradually in proportion to the number of successive generations produced. Thus, in this experiment, the expected Fe quota in cells grown in Fe-free conditions can be derived from the Fe content of cells at the time of inoculation and the number of generations they produced, according to this formula:

$$(Fe\ content\ before\ medium\ transfer)/2^{(\#\ of\ generations)}$$

Using the experimental data presented above, the expected Fe content in cells in stationary phase in the Fe-free media should be $(550 \times 10^7\ atoms/cell)/2^6 = 8.6 \times 10^7\ atoms/cell$, which is in agreement with the experimental value (again, ~9 x 10^7 Fe atoms/cell). The consistency between the quantity of Fe reduced and the number of generations that the cells produced in the Fe-free media showed that intracellular Fe content was mined for cell division. This result thereby indicated that the extra Fe that cells accumulated under alkaline, Fe-excess condition was bioavailable and could be used in face of Fe starvation.

However, the sustained slow growth of cells throughout their growth cycle in the Fe-free media pointed to a slow rate of Fe acquisition from the internal storage site, potentially hinting at some restrictions in accessing the stored Fe. Imaging data from experiments investigating intracellular Fe storages, as presented in Section 3.3.2, suggested that excess Fe accumulated under alkaline condition is likely kept in the acidocalcisome. Altogether, the results suggested that retrieving Fe from acidocalcisomes in Chlamydomonas might involve a slower mechanism than Fe uptake from the growth medium.

With regards to the other elements, cells in Fe-free media continued to accumulate Cu and Zn. Specifically, 10 days after the medium transfer, cellular Cu content increased by ~8-fold

under both neutral and alkaline conditions (Supplementary Figure 13A), and cellular Zn content increased by ~3-fold at neutral pH and ~2-fold at alkaline pH (Supplementary Figure 13B). These levels were similar to those observed in cells transferred from standard, replete conditions to Fe-limitation (data not shown). Cellular contents of Mn, Ca, P, and S did not change significantly before vs. after the transition from the alkaline, Fe-excess medium into Fe-free media.

Finally, previous data showed that when external Fe was supplied in replete or excess amount, an alkaline medium pH impedes growth rate and influences the elemental content of cells (Figure 2.4, Figure 2.5). Yet, interestingly, in Fe-free conditions, a neutral medium pH did not significantly improve the growth rate nor affect the contents of most trace metals, Ca, P, or S, suggesting that access to Fe is the primary growth limiting factor compared to pH conditions.

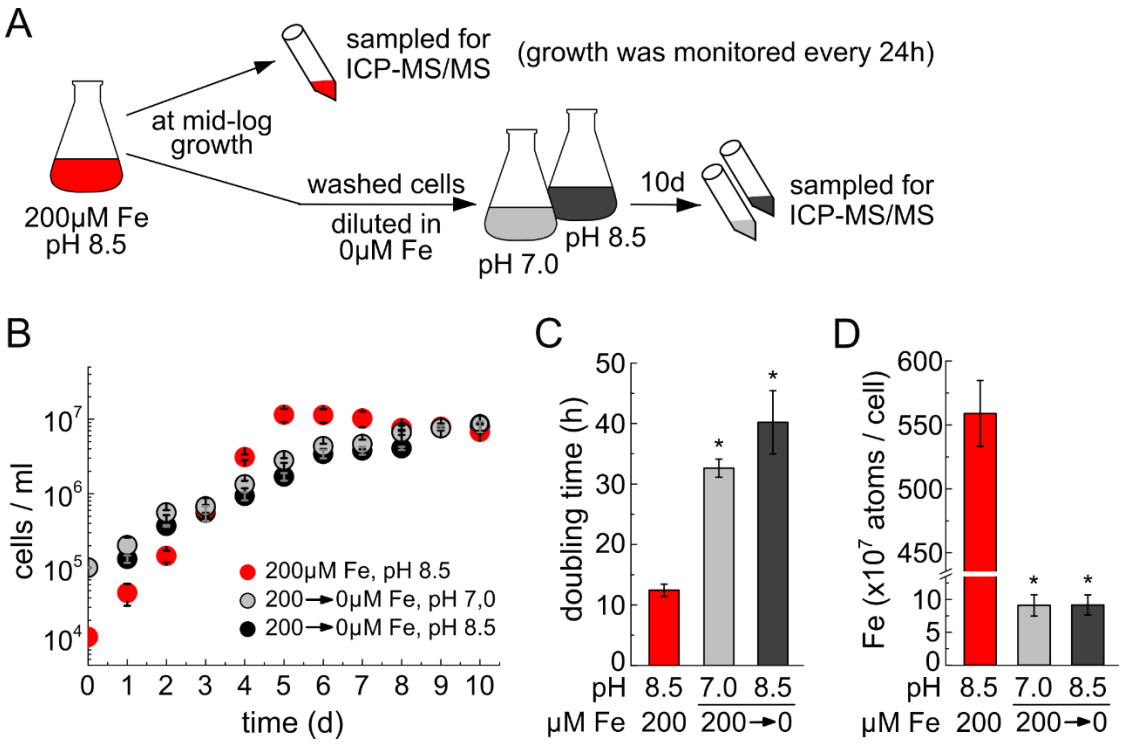

Figure 4.5. Cells grow very slowly upon transfer from alkaline, excess Fe condition into Fe-free condition, but acclimate to the same stationary density as did the Fe-excess culture. (A) Schematic of the experimental setup. CC-4533 cells were inoculated at 1 x 10^4 cell/ml into TAP medium with 200 μM Fe at pH 8.5, sampled for ICP-MS/MS at mid-log growth (2-4 x 10^6 cells/ml), and washed and transferred into Fe-free TAP medium at pH 7.0 or pH 8.5 at 1 x 10^5 cell/ml. Cells from the Fe-free media were sampled for ICP-MS/MS at 10-days post-inoculation. (B) Growth curves and (C) doubling time of cells before (red) and after the medium transfer (light and dark gray). (D) Fe content associated with the cells, as measured by ICP-MS/MS. The corresponding Fe concentration and pH of the growth media are as indicated. Asterisks represent significant differences (t-test, $p \leq 0.05$) to cells before the medium transfer. Averages are shown with error bars indicating standard deviation of 3 independent cultures.

Chlamydomonas cells can also over-accumulate Fe at neutral pH when cells are maintained at stationary phase under Fe luxury condition. Using the same assay, I also investigated the bioavailability of Fe accumulated in cells grown to different stages of stationary phase. The experimental setup is shown in Figure 4.6A. Briefly, 4-day, 7-day, and 10-day old cells growing in TAP medium at neutral pH with excess Fe were sampled for ICP-MS/MS to assess their Fe contents. Separately, the cells were also washed with 1 mM EDTA and resuspended into Fe-free, pH 7.0 TAP medium to 1 x 10^5 cells/ml. Cells in each culture transferred to Fe-free medium were sampled for ICP-MS/MS one week after inoculation, when the cultures had established stationary density.

In agreement with all the data reported thus far (*e.g.* Figure 2.2A-C, Figure 2.4), cells growing with excess Fe at neutral pH doubled every ~8 h until stationary phase and produced ~10 generations of daughter cells, provided that the inoculum density was 1 x 10^4 cells/ml (Figure 4.6B). Also consistent with previous observations (Figure 2.2D), cells accumulated progressively more Fe as they were incubated at stationary phase in the Fe-excess medium (Figure 4.6C). Specifically, the Fe content of a cell collected on day 4 vs. day 7 vs. day 10 post-inoculation increased from 21 x 10^7 to 31 x 10^7 to 53 x 10^7 Fe atoms, respectively. The accumulations of Cu and Zn in cells were also progressive during stationary phase, but not that of Mn, Ca, P, or S (Supplementary Figure S14), as previously noted (Figure 2.2E-I, Supplementary Figure S1).

Upon transitioning into Fe-free medium, the 4-day old Fe-excess inoculum doubled approximately every 17 h and the culture reached stationary phase at ~1.1 x 10^6 cells/ml (produced ~3 generations total). In comparison, the 7-day old inoculum doubled every ~14 h and its culture became stationary at ~1.9 x 10^6 cells/ml (~4 generations); with the 10-day old inoculum, the doubling time was ~12 h and the stationary density was ~2.6 x 10^6 cells/ml (~5 generations) (Figure 4.6D-F). Note that cell growth in all cultures transferred to Fe-free medium halted at

densities far below the typical saturating density (1 x 10^7 cells/ml), indicating that the cells at that point were severely Fe-limited and therefore growth was restricted (1, 7, 21).

Differences in growth aside, all the cultures in Fe-free medium reached stationary phase with a similar amount of cellular Fe, at ~2 x 10^7 Fe atoms/cell (Figure 4.6G). As described earlier, because medium Fe was not provided, the expected Fe quota in cells in the Fe-free condition can be calculated using the Fe content of cells at the time of inoculation and the number of generations of growth observed. So, the expected Fe content in the culture in Fe-free medium inoculated with the 4-day old Fe-excess cells should be $(21 \times 10^7\ atoms/cell)/2^3 = 2.6 \times 10^7\ atoms/cell$; that in the culture inoculated with the 7-day old cells, $(31 \times 10^7\ atoms/cell)/2^4 = 1.9 \times 10^7\ atoms/cell$; and with the 10-day old cells, $(53 \times 10^7\ atoms/cell)/2^5 = 1.7 \times 10^7\ atoms/cell$. These values are consistent with the experimental output (~2 x 10^7 Fe atoms/cell).

In addition to Fe, the cellular content of other elements changed as well after the cells were transferred from Fe-excess into Fe-free medium. In all the cultures without external Fe, Cu was accumulated to ~8 x 10^7 atoms/cell, which was a 2- to 5-fold increase from the various amounts of Cu observed at different stages of stationary phase in the Fe-excess medium (Supplementary Figure S14A). The cellular Zn content before vs. after the transfer was approximately the same (Supplementary Figure S14B), but Mn levels were reduced by ~2.5-fold in all the cultures in Fe-free medium (Supplementary Figure S14C). Significantly, Ca and P contents in cells decreased by over 12-fold and by ~3-fold, respectively, after the transfer to Fe-free medium (Supplementary Figure S14D-E). Cellular S content was also reduced by ~1.7-fold (Supplementary Figure S14F). However, no significant difference was observed between the three sets of cultures in Fe-free medium.

The above data showed three key results: 1) cells accumulated Fe with respect to time during stationary phase (as observed in previous data); 2) the more Fe that cells accumulated from an Fe-excess, neutral pH medium, the faster they grew subsequently and the more biomass they produced upon transitioning into an Fe-free medium; and 3) regardless of the quantity of Fe

accumulation prior to the medium transfer, the Fe content per cell at stationary phase in all cultures transferred to Fe-free medium was reduced to ~2 x 10^7 atoms, indicative of the minimal Fe quota in these conditions. Altogether, the outcome suggested that in face of Fe starvation, cells exploited the surplus Fe that they acquired during stationary phase under excess Fe condition to optimize growth until the minimal Fe quota was reached. In other words, the excess Fe accumulated during stationary phase was bioavailable, and it offered a growth advantage to the cells for subsequent Fe limitation.

Depending on the magnitude of their Fe contents, the cells in the cultures transferred into Fe-free medium in this experiment doubled every ~12 to 17 h. This range of doubling times is almost twice as fast compared to that of the cells that were transferred from alkaline, Fe-excess medium into Fe-free medium (~33 to 40 h, Figure 4.5C). The faster growth rate suggested that the Fe accumulated by cells during stationary phase under excess Fe condition (at neutral pH) was more readily accessible than the Fe that cells accumulated under alkaline condition. Previous imaging data suggested different storage sites for Fe stored under the two conditions: While the Fe overloaded into cells under alkaline condition is likely sequestered into acidocalcisomes, the Fe accumulated during stationary phase is likely stored outside of the acidocalcisome (see Section 3.3 for data and discussion). Thus, it appears that the acidocalcisome might be a less accessible storage site for Fe compared to the alternative accumulation site where excess Fe in stationary-phase cells is kept.

It was not surprising to find that excess Fe in Chlamydomonas cells is bioavailable in face of Fe limitation, whether the Fe might be stored in the acidocalcisome or other sites. Studies have shown that Fe is mobilized from vacuoles to support growth in both yeast and plants, especially during Fe deficiency (99, 251–254). Similarly, Fe is also released from plant ferritins during growth of seedlings and greening of plastids (29, 253, 255). However, it was unexpected to observe that the accessibility of intracellular Fe might significantly vary depending on the storage location. The extent of accessibility might relate to the rate of Fe export from the different storage sites.

Moreover, either Fe^{2+} or Fe^{3+} might be present in vacuoles (221, 223, 224), whereas ferritins bind only Fe^{3+} (29, 222). It is possible that the different species of stored Fe also contribute to the varied accessibility of Fe supplies.

Beside Fe, changes in the cellular contents of other elements upon the transition from Fe-excess to Fe-free conditions was also noted. First, cells accumulated Cu substantially in all Fe-free media, whether the cells were transitioning from stationary phase or alkaline condition. The higher uptake of Cu might be an indication for an increased demand in cells to synthesize Cu-dependent high-affinity Fe uptake components, such as the multicopper ferroxidase FOX1 (22, 70). Secondly, the virtually equivalent amounts of Zn in cells before vs. after the medium transfer suggested that Zn accumulation was not impacted by the change in Fe nutrition, showing that the transport of Fe vs. Zn might be selective. Third, Ca and P levels decreased dramatically during re-mobilization of stored Fe. Most of the intracellular Ca and a large amount of P, in the form of polyP, are found in Chlamydomonas (63). Therefore, a reduction in Ca and P might indicate degradation of acidocalcisomes in the cells. Lastly, note that there was generally no significant difference in the elemental contents among the cultures in Fe-free medium inoculated from 4-day vs. 7-day vs. 10-day old Fe-excess cells. This suggested that the duration that the cells had spent in the Fe-excess medium, and by association, the amounts of Fe and other elements that they had accumulated before the transfer to fresh Fe-free medium, were unlikely the primary factors that led to the observed changes in the contents of Cu, Mn, Ca, P, and S in cells. Rather, these changes were most likely a result of the metabolic switch from Fe-luxury to Fe-limiting condition.

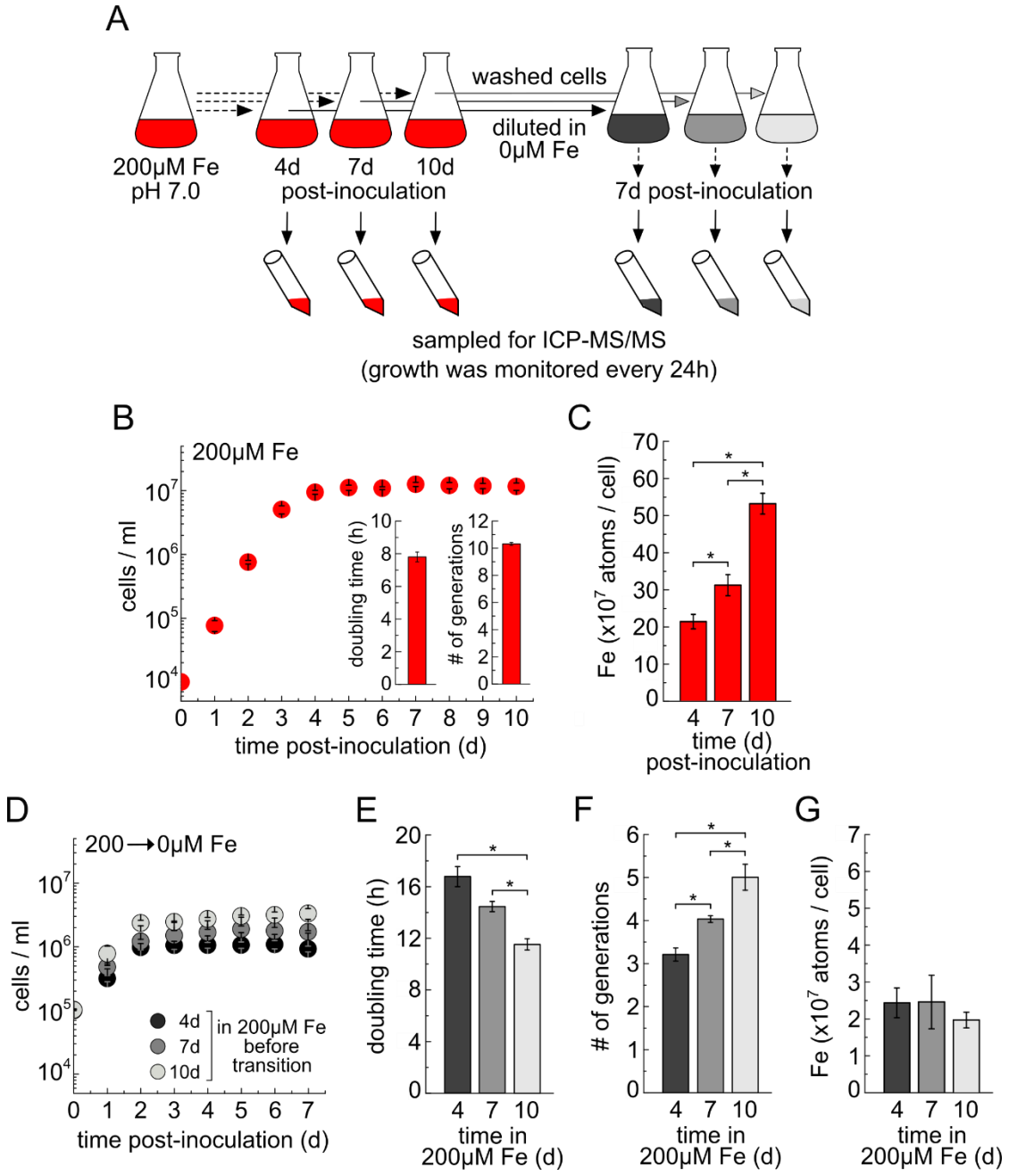

Figure 4.6 Cells with greater Fe accumulation in stationary phase grow faster and produce greater number of generations upon transfer into Fe-free medium. (A) Schematic of the experimental setup. CC-4533 cells were inoculated at 1 x 10^4 cell/ml into TAP medium with 200 μM Fe at pH 7.0. At 4-, 7-, and 10-days, cells were collected for ICP-MS/MS and were washed and transferred into Fe-free, pH 7.0 TAP medium at 1 x 10^5 cell/ml. Cells from the cultures transferred into Fe-free medium were collected for ICP-MS/MS at 7-days post-inoculation. (B, D) Growth curves before (B) and after the medium transfer (D). Insets of (B) show the doubling time and the number of generations until stationary phase of cells before the medium transfer. (C, G) Abundance of Fe associated with cells before (C) and after the medium transfer (G), as measured by ICP-MS/MS. (E) Doubling time and (F) number of generation until stationary phase of cells after the medium transfer. Asterisks represent significant differences (t-test, $p \leq 0.05$) between the bracketed data points. Averages are shown with error bars indicating standard deviation of 3 independent cultures.

4.3.4 The mutant lacking ferritin1 over-accumulates more Fe than does the wild-type strain under excess Fe condition, but fails to benefit from stored Fe during subsequent limitation.

As shown in the preceding section, excess Fe accumulated by cells in stationary phase is bioavailable and is readily accessible in subsequent periods of Fe starvation. The outcome of the experiment revealed that the longer that cells are incubated in stationary phase, they more Fe they accumulate, the better they can grow (in terms of growth rate and number of generations) in Fe limitation. This experimental setup provided an excellent platform to test different candidate components for involvement in the mobilization and distribution of excess Fe. Three groups of mutant strains, in addition to the wild-type background strain CC-4533, were acquired and tested: i) *fea1*, *fea2*, and *fre1*, which are affected in high-affinity Fe uptake; ii) *cvl1*, *cvl2*, *nramp1*, and *nramp4*, in which the corresponding gene products are homologs to Fe-distributing proteins in Arabidopsis and yeast (46, 80), and iii) *vtc1*, *v-ppase*, and *fer1*, which are defective in functions of proteins associated with Fe storage. Briefly, cells from each strain growing in TAP medium at neutral pH with excess Fe (200 μM) were sampled for ICP-MS/MS on day 3, 4, 7, 10, and 14 post-inoculation. Each sampling day corresponded to the log, early stationary, stationary, late stationary, and prolonged stationary phase of the culture. At 10-days post-inoculation, the cells were washed and resuspended into Fe-free, pH 7.0 TAP medium and sampled for ICP-MS/MS one week later, when the cells had established stationary phase. The growth and elemental composition of cells under both excess Fe condition and upon their transition into Fe-free medium were compared between the wild-type vs. the mutant strains.

Under excess Fe condition, the mutant strains with loss of function of an Fe uptake protein or an Fe storage-related protein (*fea1*, *fea2*, *fre1*, *vtc1*, *v-ppase*, and *fer1*) generally grew slower compared to the wild-type strain, with a doubling time at ~11 to 13 h vs. ~8 h, although the differences are mostly insignificant (Figure 4.7A). The mutants hypothetically defective in

intracellular Fe transport (*cvl1*, *cvl2*, *nramp1*, and *nramp4*) doubled every ~8 h, same as the wild type. All strains produced the same number of generations in Fe-excess medium (Figure 4.7B).

ICP-MS/MS analysis revealed that the S content in most of the mutants was similar to that in the wild type under excess Fe condition, except in the *nramp4*, *fer1*, and v-*ppase* strains (Supplementary Figure 15D). Compared to the wild type, the S content in the *nramp4* strain was significantly lower, while that in the *fer1* strain was higher. The S content in the *v-ppase* mutant was 1.6-fold greater than the wild type during log phase, but in stationary phase, it was reduced back to similar levels as in the wild type. Due to these variations between samples, the ICP-MS/MS data for other elements in this analysis were normalized to cell number instead of S.

Just as observed in the wild type, most mutants accumulated progressively more Fe as they grew from log to stationary phase and also during stationary phase under excess Fe condition (Figure 4.8A). However, the absolute amount of accumulated Fe varied among the different strains, especially upon extended incubation at stationary phase (10 days or longer post-inoculation). Distinctively, the *fer1* strain accumulated almost twice as much Fe than did the wild type at late and prolonged stationary phase (10- and 14-day post inoculation). In contrast, the *vtc1* strain consistently accumulated less Fe than did the wild type throughout stationary phase. Specifically, the *vtc1* mutant virtually stopped accumulating Fe at 10-days after inoculation, and at 14-days post-inoculation, its Fe content was only about half of the amount in the wild type. Other mutant strains, including *fre1*, both of the *fea*, and both of the *cvl*, accumulated just slightly but significantly less Fe than did the wild type at prolonged stationary phase; the reduction ranged from 1.2- to 1.5-fold.

The contents of other trace metals were also compared between the wild type and the mutant strains. Generally, most mutants accumulated Cu and Zn progressively as did the wild type, but the amounts of metal accumulations varied. Most significantly, compared to the wild type at 14-days after inoculation, the *fre1*, *nramp4*, and *vtc1* strains accumulated ~2-fold less Cu, while the *cvl1*, *cvl2*, *nramp1*, and *v-ppase* strains over-accumulated Cu by up to ~1.5-fold

(Supplementary Figure 15A). In the *fre1* mutant, the reduction in its Cu content was the most significant phenotype relative to other changes in its elemental composition. The Zn content increased significantly by ~1.3-fold in the *cvl1* and *nramp1* strains compared to the wild type at prolonged stationary phase, whereas in the *nramp4* strain, Zn was reduced by ~1.5-fold (Supplementary Figure 15B). The *vtc1* strain accumulated ~2-fold less Zn than did the wild type at log and early stationary phase, but reached a similar Zn content by prolonged stationary phase. No major difference was observed in Mn content between the wild type and any of the mutant strains, except those associated with Fe storage (*vtc1*, *v-ppase*, and *fer1*) (Supplementary Figure 15C). In particular, the *vtc1* strain accumulated ~1.5-fold less Mn than did the wild type throughout the experimental time course. Note that the *vtc1* strain is also the only tested mutant that was significantly affected in the accumulation of all trace metals, Ca, and P.

Accumulation of Ca and P in the wild-type vs. mutant strains were assessed as well. Consistent with previous studies (62, 63), the *vtc1* strain was defective in Ca and P accumulations. At 14-days post-inoculation, the Ca and P levels in the *vtc1* mutant were ~10-fold and ~2-fold lower than in the wild type, respectively (Figure 4.8B-C). Note that cellular Ca is mostly associated with the acidocalcisome, which is abnormal in the *vtc1* mutant. In contrast, cellular P is present in large amount both inside and outside of the acidocalcisome, such as in DNA, RNA, and different metabolites. Thus, the more dramatic reduction in Ca compared to P was expected in the *vtc1* mutant. The *v-ppase* and *fer1* mutants accumulated slightly but significantly less Ca and P compared to the wild type at different stages of stationary phase. Other mutants maintained a Ca content similar to that in the wild type (Figure 4.8B), but their P contents varied from log to late stationary phase (Figure 4.8C). An exception is the *fea2* strain, which accumulated a significantly greater amount of P than did the wild type at log and throughout the different stages of stationary phase (up to ~1.5-fold).

The outcome that the *fer1* strain over-accumulated significantly more Fe than did the wild type throughout stationary phase suggested that the loss of function of the FER1 protein triggered

increased Fe uptake. A potential reason might be that FER1 acts as a modulator for Fe acquisition, based on the amount of Fe stored within the protein. In an Arabidopsis mutant lacking three of its four ferritin isoforms, Fe is also over-accumulated relative to the wild-type plant and is observed in the plastids and cell walls of the leaves (256). It is unclear where the additional Fe might be kept in the Chlamydomonas *fer1* mutant. Ferritin is hypothesized to be a candidate storage site for Fe accumulated during stationary phase in wild-type cells, as opposed to acidocalcisomes (see Section 3.3.1). However, it is possible that the acidocalcisome could take over storage function in the absence of ferritin. The Fe might also be bound to other proteins or metabolites in the plastids, and/or sequestered in the periplasmic space as observed in Arabidopsis.

In this context, it is also interesting to note from data presented in the previous chapter that in the wild-type strain, the abundance of FER1 was reduced, while the cellular Fe content increased during stationary phase (Figure 3.4, Figure 2.2D, Figure 4.6C). In comparison, as shown above, the *fer1* strain, which lacks FER1, accumulated an even greater amount of Fe during stationary phase than did the wild type. Furthermore, Long et al. previously reported a decrease in the abundance of FER1 in cells as medium Fe concentration increased (36). The results altogether documented a negative correlation between the abundance of FER1 and cellular Fe content.

In contrast to the *fer1* strain, the *vtc1* strain showed a significant reduction in Fe accumulation, especially from late stationary phase and beyond. The *vtc1* mutation cripples both polyP synthesis and the accumulation of Ca and polyP in the acidocalcisome (54, 62, 63, 69). The mutation does not preclude the formation of acidocalcisomes in the cells (62, 63), but it does disrupt the organelle's biochemistry and functions, such as metal sequestration (62, 257). Yet, previous data showed that in the wild-type strain, acidocalcisomes are unlikely to be a major storage site for Fe accumulated during stationary phase (Section 3.3.1). Furthermore, Schmollinger et al. demonstrated by X-ray fluorescence microscopy the presence of Fe foci in acidocalcisomes in the *vtc1* strain just as in the wild type, when the cells were transiently

overloaded with Fe (63). The data suggested that Fe sequestration into the acidocalcisome is operational in the absence of VTC1. Therefore, the reduction in Fe accumulation observed in the *vtc1* mutant at stationary phase might not relate to issues specifically in the sequestration of Fe into the acidocalcisome. Perhaps the formation of defective acidocalcisomes generally perturbs metal accumulation, potentially due to the lack of polyP in the organelle. Klompmaker et al. proposed that polyP in vacuoles and acidocalcisomes is required for proper metal accumulation, as polyP-deficient yeast cells show growth defects under low metal availability and are defective in Mg^{2+} uptake (257).

Beside the *fer1* and *vtc1* strains, all other tested mutants were generally able to accumulate a similar quantity of Fe as did the wild type. The differences in the growth rate among the mutants and the wild type might have contributed to the minor differences observed. This result indicated that each of the proteins encoded by these affected genes alone was unlikely to be the sole predominant component responsible for Fe uptake during stationary phase. Nonetheless, FEA1, FEA2, FRE1, CVL1, and CVL2 might each be partially involved in Fe accumulation in Chlamydomonas under excess Fe condition, given that the Fe contents in the corresponding mutant strains were all slightly but significantly reduced upon extended incubation at stationary phase.

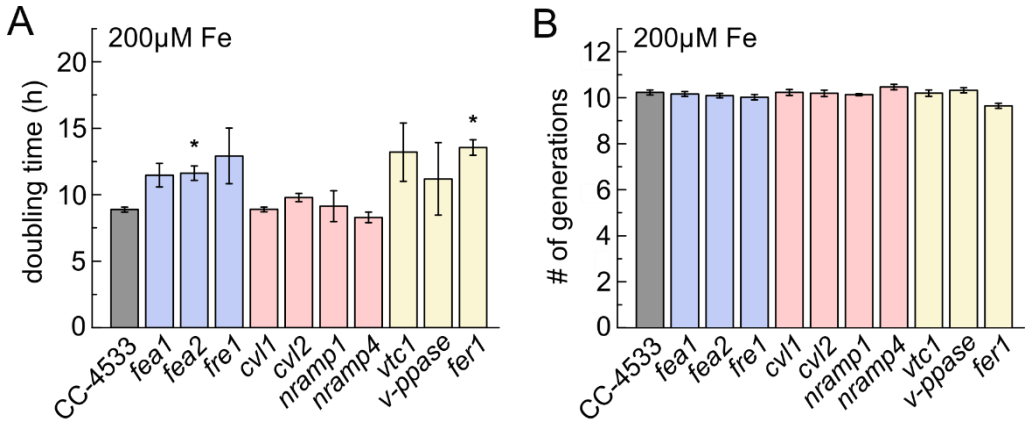

Figure 4.7. All tested mutant strains grow similarly as the wild-type strain under excess Fe condition. (A) Doubling time and (B) number of generations until stationary phase of cells in the wild-type CC-4533 strain (gray) and in the indicated insertional mutant strains (blue, affected in Fe uptake; pink, hypothetically affected in Fe distribution; yellow, affected in Fe storage). All strains were grown in TAP medium containing 200 µM Fe (pH 7.0). Asterisks represent significant differences (t-test, $p \leq 0.01$, multiple Bonferroni-corrected) to the CC-4533 cells. Averages are shown with error bars indicating standard deviation of 3 independent cultures.

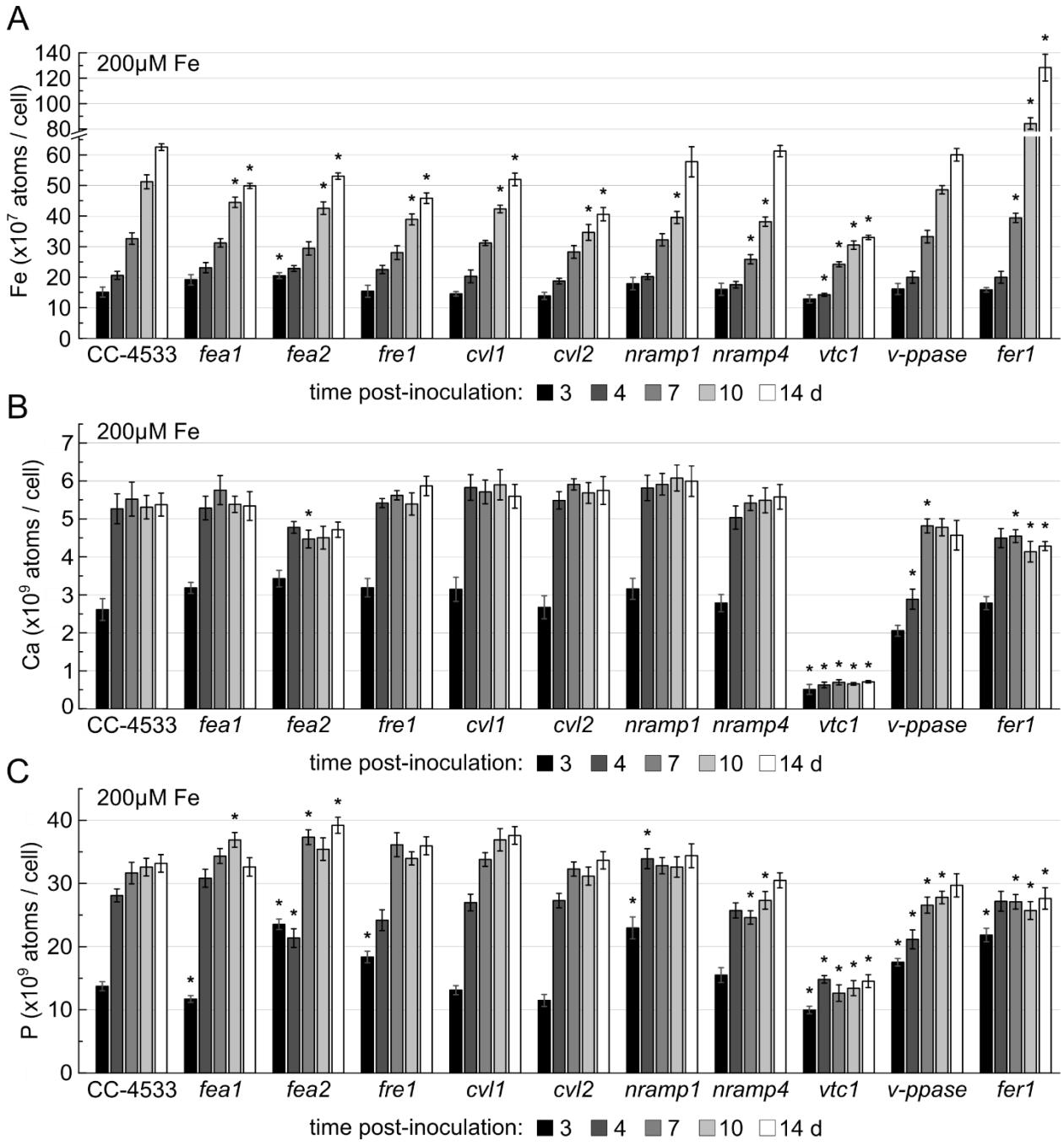

Figure 4.8. The *fer1* mutant strain accumulates Fe significantly more than does the wild type during stationary phase. (A-C) Abundances of Fe (A), Ca (B), and P (C) associated with the same cells described in Figure 4.7, as measured by ICP-MS/MS. The corresponding strains are as indicated. The cells were collected on day 3 (mid-log phase), 4 (early stationary), 7 (stationary), 10 (late stationary), and 14 (prolonged stationary) post-inoculation. Asterisks represent significant differences (t-test, $p \leq 0.01$, multiple Bonferroni-corrected) to the wild-type CC-4533 cells at each time point. Averages are shown with error bars indicating standard deviation of 3 independent cultures.

In the second part of the experiment, cells of the wild type and each of the mutant strains were transferred into Fe-free medium after a 10-day incubation in Fe-excess medium. All mutant strains grew significantly more slowly relative to the wild type upon transfer; the doubling time of the wild type was ~13 h, whereas that of the mutants ranged from ~25 to ~32 h (Figure 4.9A). The number of generations produced by the wild type, the *cvl1*, *nramp1*, *nramp4*, and *v-ppase* mutants were comparable under Fe-free condition (Figure 4.9B, Table 2). The *fea1*, *fea2*, *fre1*, *cvl2*, *vtc1*, and *fer1* strains produced ~0.6 to ~0.9 generation fewer than the wild type. The stationary density of the wild type, Fe-free culture was ~2.3 x 10^6 cells/ml; that among the mutant cultures ranged between ~1.6 and ~2.0 x 10^6 cells/ml.

Interestingly, chlorosis (measured at one-week after the medium transfer) at three distinctive levels was observed among the three groups of mutants (Figure 4.9C). Relative to the wild-type strain, the chlorophyll content in the mutants affected in Fe uptake (*fea1*, *fea2*, and *fre1*) decreased by 3-fold or more; that in the mutants affected in Fe storage (*vtc1*, *v-ppase*, and *fer1*) was reduced by ~1.5- to 2-fold; and in the mutants that are potentially defective in Fe distribution (*cvl1*, *cvl2*, *nramp1*, and *nramp4*), the chlorophyll content was approximately the same as in the wild type.

ICP-MS/MS analysis revealed differences in the elemental contents of cells before and one week after the transition from Fe-excess to Fe-free medium. Data showed that S accumulation was generally similar between the wild type and the mutants before the medium transfer, but significant differences were noted after the transfer (Supplementary Figure S16D). Many mutant strains, including *fea*, *cvl*, *nramp*, *v-ppase*, and *fer1*, accumulated more S than did the wild type in the Fe-free medium. This hinted that the biomass per cell in these strains might be greater than that in the wild type under Fe-free condition, considering that S content linearly correlated with biomass in the wild type when Fe is abundant (Supplementary Figure S2). Given these variations, the other ICP-MS/MS data were normalized to cell numbers in this analysis.

In all tested strains, the differences in their Fe contents before vs. after the medium transfer were consistent with the amount of biomass they produced in the Fe-free medium (in terms of number of generations) (Figure 4.10A). This was verified through comparing the ICP-MS/MS data for Fe contents to the calculated theoretical Fe quota of cells in the Fe-free cultures (Table 2). As did the wild type, most mutants reached stationary phase in the Fe-free medium at ~2 x 10^7 Fe atoms/cells, which has been determined as the minimal Fe quota for Chlamydomonas growing in TAP medium (see Section 4.3.3 and Figure 4.6). A distinctive exception is the *fer1* mutant, which accumulated about twice as much Fe than did the wild type before the medium transfer, and retained an Fe content ~3-fold greater than the minimal quota after the transfer. The Fe content in the *fea2* strain was also higher than that of the wild type in the Fe-free medium, but only by ~1.5-fold, and its Fe content prior to the medium transfer was slightly lower compared to the wild type (~1.2-fold difference). In line with the relatively small reduction in its Fe content, the *fea2* mutant also produced the least amount of biomass compared to the other strains upon transition into Fe-free condition.

As in the wild type, Cu accumulation increased in most mutants upon transfer from Fe-excess to Fe-free medium, although the extent of the increase varied (Supplementary Figure S16A). The *fea1*, *fea2*, *cvl1*, *v-ppase*, and *fer1* strains, as did the wild type, accumulated ~2-fold more Cu. The *cvl2* and the *nramp1* mutants accumulated ~2.8- and to ~2.5-fold more Cu, respectively. The *fre1* and *vtc1* mutants failed to accumulate Cu in the Fe-free medium; their Cu contents were maintained at similar quantities before vs. after the medium transfer. Notably, both mutants had already accumulated significantly less Cu than did the wild type in Fe-excess medium (by ~1.3 to 2-fold). In the *nramp4* strain, Cu accumulation increased by ~2.5-fold upon the medium transfer, but its Cu content both before and after the transfer was significantly less than that in the wild type by ~2-fold. The cellular Zn content before vs. after the medium transfer was unchanged in both the wild type and most mutant strains (Supplementary Figure S16B). Only in the *fea1*, *fea2*, *cvl2*, and *nramp4* strains were small but significant increases in Zn accumulation

observed. As for Mn, the accumulations between the wild type and the mutants were all very similar; all strains exhibited a ~2-fold reduction after the medium transfer (Supplementary Figure S16C).

All tested strains showed a substantial reduction in their Ca and P contents upon the transfer from Fe-excess to Fe-free medium, but again, to different extents (Figure 4.10B-C). In the wild type, the decrease in Ca before vs. after the medium transfer was ~15-fold (Figure 4.10B). The *fea1*, *fea2*, *fre1*, and *fer1* strains showed a relatively smaller reduction, while a greater decrease was noted in the *nramp4* strain. Ca content in the *vtc1* strain was already ~8-fold lower than that in the wild type before the medium transfer, and it was reduced even further after the transfer (~1.8-fold compared to the wild type and similar to the amount observed in the *nramp4* strain post-transfer).

All mutants except the *vtc1* strain showed a reduction in their P contents upon transfer to Fe-free medium from the Fe-luxury situation (Figure 4.10C). In the *vtc1* mutant, P accumulation before vs. after the medium transfer was maintained at a similarly low level that is comparable to the quantity observed in the wild type post-medium transfer. In the other mutants, a lesser reduction in P compared to that in the wild type was observed (~1.7- to ~2.5-fold among the mutants vs. ~3-fold in the wild type). Note that generally, there were significant differences between the wild type and the mutants in their P contents both before and after the medium transfer, which together contributed to variabilities in the extent of P reduction observed among the tested strains.

In most of the tested mutant strains, cell growth stopped in the Fe-free cultures when their Fe contents were reduced to ~2 x 10^7 atoms/cell, *i.e.* the minimal Fe quota for the CC-4533 wild-type Chlamydomonas strain. This indicated that in face of Fe starvation, these mutants, as did the wild type, maximized biomass production by draining their internal Fe supply accumulated during stationary phase under Fe-excess condition. In other words, the affected gene products in these mutants did not impede the cells' ability to distribute and use their stored Fe during Fe

limitation. The well-matched theoretical vs. experimental values of Fe quota in cells in the Fe-free cultures suggested that there was no issue in the allocation of Fe from mother to daughter cells during cell division, nor in the usage of the Fe (*e.g.* for synthesizing new Fe proteins). Moreover, the comparable numbers of generations produced by the wild type vs. the mutants implied that none of the mutations substantially inhibited growth. However, the similarly slower growth of all the mutants in the Fe-free medium compared to the wild type might be an indication of some common disruptions in Fe homeostasis, potentially in the transport of intracellular Fe to its destinations for utilization.

The *fer1* mutant exhibited curious phenotypes both before and after transition from Fe-excess to Fe-free conditions. It accumulated more Fe in Fe-luxury condition than did the wild type and other mutants. Supposedly, this greater supply of intracellular Fe should confer the *fer1* cells a growth advantage that other strains lack in face of Fe starvation. However, the *fer1* mutant did not grow faster nor produce more biomass than the other mutants upon the medium transfer. On the contrary, it has the second slowest growth rate and produced the second fewest generations in the Fe-free medium. Furthermore, the *fer1* mutant in the Fe-free culture retained 2-3-fold more Fe than did all other tested strains, including the wild type, indicating that its growth arrest was not due to a general lack of Fe. Taken together, the loss of function of the FER1 protein appears to 1) lead to an increase in Fe accumulation in Fe-excess condition, and 2) render a portion of the intracellular Fe un-usable in subsequent Fe limitation, which restricted growth. As previously mentioned, in Arabidopsis grown on excess Fe, the loss of ferritins likewise results in a substantial over-accumulation of Fe in the leaves, specifically in the plastids and in the cell wall (256). Accordingly, FER1 might function in facilitating both Fe uptake and distribution, and potentially has a role in signaling in response to changes in Fe nutrition. In addition, the strong accumulation of Fe in the cell wall of the Arabidopsis *fer* mutant might hint to increased Fe efflux. If excess Fe in the Chlamydomonas *fer1* strain is similarly localized to the periplasmic space for export, such an Fe pool might be more difficult to access in times of need. This might explain why a fraction of

the accumulated Fe in the *fer1* strain was not available for cell use under Fe-free condition. Alternatively, the observed Fe distribution issue might relate to the role of FER1 in Chlamydomonas as an Fe buffer that holds Fe temporarily during intracellular transport.

Meanwhile, it was interesting to observe that the extent of chlorosis in the mutants under Fe-free condition could be used to categorize the functions of the affected proteins. The results suggested that under Fe limitation, the loss of function of a high-affinity Fe uptake protein might hinder chlorophyll production more so than the loss of function of a component affecting Fe storage. In contrast, the loss of functions of CVL1, CVL2, NRAMP1, and NRAMP4, which might be involved in Fe distribution, did not appear to induce chlorosis. The phenotypes might relate to issues in the delivery of Fe to the site of chlorophyll biosynthesis in the chloroplasts.

Furthermore, the substantial reduction in both Ca and P contents in all tested strains under Fe-free condition suggested that Fe limitation might induce degradation of acidocalcisomes, considering that about half of intracellular P and most of the Ca are found in acidocalcisomes (63). In relation, the *vtc1* mutant, which is defective in Ca and P accumulations, retained a similar quantity of Ca and P as in the wild type and most other mutants in the Fe-free medium. This level of Ca and P might reflect the minimal Ca and P quota required by cells under Fe limitation.

Beside Ca and P, the *vtc1* mutation also restricts accumulation of Fe, Cu, and Mn, as shown by the present data. The effect of *vtc1* on Mn accumulation has been reported in Tsednee et al. as well (62). In wild-type yeast cells, Mg^{2+} is acquired by endocytosis, accumulated into polyP-filled vacuoles, and exported back into the cytosol subsequently for utilization (257). PolyP-deficient yeast cells, however, are sensitive to low metal availability and defective in Mg^{2+} uptake (257). These results indicated that defective acidocalcisomes, as observed in the *vtc1* strain, might generally affect metal uptake, possibly because of impaired metal transport into and out of the organelle due to the lack of polyP.

Separately, while the FRE1 protein is known as an Fe uptake component, its loss inhibited Cu accumulation in cells under both Fe-excess and Fe-limiting conditions, suggesting that it is

also associated with Cu uptake in Chlamydomonas. In line with this inference, FRE1 in yeast has been shown to involve in high-affinity transport of both Cu and Fe (258, 259). In the opposite direction, the *cvl2* and *nramp1* mutants over-accumulated Cu in both Fe-excess and Fe-free media. This suggested that the CVL2 and NRAMP1 proteins might play a role in preventing Cu overload in cells and/or in Cu efflux, potentially from acidocalcisomes, in addition to their hypothesized functions in Fe transport. Altogether, these results implicated an intertwined network between Fe and Cu homeostasis in Chlamydomonas.

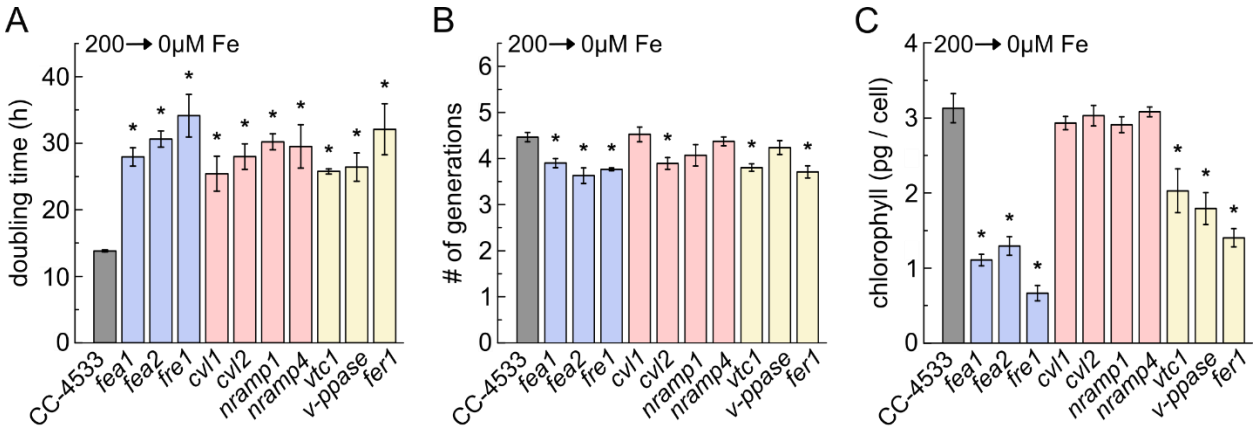

Figure 4.9. Upon transfer from Fe-excess to Fe-free medium, the tested mutants exhibit different levels of chlorosis based on the function of their affected gene product. 10-day old cells of the wild-type CC-4533 and the indicated mutant strains, grown in 200 μM Fe-containing TAP medium (pH 7.0), were washed and transferred into Fe-free TAP medium (pH 7.0) at 1 x 10^5 cells/ml. Cell growth in the Fe-free cultures were monitored for 7 days. (A) Doubling time and (B) number of generations until stationary phase of cells upon the medium transfer. (C) Chlorophyll content of cells at stationary phase, measured at 7-days post-medium transfer. The gray bars represent CC-4533; blue, mutants affected in Fe uptake; pink, mutants hypothetically affected in Fe distribution; and yellow, mutants affected in Fe storage. Asterisks indicate significant differences (t-test, $p \leq 0.01$, multiple Bonferroni-corrected) to the CC-4533 cells. Averages are shown with error bars indicating standard deviation of 3 independent cultures.

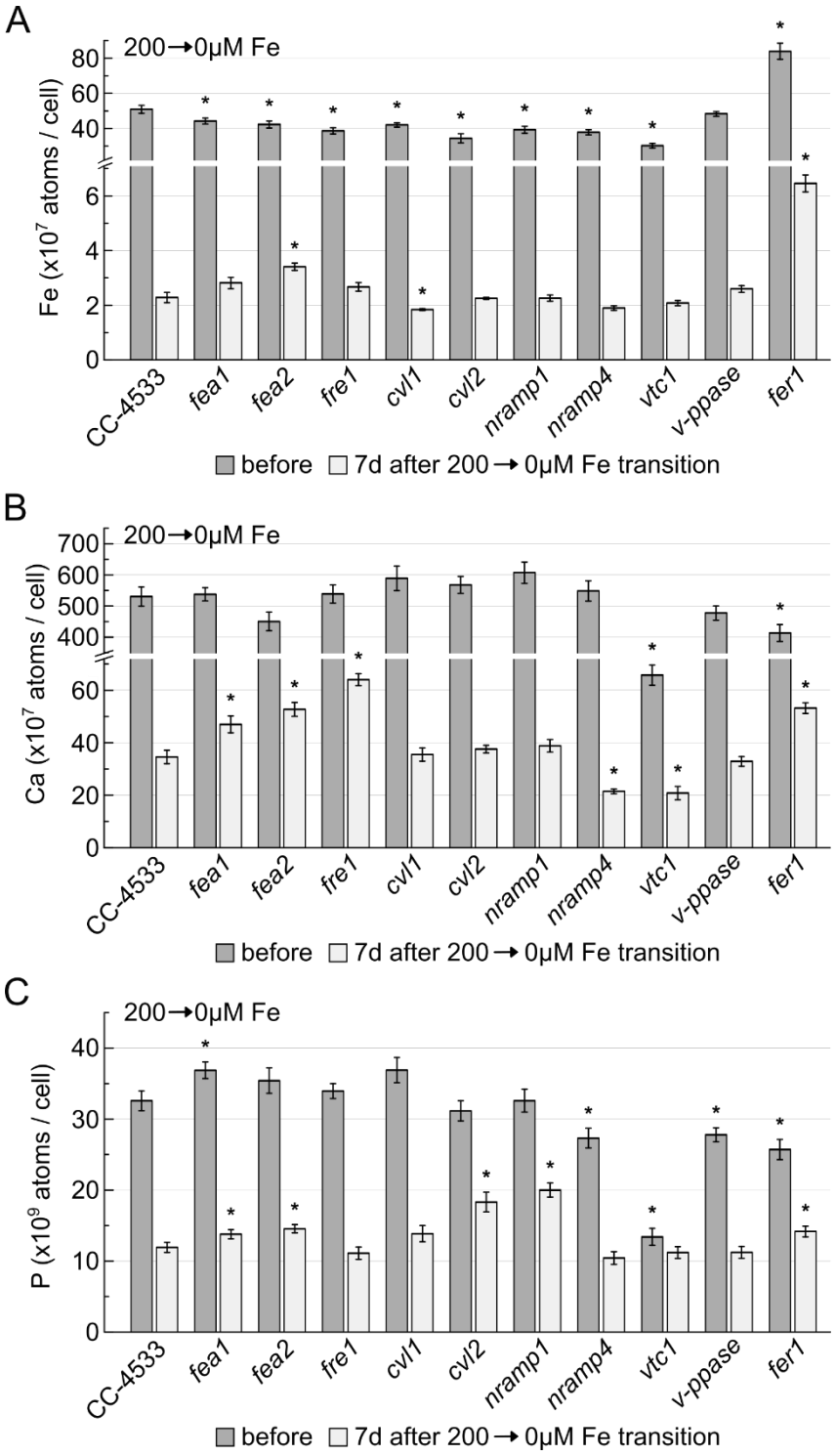

Figure 4.10. Upon transfer from Fe-excess into Fe-free medium, the *fer1* mutant strain does not reach stationary phase at the minimal Fe quota as do the wild type and other mutants. (A-C) Contents of Fe (A), Ca (B), and P (C) associated with the same cells described in Figure 4.9 before (dark gray) and 7 days after the medium transfer (light gray), as measured by ICP-MS/MS. The corresponding strains are as indicated. Asterisks represent significant differences (t-test, $p \leq 0.01$, multiple Bonferroni-corrected) between the wild-type CC-4533 cells and each mutant at the equivalent time points. Averages are shown with error bars indicating standard deviation of 3 independent cultures.

Table 2. Comparison of experimental vs. theoretical values of Fe quota in cells upon transfer from Fe-excess to Fe-free medium

		Fe (x 10^7 atoms / cell)			
			After Transfer		
Strain	**Number of Generations**	**Before Transfer**	**Experimental**	**Theoretical**	**% Difference**
CC-4533	4.5	51	2.3	2.3	1.2
fea1	3.9	45	2.8	3.0	5.1
fea2	3.6	43	3.4	3.4	0.3
fre1	3.8	39	2.7	2.9	6.1
cvl1	4.5	42	1.9	1.8	0.7
cvl2	3.9	35	2.3	2.3	2.8
nramp1	4.1	40	2.3	2.4	3.5
nramp4	4.4	38	1.9	1.8	3.5
vtc1	3.8	31	2.1	2.2	4.2
v-ppase	4.2	49	2.6	2.6	1.3
fer1	3.7	84	6.5	6.4	0.9

The numbers of generations in the Fe-free medium are as shown in Figure 4.9B, calculated as shown in Section 2.2.4.
The experimental values of cellular Fe content before and after the medium transition were obtained by ICP-MS/MS analysis. Averages of 3 independent cultures are shown, as in Figure 4.10A.
The theoretical Fe quota is calculated by $(Fe\ content\ before\ medium\ transfer)/2^{(\#\ of\ generations)}$.

4.3.5 Conclusions

The sequestration and mobilization of excess Fe in Chlamydomonas are complex processes and do not rely on a single predominant component. Nevertheless, two Fe proteins in particular have been distinguished for their roles in Fe transport through experiments reported in this chapter: 1) the FEA proteins likely facilitate Fe uptake in excess Fe conditions in both stationary phase and at alkaline pH, as revealed by comparative transcriptomic and ICP-MS/MS analyses. FEA2 especially appears to serve a unique function to over-accumulate Fe in alkaline condition. However, results from NanoSIMS imaging indicated that they have no obvious impact on the allocation of intracellular Fe; 2) in addition to its better-known function in Fe buffer and storage, the FER1 protein seems to also play a role in both Fe acquisition and mobilization. This hypothesis was made based on the far greater Fe accumulation observed in the *fer1* mutant relative to the wild type, as well as the mutant's failure to benefit from this Fe pool for growth in subsequent Fe limitation. Beside the FEA and FER1, experimental data also revealed FRE1, CVL1, CVL2, and NRAMP1 to at least partially involve in Fe transport in luxury Fe condition. Meanwhile, there might be different mechanisms for intracellular Fe distribution in Chlamydomonas, depending on the location of the Fe source (*e.g.* Fe inside vs. outside of the acidocalcisome vs. extracellular Fe). Growth data suggested that accessing acidocalcisome-associated Fe might be a slower process than to access Fe stored outside of the acidocalcisome. Finally, Fe metabolism interconnects with the homeostases of many other essential nutrients, including Cu, Zn, Ca, and P, as has become evident in results presented throughout this dissertation.

APPENDIX

I. Supplementary Data Pertaining to Chapter 2

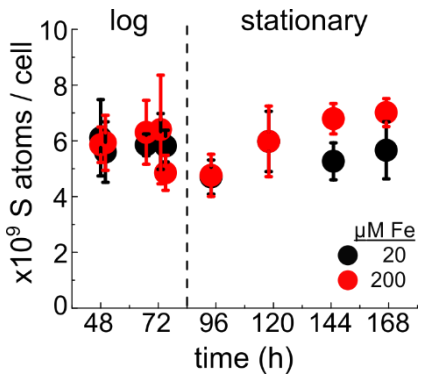

Supplementary Figure 1. S content per cell is constant. S was quantitated by ICP-MS/MS, normalized to cell numbers measured by a hemocytometer. Cells were grown in replete Fe (20 µM, black) or excess Fe condition (200 µM, red), collected at the indicated hours post-inoculation. Averages are shown with error bars indicating standard deviation of 3 independent cultures.

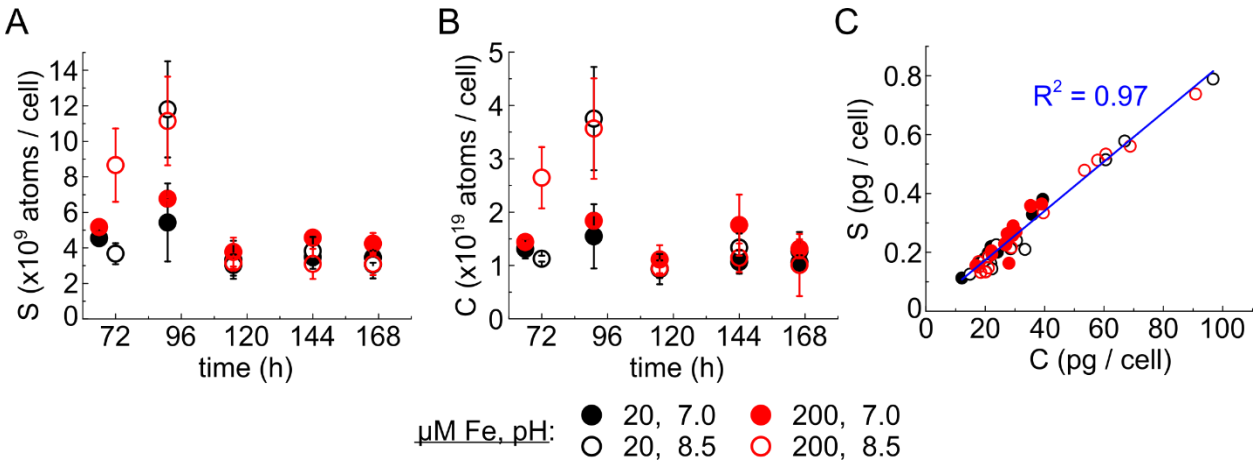

Supplementary Figure 2. S accumulation in cells correlates with biomass. (A) S content and (B) biomass of cells inoculated into TAP media containing 20 (black) or 200 (red) µM Fe, starting at either pH 7.0 (filled circles) or pH 8.5 (open circles), collected at the indicated hours post-inoculation. S content was measured by ICP-MS/MS. Biomass was measured as non-purgeable organic carbon content in cells by TOC analyzer. Averages are shown with error bars indicating standard deviation of 3 independent cultures. (C) Correlation of the S content and biomass data in (A) and (B) using all individual data points. R^2 value corresponds to linear regression fitting of the data points.

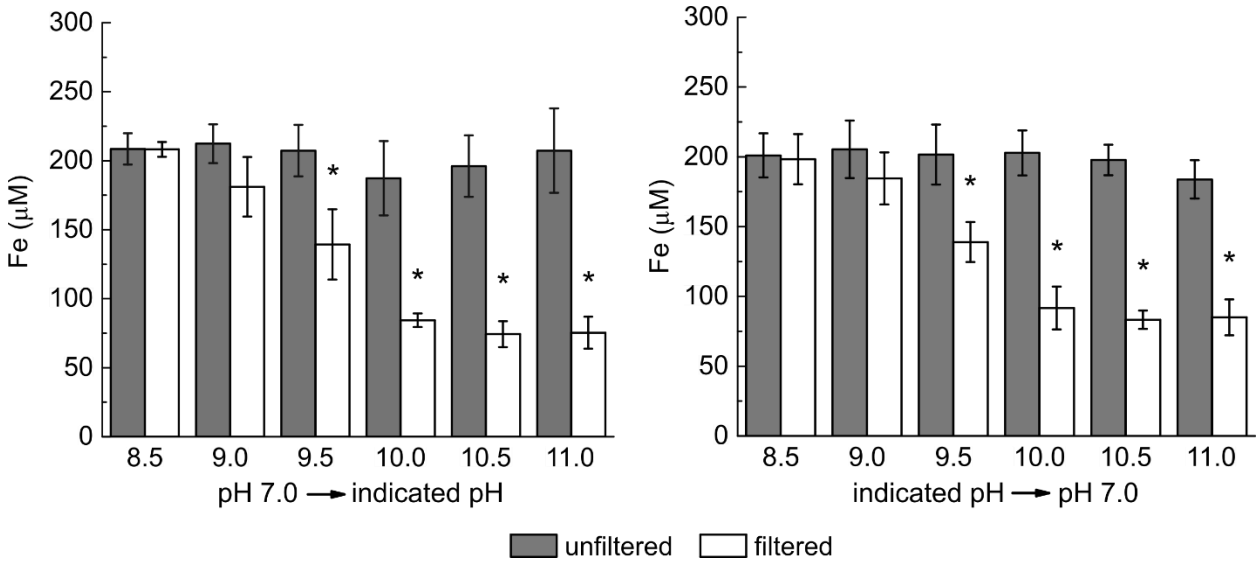

Supplementary Figure 3. Fe significantly precipitates in cell-free TAP medium at pH 9.5 and higher. Sterile TAP medium containing 200 µM Fe was titrated from pH 7.0 to pH 8.5, 9.0, 9.5, 10.0, 10.5, and 11.0 with KOH (left), or reversely from the higher pHs to pH 7.0 with acetic acid (right). The samples were left at room temperature for 30 mins at each titration point. An aliquot of each sample was filtered through a 0.2 µm filter to remove aggregates. Fe contents in both the filtered (white) and unfiltered (grey) samples were quantified by ICP-MS/MS. The Fe content detected in the unfiltered samples represents the total amount of Fe in the medium, whereas the Fe content detected in the filtered samples represents the soluble Fe pool in the medium. Asterisks indicate significant differences (t-test, $p \leq 0.05$) between the indicated filtered and unfiltered concentrations. Averages are shown with error bars indicating standard deviation of 3 independent cultures.

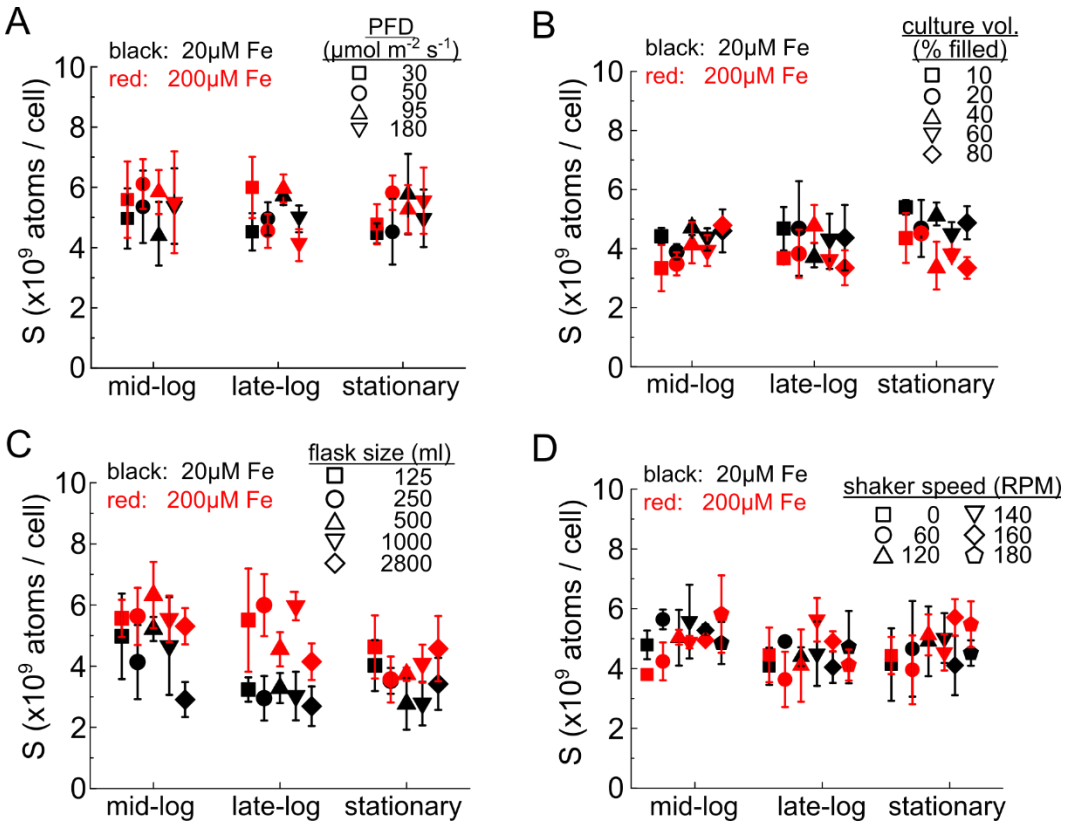

Supplementary Figure 4. S content per cell across time is similar among varied PFD and aeration parameters. (A-D) S content of cells grown in TAP with 20 (black) or 200 (red) μM Fe, collected during mid-log (2-4 x 10^6 cells/ml), late-log (6-8 x 10^6 cells/ml), and stationary growth (5-day post-inoculation, ~1 x 10^7 cells/ml), as measured by ICP-MS/MS. Data are normalized to cell numbers measured by a hemocytometer. Perturbations: (A) photon flux density (PFD), (B) fill-fraction of culture-to-flask volume, (C) vessel size, and (D) shaker speed. Averages are shown with error bars indicating standard deviation of 3 independent cultures.

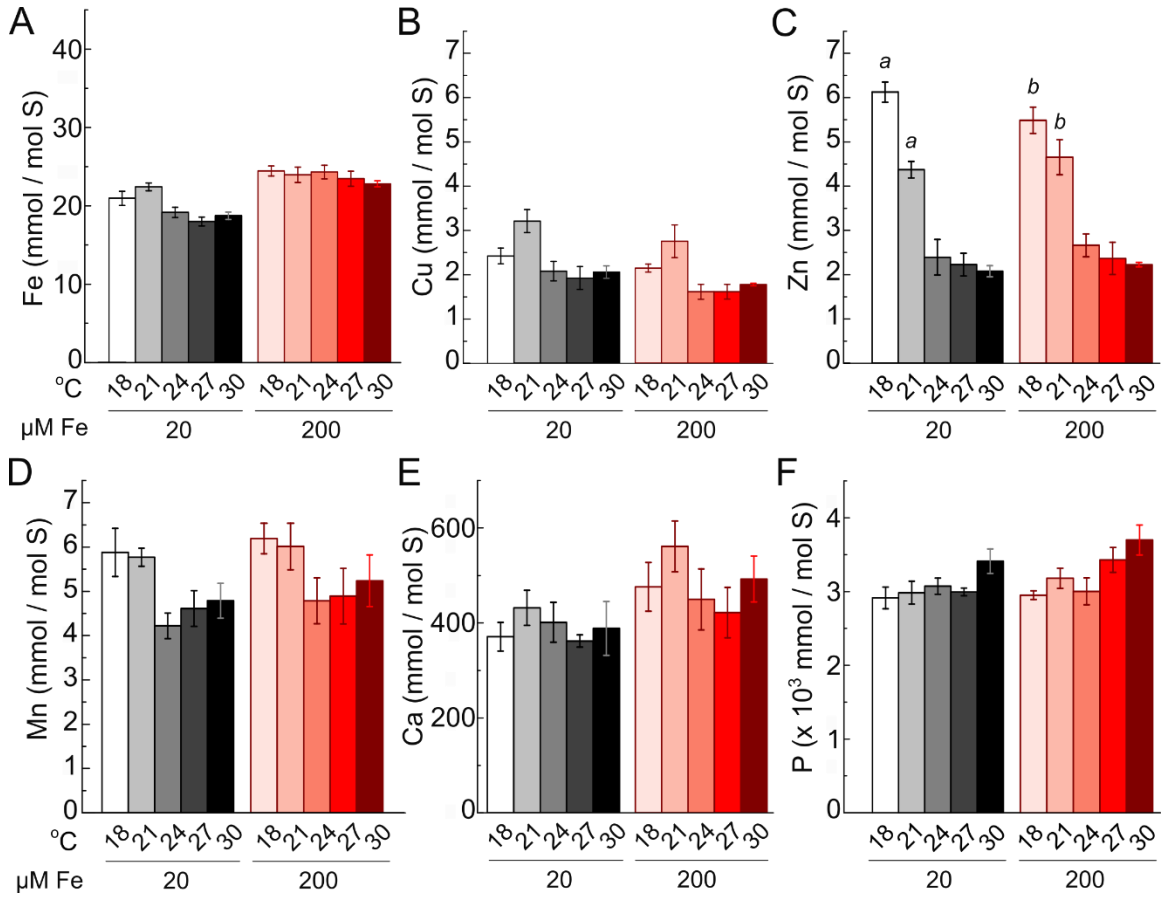

Supplementary Figure 5. Fe, Cu, Ca, and P levels correlate with S content in cells under temperature fluctuation. (A-F) Cell-associated Fe (A), Cu (B), Zn (C), Mn (D), Ca (E) and P (F) content as measured by ICP-MS/MS at mid-log growth (2-4 x 10^6 cells/ml), normalized to S content. Cells were grown at the indicated temperatures under replete (20 µM) and excess (200 µM) Fe conditions. *a* and *b* indicate significant differences (t-test, $p \leq 0.013$, multiple Bonferroni-corrected) to cells grown at 24ºC with 20 µM Fe (*a*) or 200 µM Fe (*b*). Averages are shown with error bars indicating standard deviation of 3 independent cultures.

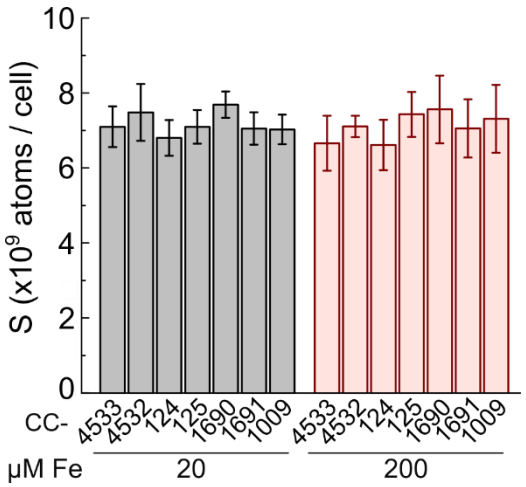

Supplementary Figure 6. S content per cell is similar among the 7 tested Chlamydomonas wild-type strains at log growth. S content in the indicated strains was quantitated by ICP-MS/MS, normalized to cell numbers measured by a hemocytometer. Cells were grown in replete Fe (20 µM, grey) and excess Fe (200 µM, pink) conditions and collected at mid-log growth (2-4 x 10^6 cells/ml). Averages are shown with error bars indicating standard deviation of 3 independent cultures.

II. Supplementary Data Pertaining to Chapter 3

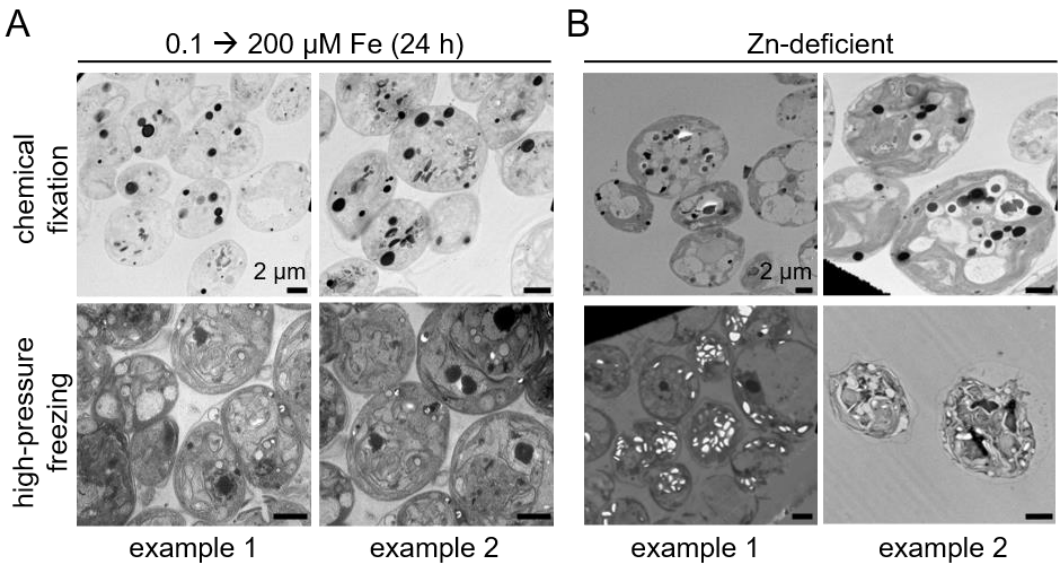

Supplementary Figure 7. High-pressure freezing induces abnormal morphology in Zn-deficient cells, but not in cells transiently overloaded with Fe. (A, B) TEM images of Fe-limiting cells (grown in 0.1 µM Fe TAP medium) supplied with 200 µM Fe for 24 h (A) and Zn-deficient cells (grown in Zn-free TAP medium) (B) after they were chemically fixed (top) or high-pressure frozen and freeze-substituted (bottom). The resin infiltration, embedding, and sectioning procedures following fixation by either method were the same for all samples. Scale bar, 2 µm.

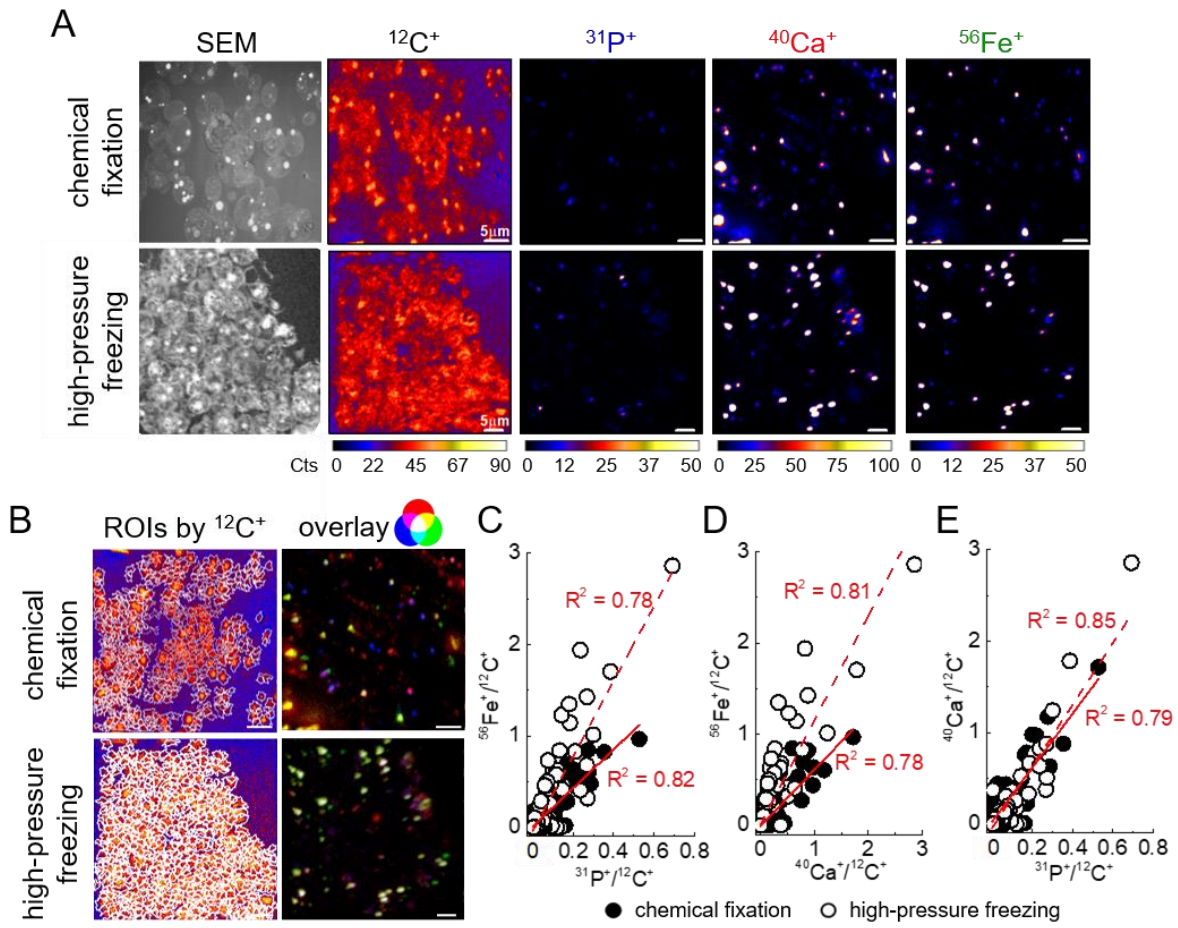

Supplementary Figure 8. Fe, Ca, and P distributions are similar between chemically fixed- vs. high-pressure frozen cells transiently overloaded with Fe. (A) Correlated SEM and NanoSIMS images of Fe-limiting cells (grown in 0.1 µM Fe TAP medium) supplied with 200 µM Fe for 24 h that were chemically fixed (top) or high-pressure frozen and freeze-substituted (bottom). (B, left) Non-overlapping ROIs covering all cell areas were generated by an automated algorithm in the analysis software based on $^{12}C^+$ distribution (left). The ROIs were used for correlative quantification shown in (C-E). (B, right) The overlaid RGB images of $^{31}P^+$ (blue), $^{40}Ca^+$ (red), and $^{56}Fe^+$ (green) as presented in (A) show colocalization between the three elements. (C, D, E) Correlative quantification of $^{12}C^+$-normalized $^{56}Fe^+$ with $^{31}P^+$ (C) and $^{40}Ca^+$ (D), and $^{40}Ca^+$ with $^{31}P^+$ (E), of the NanoSIMS imaged cells shown in (A) and (B). Each point in the plots corresponds to a ROI shown in (B). R^2 values correspond to linear regression fitting of the two sets of data points (solid line, chemical fixation; dash line, high-pressure freezing).

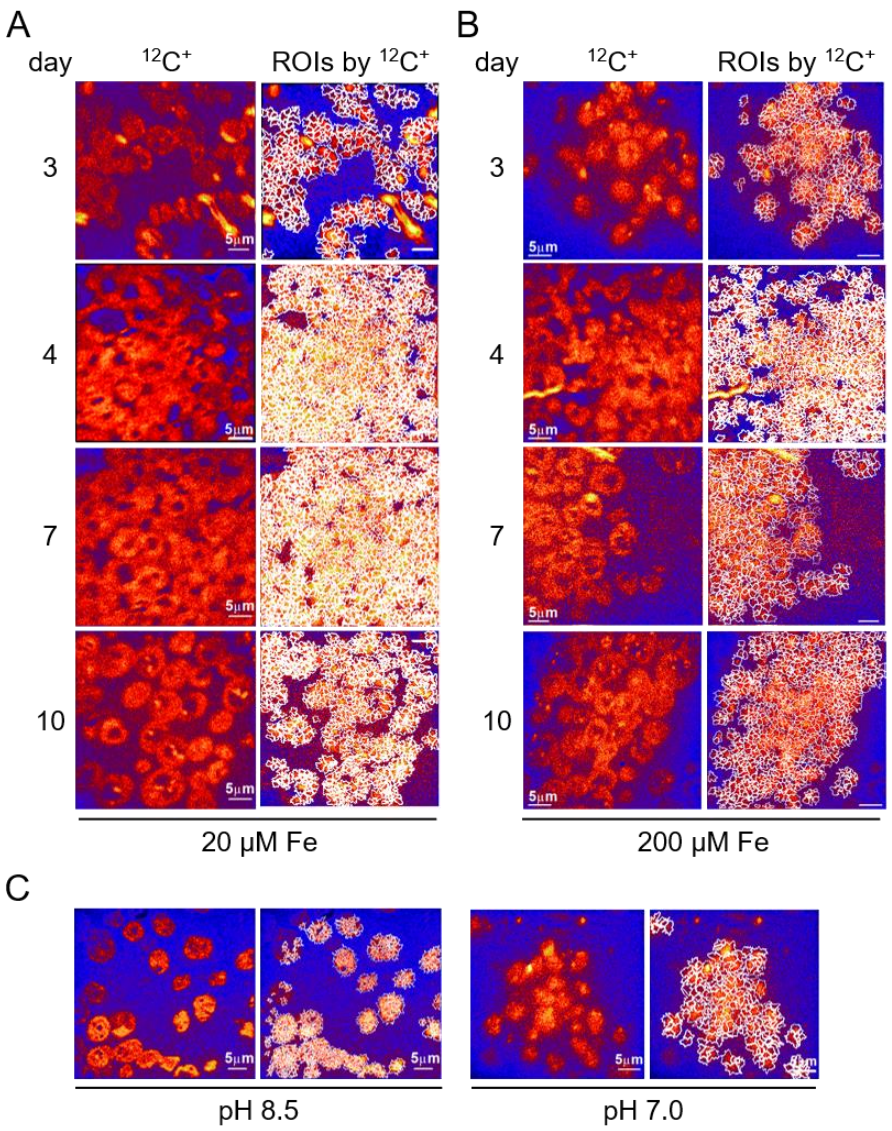

Supplementary Figure 9. ROIs for quantification of NanoSIMS data were defined using an automated algorithm in the analysis software. (A-C) NanoSIMS images of the $^{12}C^+$ distribution in samples as shown in Figure 3.1A (A), Figure 3.2A (B), and Figure 3.5 (C) (left), and illustrations of regions of interest (ROIs) corresponding to each sample, generated based on the $^{12}C^+$ distribution (right). An automated algorithm that sub-divided cells into non-overlapping small particles was used to generate the ROIs. Ion ratios ($^{31}P^+/^{12}C^+$, $^{40}Ca^+/^{12}C^+$, and $^{56}Fe^+/^{12}C^+$) were quantified for each ROI based on ion counts per cycle. These ratios were used for the subcellular correlative quantifications shown in Figure 3.1B-D, Figure 3.2B-D, and Figure 3.6.

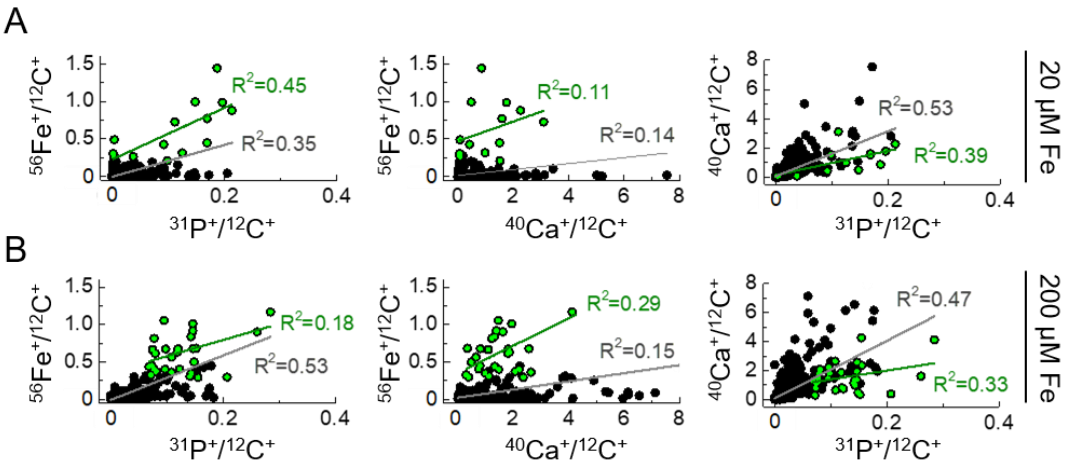

Supplementary Figure 10. Correlations between Fe, Ca, and P in late stationary cells using either ROIs covering all cell areas or ROIs with only high Fe count are mostly similar. (A, B) Subcellular correlative quantification of $^{12}C^+$-normalized $^{56}Fe^+$ with $^{31}P^+$ (left) and $^{40}Ca^+$ (middle), and of $^{40}Ca^+$ with $^{31}P^+$ (right), from NanoSIMS imaged cells grown in TAP medium with 20 µM Fe (A) or 200 µM Fe (B), collected on day 10 post-inoculation. The data are the same as those shown in Figure 3.1 (A) and 3.2 (B). Each point in the plots corresponds to a ROI generated by an automated algorithm in the analysis software (see Supplementary Figure 9A, B). The green points highlight the ROIs where $^{56}Fe^+$ count >12; the black points show all the remaining ROIs. The gray lines indicate the linear regression fitting for all points (black and green), while the green lines indicate the linear regression fitting only for the green points. R^2 values correspond to each linear regression fitting.

III. Supplementary Data Pertaining to Chapter 4

Supplementary Table 1. Abundances of the metal handling- and non-metal-associated transport genes from Table 1 under replete, deficient, and limiting Fe conditions

				mean RPKM (μM Fe)		
Process	**Locus ID**	**Gene Name**	**Description**	**20**	**1**	**0.25**
iron homeostasis	Cre12.g546550	*FEA1*	Fe-assimilating protein	248	2417	3629
	Cre12.g546600	*FEA2*	Fe-assimilating protein	6.9	378	2762
	Cre09.g393150	*FOX1*	Multicopper ferroxidase	178	795	1386
	Cre12.g531200	*FOX2*	Multicopper ferroxidase	9.1	7.4	4.7
	Cre17.g707700	*NRAMP1*	Mn/Fe transporter	7.8	7.1	9.0
	Cre12.g546500	*TEF22*	DOMON domain; cytochrome b_{561} / Fe^{3+}-reductase domain	51	384	841
	Cre05.g241400		Fe^{3+} reductase-like transmembrane component *	13	76	175
proton, calcium, and phosphate transport	Cre16.g655200	*PTB6*	Na^+/Phosphate symporter	1.5	1.8	2.2
	Cre12.g489400	*PTB7*	Na^+/Phosphate symporter	6.5	9.6	22
	Cre02.g144650	*PTB12*	Na^+/Phosphate symporter	0.1	0.1	0.4
	Cre16.g686750	*PTA3*	H^+/phosphate symporter *	12	17	26
	Cre08.g379550	*PHT4*	Na^+-dependent phosphate transporter	9.1	6.3	6.1
	Cre16.g681750		Ca^{2+}-transporting ATPase *	6.8	15	35
	Cre01.g036350		Ca^{2+}-transporting ATPase *	63	63	67
	Cre09.g410050		Ca^{2+}-translocating P-type ATPase *	5.3	4.9	1.8
	Cre04.g217954		Ca^{2+} transporting P-type ATPase *	5.6	7.8	3.7
	Cre09.g410100		Ca^{2+}-translocating P-type ATPase *	57	63	68
	Cre01.g044050		V-type H^+-transporting ATPase subunit *e* *	63	63	67

The mean Reads Per Kilobase of transcript per Million mapped fragments (RPKM) are cited from Urzica et al. (1).
Locus IDs correspond to the *C. reinhardtii* v.5.5 genome annotations, available on Phytozome. Functional annotations were manually curated. Asterisks indicate putative functions.

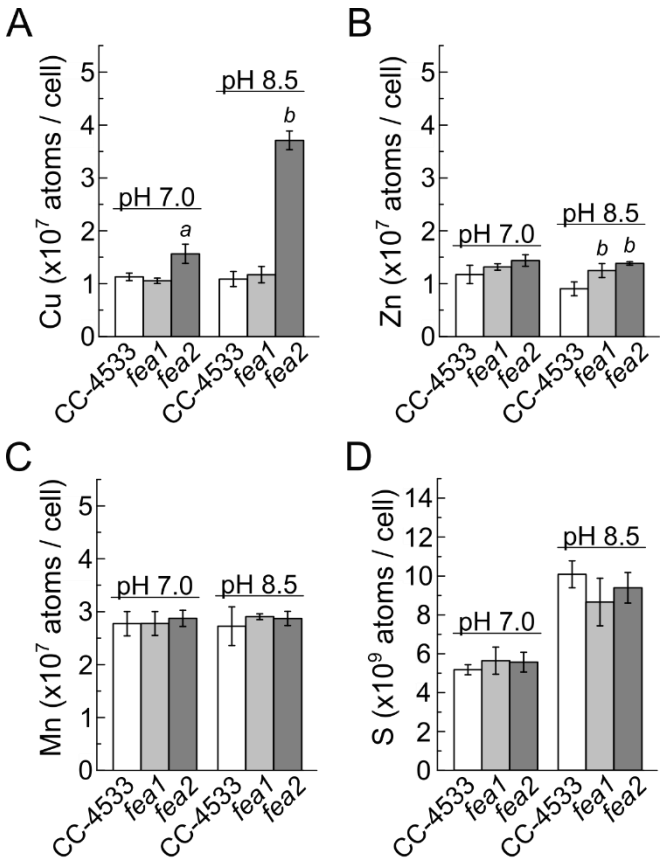

Supplementary Figure 11. Cu accumulation in the *fea2* mutant strain increases significantly compared to the wild-type and the *fea1* strains. (A-D) Abundances of Cu (A), Zn (B), Mn (C), and S (D) associated with the same cells described in Figure 4.2, as measured by ICP-MS/MS. The cells were collected during mid-log growth (2-4 x 10^6 cells/ml). The corresponding strains and pH of the growth media are as indicated. *a* and *b* represent significant differences (t-test, $p \leq 0.05$) to CC-4533 in the neutral pH condition (*a*) and in the alkaline pH condition (*b*). Averages are shown with error bars indicating standard deviation of 3 independent cultures.

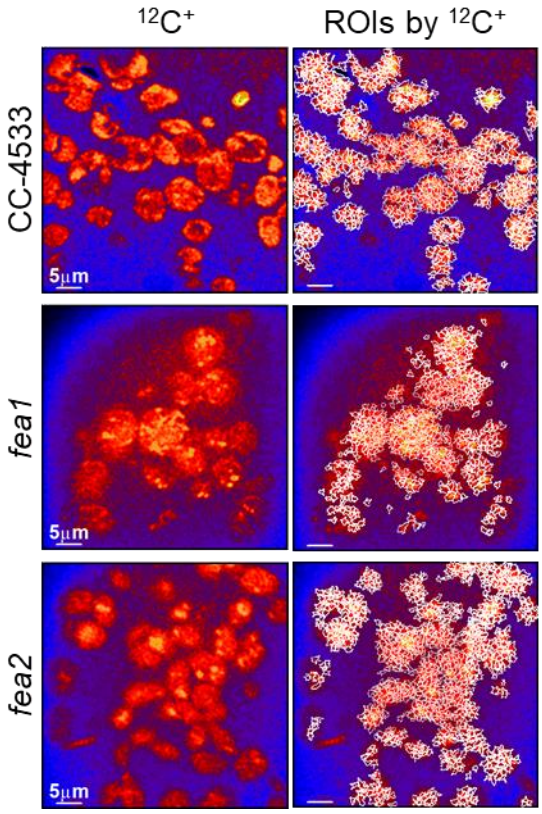

Supplementary Figure 12. An automated algorithm in the NanoSIMS analysis software was used to define ROIs for data quantification. NanoSIMS images of $^{12}C^+$ distribution in samples as shown in Figure 4.4A (left), and illustrations of regions of interest (ROIs) corresponding to each sample, generated based on the $^{12}C^+$ distribution (right). An automated algorithm that sub-divided cells into non-overlapping small particles was used to generate the ROIs. Ion ratios ($^{31}P^+/^{12}C^+$, $^{40}Ca^+/^{12}C^+$, and $^{56}Fe^+/^{12}C^+$) were quantified for each ROI based on ion counts per cycle. These ratios were used for the subcellular correlative quantifications shown in Figure 4.4B-D.

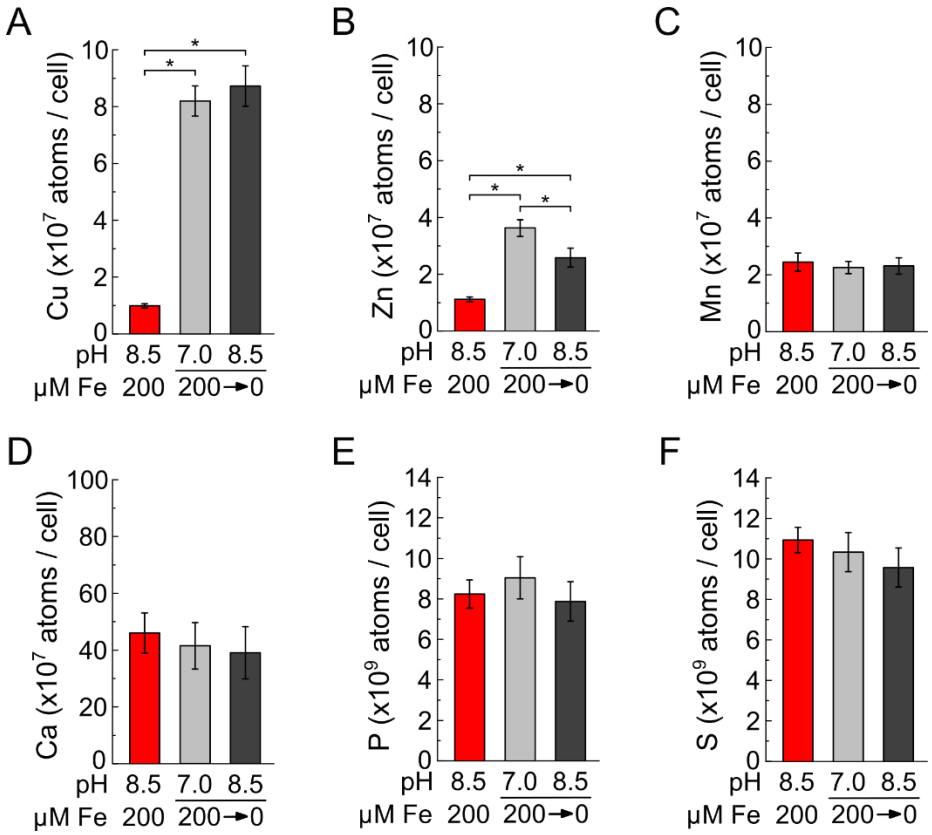

Supplementary Figure 13. Cells accumulate more Cu and Zn upon transfer from alkaline, excess Fe medium into Fe-free media. (A-F) Abundances of Cu (A), Zn (B), Mn (C), Ca (D), P (E), and S (F) associated with the cells described in Figure 4.5, as measured by ICP-MS/MS. The corresponding Fe concentration and pH of the growth media are as indicated. Asterisks represent significant differences (t-test, $p \leq 0.05$) between the bracketed data points. Averages are shown with error bars indicating standard deviation of 3 independent cultures.

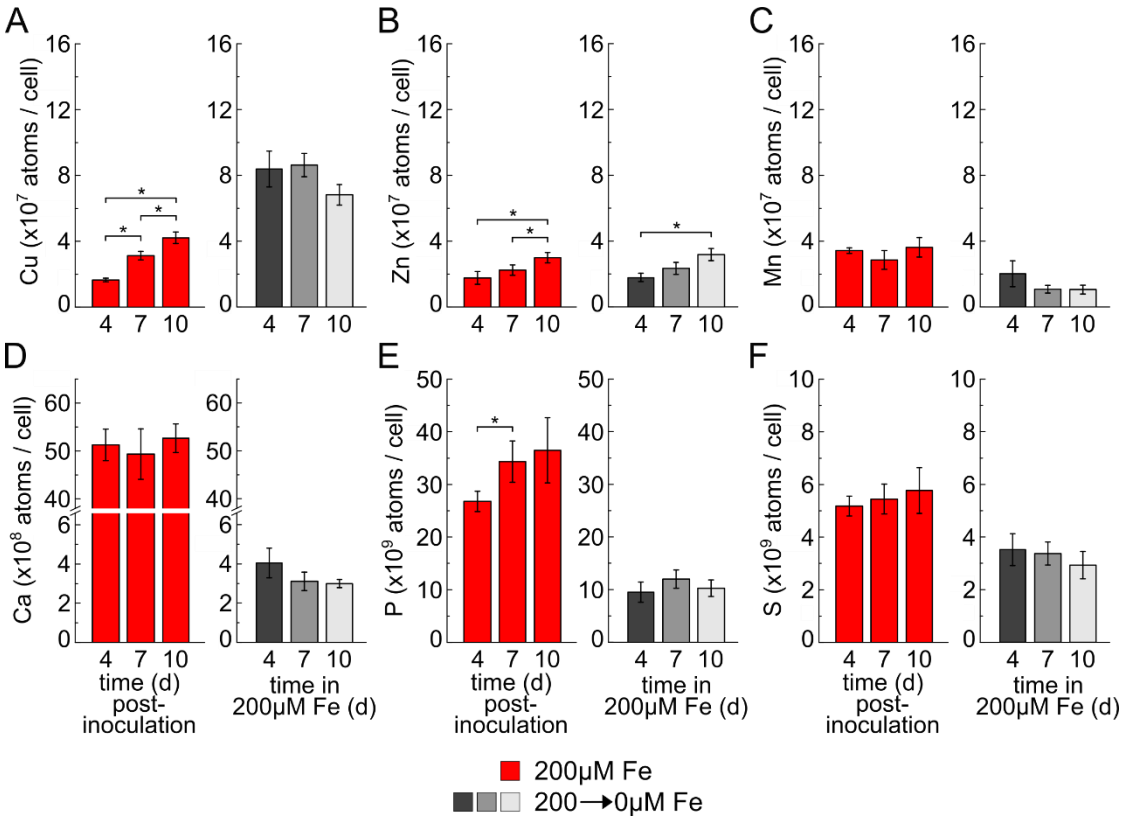

Supplementary Figure 14. Cu content increases but Ca and P contents are reduced in cells upon transfer from excess Fe to Fe-free condition at neutral pH. (A-F) Cu (A), Zn (B), Mn (C), Ca (D), P (E), and S (F) contents associated with the cells described in Figure 4.6, as measured by ICP-MS/MS. The elemental contents of cells before and after the transfer from Fe-excess to Fe-free medium are represented by red bars and the different gray bars, respectively. Asterisks represent significant differences (t-test, $p \leq 0.05$) between the bracketed data points. Averages are shown with error bars indicating standard deviation of 3 independent cultures.

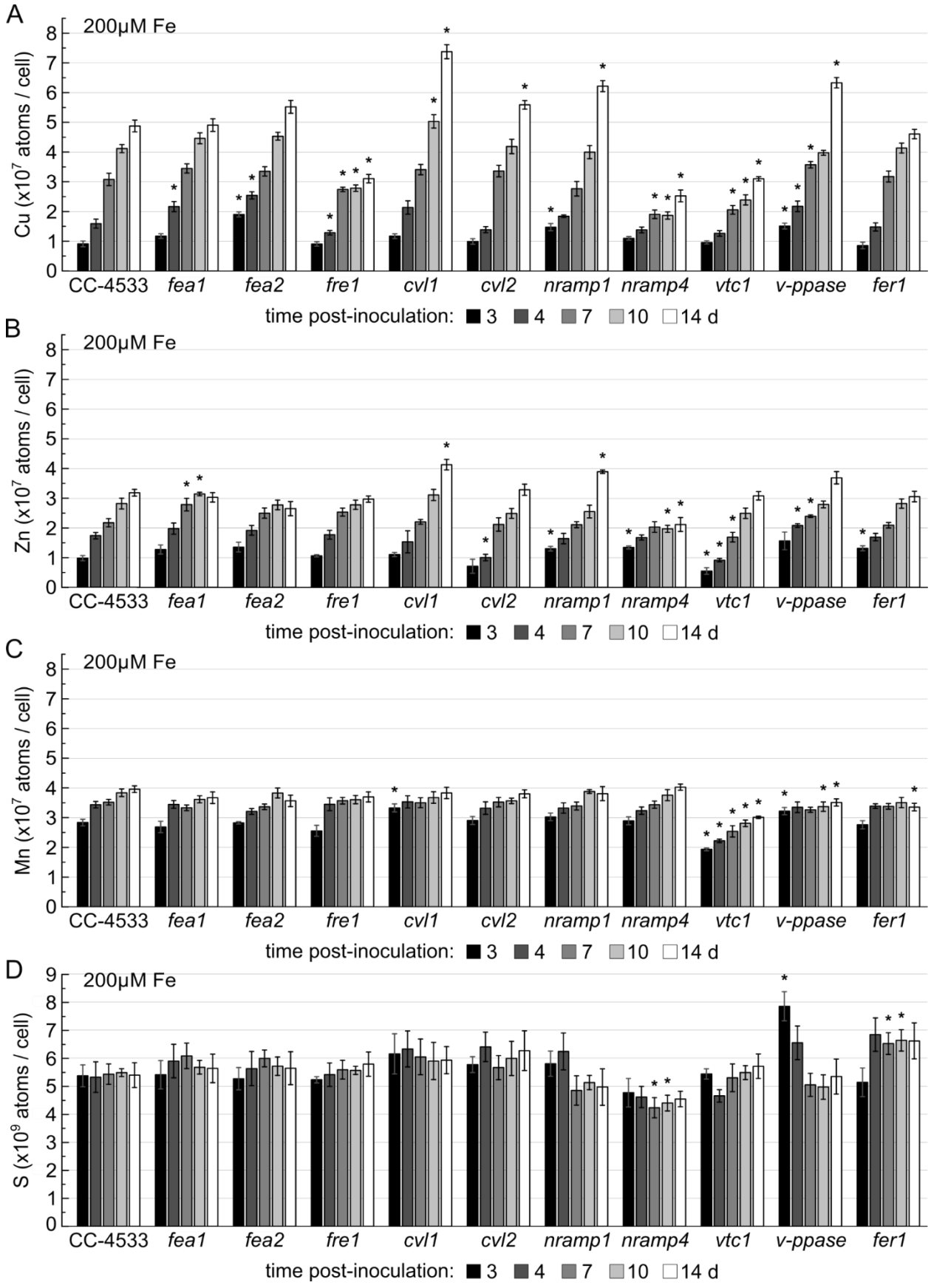
A
200μM Fe
Cu (x10^7 atoms / cell)
CC-4533
fea1
fea2
fre1
cvl1
cvl2
nramp1
nramp4
vtc1
v-ppase
fer1
time post-inoculation: 3 4 7 10 14 d
B
200μM Fe
Zn (x10^7 atoms / cell)
C
200μM Fe
Mn (x10^7 atoms / cell)
D
200μM Fe
S (x10^9 atoms / cell)

Supplementary Figure 15. Cu accumulations between the wild-type and many tested mutant strains are significantly different under excess Fe condition. (A-D) Abundances of Cu (A), Zn (B), Mn (C), and S (D) associated with the same cells described in Figure 4.7, as measured by ICP-MS/MS. The corresponding strains are as indicated. The cells were collected on day 3, 4, 7, 10, and 14 post-inoculation. Asterisks represent significant differences (t-test, $p \leq 0.01$, multiple Bonferroni-corrected) to the wild-type CC-4533 cells at each time point. Averages are shown with error bars indicating standard deviation of 3 independent cultures.

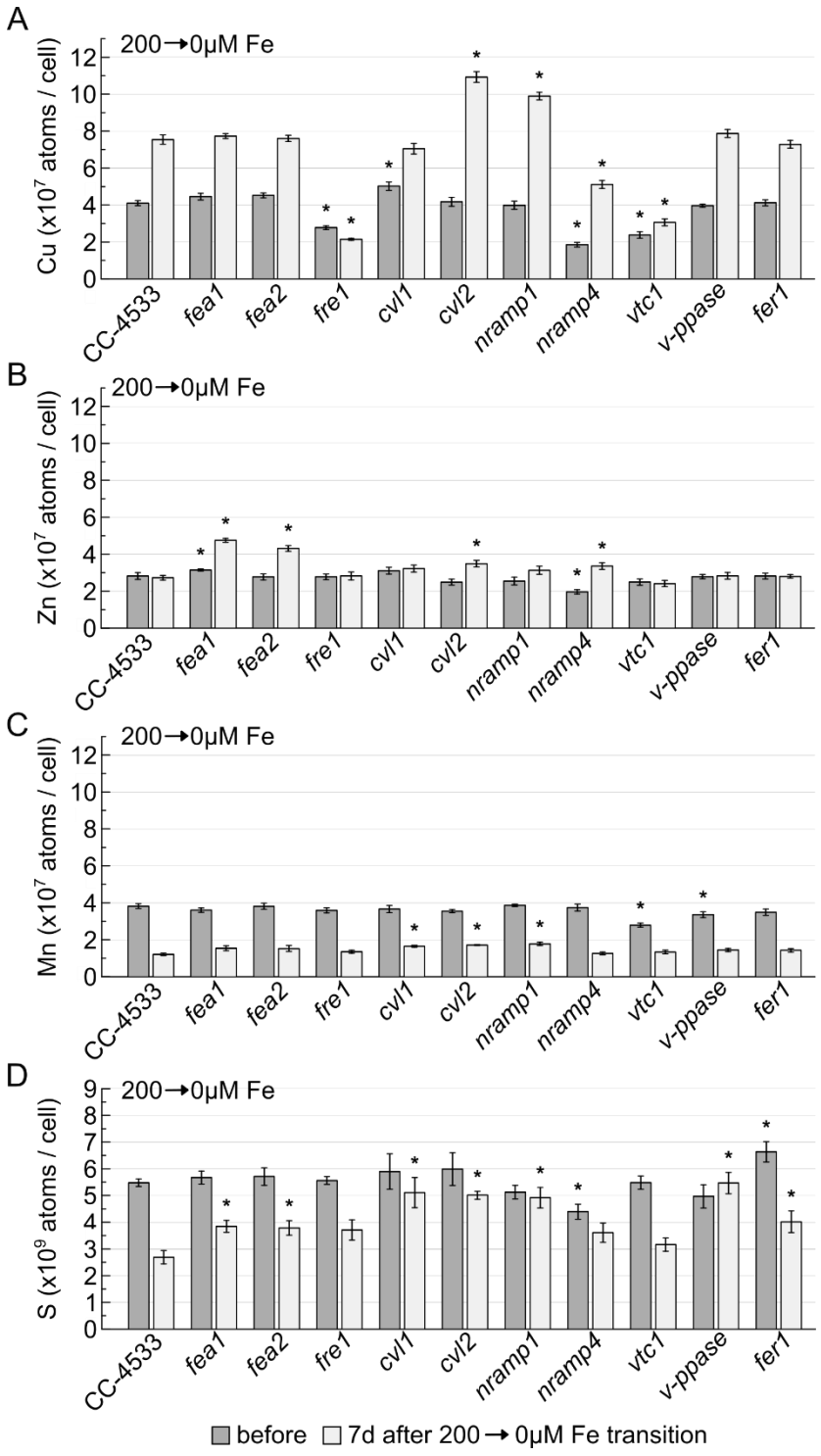

Supplementary Figure 16. The *fre1*, *cvl2*, *nramp1*, and *vtc1* mutant strains are significantly affected in Cu accumulation. (A-D) Abundances of Cu (A), Zn (B), Mn (C), and S (D) associated with the same cells described in Figure 4.9 before (dark gray) and 7 days after the medium transfer (light gray), as measured by ICP-MS/MS. The corresponding strains are as indicated. Asterisks represent significant differences (t-test, $p \leq 0.01$, multiple Bonferroni-corrected) between the wild-type CC-4533 cells and each mutant at the equivalent time points. Averages are shown with error bars indicating standard deviation of 3 independent cultures.

REFERENCES

1. Blaby-Haas CE, Merchant SS (2013) Iron sparing and recycling in a compartmentalized cell. *Curr Opin Microbiol* 16(6):677–685.

2. Staiger D (2002) Chemical Strategies for Iron Acquisition in Plants. *Angew Chemie - Int Ed* 41(13):2259–2264.

3. Imlay JA (2006) Iron-sulphur clusters and the problem with oxygen. *Mol Microbiol* 59(4):1073–1082.

4. Imlay JA (2008) Cellular Defenses against Superoxide and Hydrogen Peroxide. *Annu Rev Biochem* 77:755–776.

5. Capdevila DA, Edmonds KA, Giedroc DP (2017) Metallochaperones and metalloregulation in bacteria. *Essays Biochem* 61(2):177–200.

6. Blaby-Haas CE, Merchant SS (2017) Regulating cellular trace metal economy in algae. *Curr Opin Plant Biol* 39:88–96.

7. Merchant SS, Helmann JD (2012) Elemental Economy. Microbial Strategies for Optimizing Growth in the Face of Nutrient Limitation. *Adv Microb Physiol* 60:91–210.

8. Blaby-Haas CE, Merchant SS (2013) Metal Homeostasis: Sparing and Salvaging Metals in Chloroplasts. *Encyclopedia of Inorganic and Bioinorganic Chemistry*, pp 1–13.

9. Merchant SS (2010) The Elements of Plant Micronutrients. *Plant Physiol* 154(2):512–515.

10. Gimpel JA, Specht EA, Georgianna DR, Mayfield SP (2013) Advances in microalgae engineering and synthetic biology applications for biofuel production. *Curr Opin Chem Biol* 17(3):489–495.

11. Stephenson PG, Moore CM, Terry MJ, Zubkov M V., Bibby TS (2011) Improving photosynthesis for algal biofuels: toward a green revolution. *Trends Biotechnol* 29(12):615–623.

12. Merchant SS, et al. (2007) The Chlamydomonas Genome Reveals the Evolution of Key Animal and Plant Functions. *Science (80-)* 318(5848):245–250.

13. Silflow CD, Lefebvre PA (2001) Assembly and Motility of Eukaryotic Cilia and Flagella. Lessons from *Chlamydomonas reinhardtii*. *Plant Physiol* 127(4):1500–1507.

14. Kindle KL (1990) High-frequency nuclear transformation of *Chlamydomonas reinhardtii*. *Proc Natl Acad Sci U S A* 87(3):1228–1232.

15. Shrager J, et al. (2003) *Chlamydomonas reinhardtii* Genome Project. A Guide to the Generation and Use of the cDNA Information. *Plant Physiol* 131(2):401–408.

16. Blaby IK, et al. (2014) The Chlamydomonas genome project: A decade on. *Trends Plant Sci* 19(10):672–680.

17. Li X, et al. (2016) An Indexed, Mapped Mutant Library Enables Reverse Genetics Studies of Biological Processes in *Chlamydomonas reinhardtii*. *Plant Cell* 28(2):367–387.

18. Li X, et al. (2019) A genome-wide algal mutant library and functional screen identifies genes required for eukaryotic photosynthesis. *Nat Genet* 51(4):627–635.

19. Sager R, Granick S (1953) Nutritional Studies with *Chlamydomonas reinhardi*. *Ann N Y Acad Sci* 56(5):831–838.

20. Harris EH (2008) *The Chlamydomonas Sourcebook* eds Harris E, Stern D, Witman G (Academic Press, Cambridge, MA). 2nd Ed.

21. Moseley JL, et al. (2002) Adaptation to Fe-deficiency requires remodeling of the photosynthetic apparatus. *EMBO J* 21(24):6709–6720.

22. La Fontaine S, et al. (2002) Copper-Dependent Iron Assimilation Pathway in the Model Photosynthetic Eukaryote *Chlamydomonas reinhardtii*. *Eukaryot Cell* 1(5):736–757.

23. Long JC, Merchant SS (2008) Photo-oxidative Stress Impacts the Expression of Genes Encoding Iron Metabolism Components in Chlamydomonas. *Photochem Photobiol* 84(6):1395–1403.

24. Urzica EI, et al. (2012) Systems and *Trans*-System Level Analysis Identifies Conserved Iron Deficiency Responses in the Plant Lineage. *Plant Cell* 24(10):3921–48.

25. Kropat J, et al. (2011) A revised mineral nutrient supplement increases biomass and growth rate in *Chlamydomonas reinhardtii*. *Plant J* 66(5):770–780.

26. Terauchi AM, Peers G, Kobayashi MC, Niyogi KK, Merchant SS (2010) Trophic status of *Chlamydomonas reinhardtii* influences the impact of iron deficiency on photosynthesis. *Photosynth Res* 105(1):39–49.

27. Theil EC (1987) Ferritin: Structure, Gene Regulation, and Cellular Function in Animals, Plants, and Microorganisms. *Annu Rev Biochem* 56(1):289–315.

28. Briat JF, et al. (2010) New insights into ferritin synthesis and function highlight a link between iron homeostasis and oxidative stress in plants. *Ann Bot* 105(5):811–822.

29. Briat J-F, Duc C, Ravet K, Gaymard F (2010) Ferritins and iron storage in plants. *Biochim Biophys Acta - Gen Subj* 1800(8):806–814.

30. Arosio P, Ingrassia R, Cavadini P (2009) Ferritins: A family of molecules for iron storage, antioxidation and more. *Biochim Biophys Acta* 1790(7):589–599.

31. Pfaffen S, et al. (2015) A Diatom Ferritin Optimized for Iron Oxidation but Not Iron Storage. *J Biol Chem* 290(47):28416–28427.

32. Ravet K, et al. (2009) Ferritins control interaction between iron homeostasis and oxidative stress in Arabidopsis. *Plant J* 57(3):400–412.

33. Ravet K, Pilon M (2013) Copper and Iron Homeostasis in Plants: The Challenges of Oxidative Stress. *Antioxidants Redox Signal* 19(9):919–932.

34. Laulhere JP, Laboure AM, Briat JF (1989) Mechanism of the Transition from Plant Ferritin to Phytosiderin. *J Biol Chem* 264(6):3629–3635.

35. Santambrogio P, et al. (1992) Evidence That a Salt Bridge in the Light Chain Contributes to the Physical Stability Difference between Heavy and Light Human Ferritins. *J Biol Chem* 267(20):14077–14083.

36. Long JC, Sommer F, Allen MD, Lu S-F, Merchant SS (2008) FER1 and FER2 Encoding Two Ferritin Complexes in *Chlamydomonas reinhardtii* Chloroplasts Are Regulated by Iron. *Genetics* 179(1):137–147.

37. Petit JM, Briat JF, Lobréaux S (2001) Structure and differential expression of the four members of the *Arabidopsis thaliana* ferritin gene family. *Biochem J* 359(3):575–582.

38. Arosio P, Elia L, Poli M (2017) Ferritin, Cellular Iron Storage and Regulation. *IUBMB Life* 69(6):414–422.

39. Busch A, Rimbauld B, Naumann B, Rensch S, Hippler M (2008) Ferritin is required for rapid remodeling of the photosynthetic apparatus and minimizes photo-oxidative stress in response to iron availability in *Chlamydomonas reinhardtii*. *Plant J* 55(2):201–211.

40. Botebol H, et al. (2015) Central role for ferritin in the day/night regulation of iron homeostasis in marine phytoplankton. *Proc Natl Acad Sci* 112(47):14652–14657.

41. Lampe RH, et al. (2018) Different iron storage strategies among bloom-forming diatoms. *Proc Natl Acad Sci U S A* 115(52):E12275–E12284.

42. Docampo R (2016) The origin and evolution of the acidocalcisome and its interactions with other organelles. *Mol Biochem Parasitol* 209(1–2):3–9.

43. Li SC, Kane PM (2009) The yeast lysosome-like vacuole: Endpoint and crossroads. *Biochim Biophys Acta - Mol Cell Res* 1793(4):650–663.

44. Tan X, et al. (2019) A Review of Plant Vacuoles: Formation, Located Proteins, and Functions. *Plants* 8(9):327.

45. Thomine S, Vert G (2013) Iron transport in plants: better be safe than sorry. *Curr Opin Plant Biol* 16(3):322–327.

46. Blaby-Haas CE, Merchant SS (2014) Lysosome-related Organelles as Mediators of Metal Homeostasis. *J Biol Chem* 289(41):28129–28136.

47. Eide DJ, Bridgham JT, Zhao Z, Mattoon JR (1993) The vacuolar H^+-ATPase of *Saccharomyces cerevisiae* is required for efficient copper detoxification, mitochondrial function, and iron metabolism. *MGG Mol Gen Genet* 241(3–4):447–456.

48. MacDiarmid CW, Milanick MA, Eide DJ (2002) Biochemical Properties of Vacuolar Zinc Transport Systems of *Saccharomyces cerevisiae*. *J Biol Chem* 277(42):39187–39194.

49. Kane PM (2006) The Where, When, and How of Organelle Acidification by the Yeast Vacuolar H^+-ATPase . *Microbiol Mol Biol Rev* 70(1):177–191.

50. Van Ho A, Ward DMV, Kaplan J (2002) Transition Metal Transport in Yeast. *Annu Rev Microbiol* 56:237–261.

51. Cohen A, Perzov N, Nelson H, Nelson N (1999) A Novel Family of Yeast Chaperons Involved in the Distribution of V-ATPase and Other Membrane Proteins. *J Biol Chem* 274(38):26885–26893.

52. Müller O, et al. (2002) The Vtc proteins in vacuole fusion: coupling NSF activity to V_0 *trans*-complex formation. *EMBO J* 21(3):259–269.

53. Hothorn M, et al. (2009) Catalytic Core of a Membrane-Associated Eukaryotic Polyphosphate Polymerase. *Science (80-)* 324(5926):513–516.

54. Ogawa N, DeRisi J, Brown PO (2000) New Components of a System for Phosphate Accumulation and Polyphosphate Metabolism in *Saccharomyces cerevisiae* Revealed by Genomic Expression Analysis. *Mol Biol Cell* 11(12):4309–4321.

55. Rogers JC (2011) Internal Membranes in Maize Aleurone Protein Storage Vacuoles: Beyond Autophagy . *Plant Cell* 23(12):4168–4172.

56. Wada T, Lott JNA (1997) Light and electron microscopic and energy dispersive X-ray microanalysis studies of globoids in protein bodies of embryo tissues and the aleurone layer of rice (*Oryza sativa* L.) grains. *Can J Bot* 75(7):1137–1147.

57. Regvar M, et al. (2011) New insights into globoids of protein storage vacuoles in wheat aleurone using synchrotron soft X-ray microscopy. *J Exp Bot* 62(11):3929–3939.

58. Kim EJ, Zhen RG, Rea PA (1994) Heterologous expression of plant vacuolar pyrophosphatase in yeast demonstrates sufficiency of the substrate-binding subunit for proton transport. *Proc Natl Acad Sci U S A* 91(13):6128–6132.

59. Viotti C (2014) ER and vacuoles: never been closer. *Front Plant Sci* 5(FEB):20.

60. Ruiz FA, Marchesini N, Seufferheld M, Govindjee, Docampo R (2001) The Polyphosphate Bodies of *Chlamydomonas reinhardtii* Possess a Proton-pumping Pyrophosphatase and Are Similar to Acidocalcisomes. *J Biol Chem* 276(49):46196–46203.

61. Hong-Hermesdorf A, et al. (2014) Subcellular metal imaging identifies dynamic sites of Cu accumulation in *Chlamydomonas*. *Nat Chem Biol* 10(12):1034–1042.

62. Tsednee M, et al. (2019) Manganese co-localizes with calcium and phosphorus in *Chlamydomonas* acidocalcisomes and is mobilized in manganese-deficient conditions. *J Biol Chem* 294(46):17626–17641.

63. Schmollinger S, et al. (2021) Single-cell visualization and quantification of trace metals in *Chlamydomonas* lysosome-related organelles. *Proc Natl Acad Sci* 118(16):e2026811118.

64. Nagasaka S, Nishizawa NK, Watanabe T, Mori S, Yoshimura E (2003) Evidence that electron-dense bodies in *Cyanidium caldarium* have an iron-storage role. *BioMetals* 16(3):465–470.

65. Docampo R, Huang G (2016) Acidocalcisomes of Eukaryotes. *Curr Opin Cell Biol* 41:66–72.

66. Paz Y, Shimoni E, Weiss M, Pick U (2007) Effects of Iron Deficiency on Iron Binding and Internalization into Acidic Vacuoles in Dunaliella salina. *Plant Physiol* 144(3):1407–15.

67. Beyenbach KW, Wieczorek H (2006) The V-type H^+ ATPase: molecular structure and function, physiological roles and regulation. *J Exp Biol* 209(4):577–589.

68. Rea PA, Poole RJ (1993) Vacuolar H^+-Translocating Pyrophosphatase. *Annu Rev Plant Physiol Plant Mol Biol* 44(1):157–180.

69. Lander N, Cordeiro C, Huang G, Docampo R (2016) Polyphosphate and Acidocalcisomes. *Biochem Soc Trans* 44(1):1–6.

70. Herbik A, Bölling C, Buckhout TJ (2002) The Involvement of a Multicopper Oxidase in Iron Uptake by the Green Algae *Chlamydomonas reinhardtii*. *Plant Physiol* 130(4):2039–2048.

71. Terzulli AJ, Kosman DJ (2009) The Fox1 Ferroxidase of *Chlamydomonas reinhardtii*: A New Multicopper Oxidase Structural Paradigm. *J Biol Inorg Chem* 14(2):315–325.

72. Chen JC, Hsieh SI, Kropat J, Merchant SS (2008) A Ferroxidase Encoded by FOX1 Contributes to Iron Assimilation under Conditions of Poor Iron Nutrition in *Chlamydomonas*.

Eukaryot Cell 7(3):541–545.

73. Askwith C, Kaplan J (1998) Iron and copper transport in yeast and its relevance to human disease. *Trends Biochem Sci* 23(4):135–138.

74. Radisky D, Kaplan J (1999) Regulation of Transition Metal Transport across the Yeast Plasma Membrane. *J Biol Chem* 274(8):4481–4484.

75. Stearman R, Yuan DS, Yamaguchi-Iwai Y, Klausner RD, Dancis A (1996) A Permease-Oxidase Complex Involved in High-Affinity Iron Uptake in Yeast. *Science (80-)* 271(5255):1552–1557.

76. Askwith C, Kaplan J (1997) An Oxidase-Permease-based Iron Transport System in *Schizosaccharomyces pombe* and Its Expression in *Saccharomyces cerevisiae*. *J Biol Chem* 272(1):401–405.

77. Eck R, Hundt S, Härtl A, Roemer E, Künkel W (1999) A multicopper oxidase gene from *Candida albicans*: cloning, characterization and disruption. *Microbiology* 145(9):2415–2422.

78. Knight SAB, Lesuisse E, Stearman R, Klausner RD, Dancis A (2002) Reductive iron uptake by *Candida albicans*: role of copper, iron and the *TUP1* regulator. *Microbiology* 148(1):29–40.

79. Ramanan N, Wang Y (2000) A High-Affinity Iron Permease Essential for *Candida albicans* Virulence. *Science (80-)* 288(5468):1062–1064.

80. Blaby-Haas CE, Merchant SS (2012) The ins and outs of algal metal transport. *Biochim Biophys Acta - Mol Cell Res* 1823(9):1531–1552.

81. Reinhardt I, Haebel S, Herbik A, Buckhout TJ (2006) Proteomic Studies under Iron Stress: Iron Deficiency-Induced Regulation of Protein Synthesis in the Green Alga *Chlamydomonas reinhardtii*. *Iron Nutrition in Plants and Rhizospheric Microorganisms*, eds Barton LL, Abadía J (Springer , Dordrecht), pp 371–393.

82. Allen MD, del Campo JA, Kropat J, Merchant SS (2007) *FEA1* , *FEA2* , and *FRE1* , Encoding Two Homologous Secreted Proteins and a Candidate Ferrireductase, Are Expressed Coordinately with *FOX1* and *FTR1* in Iron-Deficient *Chlamydomonas reinhardtii*. *Eukaryot Cell* 6(10):1841–1852.

83. Dancis A, Klausner RD, Hinnebusch AG, Barriocanal JG (1990) Genetic Evidence that Ferric Reductase is Required for Iron Uptake in *Saccharomyces cerevisiae*. *Mol Cell Biol* 10(5):2294–2301.

84. Dancis A, Roman DG, Anderson GJ, Hinnebusch AG, Klausner RD (1992) Ferric reductase of *Saccharomyces cerevisiae*: Molecular characterization, role in iron uptake, and transcriptional control by iron. *Proc Natl Acad Sci U S A* 89(9):3869–3873.

85. Robinson NJ, Procter CM, Connolly EL, Guerinot M Lou (1999) A ferric-chelate reductase for iron uptake from soils. *Nature* 397(6721):694–697.

86. Kustka AB, Allen AE, Morel FMM (2007) Sequence analysis and transcriptional regulation of iron acquisition genes in two marine diatoms. *J Phycol* 43(4):715–729.

87. Allen AE, et al. (2008) Whole-cell response of the pennate diatom *Phaeodactylum tricornutum* to iron starvation. *Proc Natl Acad Sci U S A* 105(30):10438–10443.

88. Guerinot M Lou (2000) The ZIP family of metal transporters. *Biochim Biophys Acta - Biomembr* 1465(1–2):190–198.

89. Eide D, Broderius M, Fett J, Guerinot M Lou (1996) A novel iron-regulated metal transporter from plants identified by functional expression in yeast. *Proc Natl Acad Sci U S A* 93(11):5624–5628.

90. Vert G, et al. (2002) IRT1, an Arabidopsis Transporter Sssential for Iron Uptake from the Soil and for Plant Growth. *Plant Cell* 14(6):1223–33.

91. Sasaki T, Kurano N, Miyachi S (1998) Cloning and Characterization of High-CO_2-Specific cDNAs from a Marine Microalga, *Chlorococcum littorale*, and Effect of CO_2 Concentration and Iron Deficiency on the Gene Expression . *Plant Cell Physiol* 39(2):131–138.

92. Narayanan NN, et al. (2011) The iron assimilatory protein, FEA1, from *Chlamydomonas reinhardtii* facilitates iron-specific metal uptake in yeast and plants. *Front Plant Sci* 2(OCT):67.

93. Ihemere UE, Narayanan NN, Sayre RT (2012) Iron biofortification and homeostasis in transgenic cassava roots expressing the algal iron assimilatory gene, *FEA1*. *Front Plant Sci* 3(SEP):171.

94. Glaesener AG, Merchant SS, Blaby-Haas CE (2013) Iron economy in *Chlamydomonas reinhardtii*. *Front Plant Sci* 4(337). doi:10.3389/fpls.2013.00337.

95. Coutville P, Chaloupka R, Cellier MFM (2006) Recent progress in structure-function analyses of Nramp proton-dependent metal-ion transporters. *Biochem Cell Biol* 84(6):960–978.

96. Nevo Y, Nelson N (2006) The NRAMP family of metal-ion transporters. *Biochim Biophys Acta - Mol Cell Res* 1763(7):609–620.

97. Thomine S, Lelièvre F, Debarbieux E, Schroeder JI, Barbier-Brygoo H (2003) AtNRAMP3, a multispecific vacuolar metal transporter involved in plant responses to iron deficiency. *Plant J* 34(5):685–695.

98. Thomine S, Wang R, Ward JM, Crawford NM, Schroeder JI (2000) Cadmium and iron transport by members of a plant metal transporter family in *Arabidopsis* with homology to *Nramp* genes. *Proc Natl Acad Sci U S A* 97(9):4991–4996.

99. Lanquar V, et al. (2005) Mobilization of vacuolar iron by AtNRAMP3 and AtNRAMP4 is essential for seed germination on low iron. *EMBO J* 24(23):4041–4051.

100. Rosakis A, Köster W (2005) Divalent metal transport in the green microalga *Chlamydomonas reinhardtii* is mediated by a protein similar to prokaryotic Nramp homologues. *BioMetals* 18(1):107–120.

101. Liu XF, Culotta VC (1999) Post-translation Control of Nramp Metal Transport in Yeast. *J Biol Chem* 274(8):4863–4868.

102. Wolfe-Simon F, Starovoytov V, Reinfelder JR, Schofield O, Falkowski PG (2006) Localization and Role of Manganese Superoxide Dismutase in a Marine Diatom . *Plant Physiol* 142(4):1701–1709.

103. Li L, Chen OS, Ward DM, Kaplan J (2001) CCC1 Is a Transporter That Mediates Vacuolar Iron Storage in Yeast. *J Biol Chem* 276(31):29515–29519.

104. Li L, Bagley D, Ward DM, Kaplan J (2008) Yap5 Is an Iron-Responsive Transcriptional Activator That Regulates Vacuolar Iron Storage in Yeast. *Mol Cell Biol* 28(4):1326–1337.

105. Li L, Kaplan J (2004) A Mitochondrial-Vacuolar Signaling Pathway in Yeast That Affects Iron and Copper Metabolism. *J Biol Chem* 279(32):33653–33661.

106. Kim SA, et al. (2006) Localization of Iron in *Arabidopsis* Seed Requires the Vacuolar Membrane Transporter VIT1. *Science (80-)* 314(5803):1295–1298.

107. Morel FMM, Hudson RJM, Price NM (1991) Limitation of productivity by trace metals in the sea. *Limnol Oceanogr* 36(8):1742–1755.

108. Behrenfeld MJ, et al. (2009) Satellite-detected fluorescence reveals global physiology of ocean phytoplankton. *Biogeosciences* 6(5):779–794.

109. Marschner H (1995) *Mineral Nutrition of Higher Plants* (Academic Press, London). 2nd Ed.

110. Andreini C, Bertini I, Cavallaro G, Holliday GL, Thornton JM (2008) Metal ions in biological catalysis: from enzyme databases to general principles. *J Biol Inorg Chem* 13(8):1205–1218.

111. Waldron KJ, Rutherford JC, Ford D, Robinson NJ (2009) Metalloproteins and metal sensing. *Nature* 460(7257):823–830.

112. Gallaher SD, Fitz-Gibbon ST, Glaesener AG, Pellegrini M, Merchant SS (2015) Chlamydomonas Genome Resource for Laboratory Strains Reveals a Mosaic of Sequence Variation, Identifies True Strain Histories, and Enables Strain-Specific Studies. *Plant Cell* 27(9):2335–2352.

113. Bernát I (1983) The Distribution of Iron in Nature. *Iron Metab*:9–13.

114. Lundgren DG, Dean W (1979) Biogeochemistry of Iron. *Stud Environ Sci* 3(C):211–251.

115. Hutner SH, Provasoli L, Schatz A, Haskins CP (1950) Some Approaches to the Study of the Role of Metals in the Metabolism of Microorganisms. *Proc Am Philos Soc* 94(2):152–170.

116. Ma M, Zhu W, Wang Z, Witkamp GJ (2003) Accumulation, assimilation and growth inhibition of copper on freshwater alga (*Scenedesmus subspicatus* 86.81 SAG) in the presence of EDTA and fulvic acid. *Aquat Toxicol* 63(3):221–228.

117. Balcaen L, Bolea-Fernandez E, Resano M, Vanhaecke F (2015) Inductively coupled plasma – Tandem mass spectrometry (ICP-MS/MS): A powerful and universal tool for the interference-free determination of (ultra)trace elements – A tutorial review. *Anal Chim Acta* 894:7–19.

118. Salt DE, Baxter I, Lahner B (2008) Ionomics and the Study of the Plant Ionome. *Annu Rev Plant Biol* 59:709–733.

119. Harris EH (2009) Chlamydomonas in the Laboratory. *The Chlamydomonas Sourcebook*, ed Harrisduke E (Academic Press, Cambridge, MA), pp 241–302. 2nd Ed.

120. Strenkert D, et al. (2016) Genetically programmed changes in photosynthetic cofactor metabolism in copper-deficient Chlamydomonas. *J Biol Chem* 291(36):19118–19131.

121. Schmollinger S, et al. (2014) Nitrogen-Sparing Mechanisms in *Chlamydomonas* Affect the Transcriptome, the Proteome, and Photosynthetic Metabolism. *Plant Cell* 26(4):1410–1435.

122. Park J, McCormick SP, Chakrabarti M, Lindahl PA (2013) The Lack of Synchronization between Iron Uptake and Cell Growth Leads to Iron Overload in *Saccharomyces cerevisiae* during Post-exponential Growth Modes. *Biochemistry* 52:9413–9425.

123. Merchant SS, et al. (2006) Between a rock and a hard place: Trace element nutrition in Chlamydomonas. *Biochim Biophys Acta - Mol Cell Res* 1763(7):578–594.

124. Allen MD, Kropat J, Tottey S, Del Campo JA, Merchant SS (2006) Manganese Deficiency in Chlamydomonas Results in Loss of Photosystem II and MnSOD Function, Sensitivity to Peroxides, and Secondary Phosphorus and Iron Deficiency. *Plant Physiol* 143(1):263–277.

125. Sunda WG, Huntsman SA (1985) Regulation of cellular manganese and manganese transport rates in the unicellular alga *Chlamydomonas* 1. *Limnol Oceanogr* 30(1):71–80.

126. Castaings L, Alcon C, Kosuth T, Correia D, Curie C (2021) Manganese triggers phosphorylation-mediated endocytosis of the Arabidopsis metal transporter NRAMP1. *Plant J* 106(5). doi:10.1111/TPJ.15239.

127. Braun FJ, Hegemann P (1999) Direct measurement of cytosolic calcium and pH in living *Chlamydomonas reinhardtii* cells. *Eur J Cell Biol* 78(3):199–208.

128. Wheeler GL (2017) Calcium-Dependent Signalling Processes in Chlamydomonas. *Chlamydomonas: Molecular Genetics and Physiology*, ed Hippler M (Springer, Cham), pp 233–255.

129. Slocombe SP, et al. (2020) Fixing the Broken Phosphorus Cycle: Wastewater Remediation by Microalgal Polyphosphates. *Front Plant Sci* 11. doi:10.3389/fpls.2020.00982.

130. Goodenough U, Heiss AA, Roth R, Rusch J, Lee JH (2019) Acidocalcisomes: Ultrastructure, Biogenesis, and Distribution in Microbial Eukaryotes. *Protist* 170(3):287–313.

131. Yi Y, Guerinot M Lou (1996) Genetic evidence that induction of root Fe(III) chelate reductase activity is necessary for iron uptake under iron deficiency. *Plant J* 10(5):835–844.

132. Dhaliwal G, Lee T, Talwar D, Wang O (2017) Effect of varying pH adjusted media on the growth rate of Chlamydomonas reinhardtii | The Expedition. *Expedition* 7:1–14.

133. Visviki I, Santikul D (2000) The pH tolerance of Chlamydomonas applanata (Volvocales, Chlorophyta). *Arch Environ Contam Toxicol* 38(2):147–51.

134. Wilde KL, Stauber JL, Markich SJ, Franklin NM, Brown PL (2006) The effect of pH on the uptake and toxicity of copper and zinc in a tropical freshwater alga (Chlorella sp.). *Arch Environ Contam Toxicol* 51(2):174–185.

135. Macfie SM, Tarmohamed Y, Welbourn PM (1994) Effects of Cadmium, Cobalt, Copper, and Nickel on Growth of the Green Alga *Chlamydomonas reinhardtii*: The Influences of the Cell Wall and pH. *Arch Environ Contam Toxicol* 27(4):454–458.

136. Franklin NM, Stauber JL, Markich SJ, Lim RP (2000) pH-dependent toxicity of copper and uranium to a tropical freshwater alga (Chlorella sp.). *Aquat Toxicol* 48(2–3):275–289.

137. Guo R, et al. (2017) Ionomic and metabolic responses to neutral salt or alkaline salt stresses in maize (*Zea mays* L.) seedlings. *BMC Plant Biol* 17(41). doi:10.1186/s12870-017-0994-6.

138. Zhang JT, Mu CS (2009) Effects of saline and alkaline stresses on the germination, growth, photosynthesis, ionic balance and anti-oxidant system in an alkali-tolerant leguminous

forage *Lathyrus quinquenervius*. *Soil Sci Plant Nutr* 55(5):685–697.

139. Zaid A, Ahmad B, Jaleel H, Wani SH, Hasanuzzaman M (2020) A Critical Review on Iron Toxicity and Tolerance in Plants: Role of Exogenous Phytoprotectants. *Plant Micronutrients* (Springer International Publishing), pp 83–99.

140. Kamalanathan M, Pierangelini M, Shearman LA, Gleadow R, Beardall J (2015) Impacts of nitrogen and phosphorus starvation on the physiology of *Chlamydomonas reinhardtii*. *J Appl Phycol 2015 283* 28(3):1509–1520.

141. Dean AP, Nicholson JM, Sigee DC (2008) Impact of phosphorus quota and growth phase on carbon allocation in *Chlamydomonas reinhardtii*: an FTIR microspectroscopy study. *https://doi.org/101080/09670260801979287* 43(4):345–354.

142. Miller GW, Pushnik JC, Welkie GW (2008) Iron chlorosis, a world wide problem, the relation of chlorophyll biosynthesis to iron. *J Plant Nutr* 7(1–5):1–22.

143. Pushnik JC, Miller GW, Manwaring JH (2008) The role of iron in higher plant chlorophyll biosynthesis, maintenance and chloroplast biogenesis. *J Plant Nutr* 7(1–5):733–758.

144. Aung MS, Masuda H (2020) How Does Rice Defend Against Excess Iron?: Physiological and Molecular Mechanisms. *Front Plant Sci* 0:1102.

145. Mengel K, Geurtzen G (1986) Iron chlorosis on calcareous soils. Alkaline nutritional condition as the cause for the chlorosis. *J Plant Nutr* 9(3–7):161–173.

146. Hsieh E-J, Waters BM (2016) Alkaline stress and iron deficiency regulate iron uptake and riboflavin synthesis gene expression differently in root and leaf tissue: implications for iron deficiency chlorosis. *J Exp Bot* 67(19):5671–5685.

147. Fuglsang AT, et al. (2014) Receptor kinase-mediated control of primary active proton pumping at the plasma membrane. *Plant J* 80(6):951–964.

148. Tsai HH, Schmidt W (2021) The enigma of environmental pH sensing in plants. *Nat Plants* 7(2):106–115.

149. Smith RM, Martell AE (1989) *Critical Stability Constants* (Springer US, Boston, MA) doi:10.1007/978-1-4615-6764-6.

150. The Dow Chemical Company (2018) *Chelation Chemistry: General Concepts of the Chemistry of Chelation* Available at: https://www.dow.com/content/dam/dcc/documents/en-us/mark-prod-info/113/113-01388-01-chelation-chemistry-general-concepts-of-the-chemistry-of-chelation.pdf?iframe=true [Accessed April 9, 2021].

151. Serra-Cardona A, Canadell D, Ariño J (2015) Coordinate responses to alkaline pH stress in budding yeast. *Microb Cell* 2(6):182–196.

152. Serrano R, Bernal D, Simón E, Ariño J (2004) Copper and Iron Are the Limiting Factors for Growth of the Yeast *Saccharomyces cerevisiae* in an Alkaline Environment. *J Biol Chem* 279(19):19698–19704.

153. Casamayor A, et al. (2012) The role of the Snf1 kinase in the adaptive response of *Saccharomyces cerevisiae* to alkaline pH stress. *Biochem J* 444(1):39–49.

154. Förster C, Kane PM (2000) Cytosolic Ca^{2+} Homeostasis Is a Constitutive Function of the V-ATPase in *Saccharomyces cerevisiae*. *J Biol Chem* 275(49):38245–38253.

155. Freimoser FM, Hürlimann HC, Jakob CA, Werner TP, Amrhein N (2006) Systematic screening of polyphosphate (poly P) levels in yeast mutant cells reveals strong interdependence with primary metabolism. *Genome Biol* 7(11). doi:10.1186/gb-2006-7-11-r109.

156. Thomas MR, O'Shea EK (2005) An intracellular phosphate buffer filters transient fluctuations in extracellular phosphate levels. *Proc Natl Acad Sci U S A* 102(27):9565–9570.

157. Castro CD, Meehan AJ, Koretsky AP, Domach MM (1995) In Situ ^{31}P Nuclear Magnetic Resonance for Observation of Polyphosphate and Catabolite Responses of Chemostat-Cultivated *Saccharomyces cerevisiae* after Alkalinization. *Appl Environ Microbiol* 61(12):4448–4453.

158. Rodriguez IB, Ho TY (2017) Interactive effects of spectral quality and trace metal availability on the growth of Trichodesmium and Symbiodinium. *PLoS One* 12(11). doi:10.1371/journal.pone.0188777.

159. Bonente G, Pippa S, Castellano S, Bassi R, Ballottari M (2012) Acclimation of *Chlamydomonas reinhardtii* to Different Growth Irradiances. *J Biol Chem* 287(8):5833–5847.

160. Murchie EH, Hubbart S, Peng S, Horton P (2005) Acclimation of photosynthesis to high irradiance in rice: gene expression and interactions with leaf development. *J Exp Bot* 56(411):449–460.

161. Im CS, Grossman AR (2002) Identification and regulation of high light-induced genes in *Chlamydomonas reinhardtii*. *Plant J* 30(3):301–313.

162. Niyogi KK, Björkman O, Grossman AR (1997) The roles of specific xanthophylls in photoprotection. *Proc Natl Acad Sci U S A* 94(25):14162–14167.

163. Mettler T, et al. (2014) Systems Analysis of the Response of Photosynthesis, Metabolism, and Growth to an Increase in Irradiance in the Photosynthetic Model Organism *Chlamydomonas reinhardtii*. *Plant Cell* 26(6):2310–2350.

164. Zhu J, et al. (2017) Impact of aeration disturbances on endogenous phosphorus fractions and their algae growth potential from malodorous river sediment. *Environ Sci Pollut Res* 24(9):8062–8070.

165. de la Noüe J, Cloutier-Mantha L, Walsh P, Picard G (1984) Influence of Agitation and Aeration Modes on Biomass Production by *Oocystis* sp. Grown on Wastewaters. *Biomass* 4(1):43–58.

166. Qi F, et al. (2017) Enhancing growth of *Chlamydomonas reinhardtii* and nutrient removal in diluted primary piggery wastewater by elevated CO_2 supply. *Water Sci Technol* 75(10):2281–2290.

167. Abreu IN, et al. (2020) Changes in lipid and carotenoid metabolism in *Chlamydomonas reinhardtii* during induction of CO_2-concentrating mechanism: Cellular response to low CO_2 stress. *Algal Res* 52:102099.

168. Singh SP, Singh P (2014) Effect of CO_2 concentration on algal growth: A review. *Renew Sustain Energy Rev* 38:172–179.

169. Dumay QC, Debut AJ, Mansour NM, Saier MH (2006) The Copper Transporter (Ctr) Family of Cu^+ Uptake Systems. *J Mol Microbiol Biotechnol* 11(1–2):10–19.

170. Zhao B, et al. (2011) Effect of cultivation mode on microalgal growth and CO_2 fixation. *Chem Eng Res Des* 89(9):1758–1762.

171. Im C-S, Zhang Z, Shrager J, Chang C-W, Grossman AR (2003) Analysis of light and CO_2 regulation in *Chlamydomonas reinhardtii* using genome-wide approaches. *Photosynth Res* 75(2):111–125.

172. Wang Y, Stessman DJ, Spalding MH (2015) The CO2 concentrating mechanism and photosynthetic carbon assimilation in limiting CO2: how Chlamydomonas works against the gradient. *Plant J* 82(3):429–448.

173. Goldman JC, Mann R (1980) Temperature-influenced variations in speciation and chemical composition of marine phytoplankton in outdoor mass cultures. *J Exp Mar Bio Ecol* 46(1):29–39.

174. Converti A, Casazza AA, Ortiz EY, Perego P, Del Borghi M (2009) Effect of temperature and nitrogen concentration on the growth and lipid content of *Nannochloropsis oculata* and *Chlorella vulgaris* for biodiesel production. *Chem Eng Process Process Intensif* 48(6):1146–1151.

175. Teoh ML, Chu WL, Phang SM (2010) Effect of temperature change on physiology and biochemistry of algae: A review. *Malaysian J Sci* 29(2):82–97.

176. Maikova A, Zalutskaya Z, Lapina T, Ermilova E (2016) The HSP70 chaperone machines of *Chlamydomonas* are induced by cold stress. *J Plant Physiol* 204:85–91.

177. Schroda M, Hemme D, Mühlhaus T (2015) The *Chlamydomonas* heat stress response. *Plant J* 82(3):466–480.

178. Valledor L, Furuhashi T, Hanak AM, Weckwerth W (2013) Systemic Cold Stress Adaptation of *Chlamydomonas reinhardtii*. *Mol Cell Proteomics* 12(8):2032–2047.

179. Gross JA, Jahn TL (1962) Cellular Responses to Thermal and Photo Stress I. *Euglena* and *Chlamydomonas*. *J Protozool* 9(3):340–346.

180. Hema R, Senthil-Kumar M, Shivakumar S, Chandrasekhara Reddy P, Udayakumar M (2007) *Chlamydomonas reinhardtii*, a model system for functional validation of abiotic stress responsive genes. *Planta* 226(3):655–670.

181. Giordano M, Norici A, Ratti S, Raven JA (2008) Role of Sulfur for Algae: Acquisition, Metabolism, Ecology and Evolution. *Sulfur Metabolism in Phototrophic Organisms*, eds Hell R, Dahl C, Knaff D, Leustek T (Springer, Dordrecht), pp 397–415.

182. Li X, Slavens S, Crunkleton DW, Johannes TW (2021) Interactive effect of light quality and temperature on *Chlamydomonas reinhardtii* growth kinetics and lipid synthesis. *Algal Res* 53:102127.

183. Lukeš M, Procházková L, Shmidt V, Nedbalová L, Kaftan D (2014) Temperature dependence of photosynthesis and thylakoid lipid composition in the red snow alga *Chlamydomonas* cf. *nivalis* (*Chlorophyceae*). *FEMS Microbiol Ecol* 89(2):303–315.

184. James GO, Hocart CH, Hillier W, Price GD, Djordjevic MA (2013) Temperature modulation of fatty acid profiles for biofuel production in nitrogen deprived Chlamydomonas reinhardtii. *Bioresour Technol* 127:441–447.

185. Morales-Sánchez D, Schulze PSC, Kiron V, Wijffels RH (2020) Temperature-Dependent

Lipid Accumulation in the Polar Marine Microalga *Chlamydomonas malina* RCC2488. *Front Plant Sci* 11:1–10.

186. Singh SP, Singh P (2015) Effect of temperature and light on the growth of algae species: A review. *Renew Sustain Energy Rev* 50:431–444.

187. Pazour GJ, Sineshchekov OA, Witman GB (1995) Mutational Analysis of the Phototransduction Pathway of *Chlamydomonas reinhardtii*. *J Cell Biol* 131(2):427–440.

188. Sager R (1955) Inheritance in the Green Alga *Chlamydomonas Rehinardi*. *Genetics* 40(4):476–489.

189. Terauchi AM, et al. (2009) Pattern of Expression and Substrate Specificity of Chloroplast Ferredoxins from *Chlamydomonas reinhardtii*. *J Biol Chem* 284(38):25867–25878.

190. Hanke GT, Kimata-Ariga Y, Taniguchi I, Hase T (2004) A Post Genomic Characterization of Arabidopsis Ferredoxins. *Plant Physiol* 134(1):255–264.

191. Page MD, et al. (2012) Fe Sparing and Fe Recycling Contribute to Increased Superoxide Dismutase Capacity in Iron-Starved *Chlamydomonas reinhardtii*. *Plant Cell* 24(6):2649–2665.

192. Nagasaka S, Yoshimura E (2008) External Iron Regulates Polyphosphate Content in the Acidophilic, Thermophilic Alga *Cyanidium caldarium*. *Biol Trace Elem Res* 125(3):286–289.

193. Mueller CW, et al. (2013) Advances in the Analysis of Biogeochemical Interfaces: NanoSIMS to Investigate Soil Microenvironments. *Advances in Agronomy* (Academic Press Inc.), pp 1–46.

194. Kubota K, Morono Y, Ito M (2017) Nanoscale Secondary-Ion Mass Spectrometry Imaging of Biological Structures. *Encyclopedia of Analytical Chemistry* (John Wiley & Sons, Ltd, Chichester, UK), pp 1–17.

195. Ackerman CM, et al. (2018) Multimodal LA-ICP-MS and nanoSIMS imaging enables copper mapping within photoreceptor megamitochondria in a zebrafish model of Menkes disease. *Metallomics* 10(3):474–485.

196. Doble PA, de Vega RG, Bishop DP, Hare DJ, Clases D (2021) Laser Ablation–Inductively Coupled Plasma–Mass Spectrometry Imaging in Biology. *Chem Rev*. doi:10.1021/acs.chemrev.0c01219.

197. Ackerman CM, Lee S, Chang CJ (2017) Analytical Methods for Imaging Metals in Biology: From Transition Metal Metabolism to Transition Metal Signaling. *Anal Chem* 89(1):22–41.

198. Vogt S, Ralle M (2013) Opportunities in multidimensional trace metal imaging: taking copper-associated disease research to the next level. *Anal Bioanal Chem* 405(6):1809–1820.

199. Leary SC, Ralle M (2020) Advances in visualization of copper in mammalian systems using X-ray fluorescence microscopy. *Curr Opin Chem Biol* 55:19–25.

200. Paunesku T, Vogt S, Maser J, Lai B, Woloschak G (2006) X-ray Fluorescence Microprobe Imaging in Biology and Medicine. *J Cell Biochem* 99(6):1489–1502.

201. Siegbahn M (1916) Relations between the K and L Series of the High-Frequency Spectra. *Nature* 96(2416):676.

202. Combs CA, Shroff H (2017) Fluorescence Microscopy: A Concise Guide to Current Imaging Methods. *Curr Protoc Neurosci* 2017:2.1.1-2.1.25.

203. Bayguinov PO, et al. (2018) Modern Laser Scanning Confocal Microscopy. *Curr Protoc Cytom* 85(1). doi:10.1002/cpcy.39.

204. Seufferheld M, et al. (2003) Identification of Organelles in Bacteria Similar to Acidocalcisomes of Unicellular Eukaryotes. *J Biol Chem* 278(32):29971–29978.

205. Au-Yeung HY, Chan J, Chantarojsiri T, Chang CJ (2013) Molecular Imaging of Labile Iron(II) Pools in Living Cells with a Turn-On Fluorescent Probe. *J Am Chem Soc* 135(40):15165–73.

206. Johnson UG, Porter KR (1968) Fine Structure of Cell Division in *Chlamydomonas reinhardi*. Basal Bodies and Microtubules. *J Cell Biol* 38(2):403–425.

207. Roberts K, Gurney-Smith M, Hills GJ (1972) Structure, Composition and Morphogenesis of the Cell Wall of *Chlamydomonas reinhardi*. I. Ultrastructure and Preliminary Chemical Analysis. *J Ultrasructure Res* 40(5–6):599–613.

208. O'Toole ET (2010) *Chlamydomonas*: Cryopreparation Methods for the 3-D Analysis of Cellular Organelles. *Methods in Cell Biology*, ed Müller-Reichert T (Academic Press, Cambridge, MA), pp 71–91.

209. O'Toole ET, Giddings TH, McIntosh JR, Dutcher SK (2003) Three-dimensional Organization of Basal Bodies from Wild-Type and δ-Tubulin Deletion Strains of *Chlamydomonas reinhardtii*. *Mol Biol Cell* 14(7):2999–3012.

210. Preble AM, Giddings TH, Dutcher SK (2001) Extragenic Bypass Suppressors of Mutations in the Essential Gene *BLD2* Promote Assembly of Basal Bodies With Abnormal Microtubules in *Chlamydomonas reinhardtii*. *Genetics* 157(1):163–181.

211. Moore KL, et al. (2010) NanoSIMS analysis of arsenic and selenium in cereal grain. *New Phytol* 185(2):434–445.

212. Mcdonald KL, Webb RI (2011) Freeze substitution in 3 hours or less. *J Microsc* 243(3):227–233.

213. McDonald KL (2014) Out with the old and in with the new: Rapid specimen preparation procedures for electron microscopy of sectioned biological material. *Protoplasma* 251(2):429–448.

214. Chen S, et al. (2014) The Bionanoprobe: hard X-ray fluorescence nanoprobe with cryogenic capabilities. *J Synchrotron Radiat* 21(1):66–75.

215. Vogt S (2003) MAPS : A set of software tools for analysis and visualization of 3D X-ray fluorescence data sets. *J Phys IV* 104:635–638.

216. Merchant S, Hill K, Howe G (1991) Dynamic interplay between two copper-titrating components in the transcriptional regulation of cyt *c6*. *EMBO J* 10(6):1383–1389.

217. Merchant S, Selman BR (1983) Identification of the α and β subunits of the chloroplast coupling factor one in *Chlamydomonas reinhardi*. *Eur J Biochem* 137(1–2):373–376.

218. Sanz-Luque E, Saroussi S, Huang W, Akkawi H, Grossman AR (2020) Metabolic control of acclimation to nutrient deprivation dependent on polyphosphate synthesis. *Sci Adv* 6(40). doi:10.1126/SCIADV.ABB5351.

219. Plouviez M, et al. (2021) Responses of Chlamydomonas reinhardtii during the transition from P-deficient to P-sufficient growth (the P-overplus response): The roles of the vacuolar transport chaperones and polyphosphate synthesis. *J Phycol* 57(3):988–1003.

220. Aksoy M, Pootakham W, Grossman AR (2014) Critical Function of a *Chlamydomonas reinhardtii* Putative Polyphosphate Polymerase Subunit during Nutrient Deprivation. *Plant Cell* 26(10):4214–4229.

221. Semin BK, et al. (2003) Accumulation of Ferrous Iron in *Chlamydomonas reinhardtii*. Influence of CO 2 and Anaerobic Induction of the Reversible Hydrogenase. *Plant Physiol* 131(4):1756–1764.

222. Briat J-F, Lobréaux S (1997) Iron transport and storage in plants. *Trends Plant Sci* 2(5):187–193.

223. Park J, McCormick SP, Cockrell AL, Chakrabarti M, Lindahl PA (2014) High-Spin Ferric Ions in *Saccharomyces cerevisiae* Vacuoles Are Reduced to the Ferrous State during Adenine-Precursor Detoxification. *Biochemistry* 53(24):3940–3951.

224. Kovács K, Kuzmann E, Tatár E, Vértes A, Fodor F (2009) Investigation of iron pools in cucumber roots by Mössbauer spectroscopy: direct evidence for the Strategy I iron uptake mechanism. *Planta* 229(2):271–278.

225. Aschar-Sobbi R, et al. (2008) High Sensitivity, Quantitative Measurements of Polyphosphate Using a New DAPI-Based Approach. *J Fluoresc* 18(5):859–866.

226. Keasling JD (1997) Regulation of Intracellular Toxic Metals and Other Cations by Hydrolysis of Polyphosphate. *Ann N Y Acad Sci* 829:242–249.

227. Docampo R (2006) Acidocalcisomes and Polyphosphate Granules. *Inclusions in Prokaryotes. Microbiology Monographs*, ed Shively JM (Springer, Berlin, Heidelberg), pp 53–70.

228. Lavoie M, Le Faucheur S, Fortin C, Campbell PGC (2009) Cadmium detoxification strategies in two phytoplankton species: Metal binding by newly synthesized thiolated peptides and metal sequestration in granules. *Aquat Toxicol* 92(2):65–75.

229. Martínez-Muñoz GA, Kane P (2008) Vacuolar and Plasma Membrane Proton Pumps Collaborate to Achieve Cytosolic pH Homeostasis in Yeast. *J Biol Chem* 283(29):20309–20319.

230. Ariño J, Ramos J, Sychrová H (2010) Alkali Metal Cation Transport and Homeostasis in Yeasts. *Microbiol Mol Biol Rev* 74(1):95–120.

231. Van Der Rest ME, et al. (1995) The Plasma Membrane of *Saccharomyces cerevisiae*: Structure, Function, and Biogenesis. *Microbiol Rev* 59(2):304–322.

232. Padilla-López S, Pearce DA (2006) *Saccharomyces cerevisiae* Lacking Btn1p Modulate Vacuolar ATPase Activity to Regulate pH Imbalance in the Vacuole. *J Biol Chem* 281(15):10273–10280.

233. Giaever G, et al. (2002) Functional profiling of the *Saccharomyces cerevisiae* genome. *Nature* 418(6896):387–391.

234. Dobin A, et al. (2013) STAR: ultrafast universal RNA-seq aligner. *Bioinformatics* 29(1):15–21.

235. Trapnell C, et al. (2012) Differential analysis of gene regulation at transcript resolution with RNA-seq. *Nat Biotechnol 2012 311* 31(1):46–53.

236. Hanawa Y, Watanabe M, Karatsu Y, Fukuzawa H, Shiraiwa Y (2007) Induction of a high-CO2-inducible, periplasmic protein, H43, and its application as a high-CO2-responsive marker for study of the high-CO2-sensing mechanism in Chlamydomonas reinhardtii. *Plant Cell Physiol* 48(2):299–309.

237. Reinhardt I, Haebel S, Herbik A, Buckhout TJ (2006) Proteomic Studies under Iron Stress: Iron Deficiency-Induced Regulation of Protein Synthesis in the Green Alga *Chlamydomonas reinhardtii*. *Iron Nutr Plants Rhizospheric Microorg*:371–393.

238. Allmer J, Naumann B, Markert C, Zhang M, Hippler M (2006) Mass spectrometric genomic data mining: Novel insights into bioenergetic pathways in *Chlamydomonas reinhardtii*. *Proteomics* 6(23):6207–6220.

239. Atteia A, et al. (2009) A Proteomic Survey of *Chlamydomonas reinhardtii* Mitochondria Sheds New Light on the Metabolic Plasticity of the Organelle and on the Nature of the α-Proteobacterial Mitochondrial Ancestor. *Mol Biol Evol* 26(7):1533–1548.

240. Ma F, Salomé PA, Merchant SS, Pellegrini M (2021) Single-cell RNA sequencing of batch Chlamydomonas cultures reveals heterogeneity in their diurnal cycle phase. *Plant Cell* 33(4):1042–1057.

241. Kabała K, Kłobus G yna (2005) Plant Ca^{2+}-ATPases. *Acta Physiol Plant* 27(4):559–574.

242. Pivato M, Ballottari M (2021) *Chlamydomonas reinhardtii* cellular compartments and their contribution to intracellular calcium signalling. *J Exp Bot*. doi:10.1093/JXB/ERAB212.

243. García Bossi J, et al. (2020) The role of P-type IIA and P-type IIB Ca^{2+}-ATPases in plant development and growth. *J Exp Bot* 71(4):1239–1248.

244. Wang L, et al. (2020) Genome-Wide Identification, Expression Profiling, and Evolution of Phosphate Transporter Gene Family in Green Algae. *Front Genet* 0:1170.

245. Fabiańska I, Bucher M, Häusler RE (2019) Intracellular phosphate homeostasis – A short way from metabolism to signaling. *Plant Sci* 286:57–67.

246. Moseley JL, Chang CW, Grossman AR (2006) Genome-Based Approaches to Understanding Phosphorus Deprivation Responses and PSR1 Control in *Chlamydomonas reinhardtii*. *Eukaryot Cell* 5(1):26–44.

247. Moseley JL, Gonzalez-Ballester D, Pootakham W, Bailey S, Grossman AR (2009) Genetic Interactions Between Regulators of Chlamydomonas Phosphorus and Sulfur Deprivation Responses. *Genetics* 181(3):889–905.

248. Bonnot C, et al. (2017) Functional PTB phosphate transporters are present in streptophyte algae and early diverging land plants. *New Phytol* 214(3):1158–1171.

249. Mathan KK, Amberger A (1977) Influence of Iron on the Uptake of Phosphorus by Maize. *Plant Soil* 46(2):413–422.

250. Singh M, Dahiya SS (1976) Effect of Calcium Carbonate and Iron on the Availability and Uptake of Iron, Manganese, Phosphorus and Calcium in Pea (*Pisum sativum* L.). *Plant Soil* 44(3):511–520.

251. Singh A, Kaur N, Kosman DJ (2007) The Metalloreductase Fre6p in Fe-Efflux from the

Yeast Vacuole. *J Biol Chem* 282(39):28619–28626.

252. Li L, Ward DM (2018) Iron toxicity in yeast: transcriptional regulation of the vacuolar iron importer Ccc1. *Curr Genet* 64(2):413–416.

253. Zhang X, Zhang D, Sun W, Wang T (2019) The Adaptive Mechanism of Plants to Iron Deficiency via Iron Uptake, Transport, and Homeostasis. *Int J Mol Sci* 20(10). doi:10.3390/IJMS20102424.

254. Zhang Y, Xu Y-H, Yi H-Y, Gong J-M (2012) Vacuolar membrane transporters OsVIT1 and OsVIT2 modulate iron translocation between flag leaves and seeds in rice. *Plant J* 72(3):400–410.

255. Laulhere JP, Briat JF (1993) Iron release and uptake by plant ferritin: effects of pH, reduction and chelation. *Biochem J* 290(Pt 3):693.

256. Roschzttardtz H, et al. (2013) New insights into Fe localization in plant tissues. *Front Plant Sci* 0(SEP):350.

257. Klompmaker SH, Kohl K, Fasel N, Mayer A (2017) Magnesium uptake by connecting fluid-phase endocytosis to an intracellular inorganic cation filter. *Nat Commun 2017 81* 8(1):1–12.

258. Labbé S, Zhu Z, Thiele DJ (1997) Copper-specific Transcriptional Repression of Yeast Genes Encoding Critical Components in the Copper Transport Pathway. *J Biol Chem* 272(25):15951–15958.

259. Georgatsou E, Mavrogiannis LA, Fragiadakis GS, Alexandraki D (1997) The Yeast Fre1p/Fre2p Cupric Reductases Facilitate Copper Uptake and Are Regulated by the Copper-modulated Mac1p Activator. *J Biol Chem* 272(21):13786–13792.